FEDERAL UNIVERSITY OF SÃO CARLOS
CENTER FOR EXACT SCIENCES AND TECHNOLOGY
MATERIALS SCIENCE AND ENGINEERING GRADUATE PROGRAM

STUDY OF RUTILE-SUPPORTED ANATASE NANOSTRUCTURED FILMS AS PHOTOCATALYSTS FOR THE DEGRADATION OF WATER CONTAMINANTS

Margaret Dawson

São Carlos
2015

FEDERAL UNIVERSITY OF SÃO CARLOS
CENTER FOR EXACT SCIENCES AND TECHNOLOGY
MATERIALS SCIENCE AND ENGINEERING GRADUATE PROGRAM

STUDY OF RUTILE-SUPPORTED ANATASE NANOSTRUCTURED FILMS AS PHOTOCATALYSTS FOR THE DEGRADATION OF WATER CONTAMINANTS

Margaret Dawson

Dissertation presented in partial fulfillment of the requirements for the degree MASTER OF SCIENCE IN MATERIALS SCIENCE AND ENGINEERING

Advisor: Dr. Márcio Raymundo Morelli
Co-advisor: Dr. Cauê Ribeiro de Oliveira
Funding Agency: CNPq

São Carlos
2015

Ficha catalográfica elaborada pelo DePT da Biblioteca Comunitária UFSCar
Processamento Técnico
com os dados fornecidos pelo(a) autor(a)

Dawson, Margaret
D272sr Study of rutile-supported anatase nanostructured films as photocatalysts for the degradation of water contaminants / Margaret Dawson. -- São Carlos : UFSCar, 2015.
129 p.

Dissertação (Mestrado) -- Universidade Federal de São Carlos, 2015.

1. TiO2. 2. Photocatalysis. 3. Anatase films. 4. Rutile support. I. Título.

DEDICATION

This work is dedicated to my mother,

Beauty Norgbey

And my siblings,

Emmanuella Hofe, Solomon Dawson, John Dawson, David Dawson

CANDIDATE`S VITAE

Bachelor of Science in Materials Engineering with major in Metals (UFSCar - 2012), Bachelor of Science in Materials Engineering with major in Ceramics (UFSCar - 2011).

UNIVERSIDADE FEDERAL DE SÃO CARLOS

Centro de Ciências Exatas e de Tecnologia
Programa de Pós-Graduação em Ciência e Engenharia de Materiais

Folha de Aprovação

Assinaturas dos membros da comissão examinadora que avaliou e aprovou a Defesa de Dissertação de Mestrado da candidata Margaret Dawson, realizada em 30/03/2015:

Prof. Dr. Márcio Raymundo Morelli
UFSCar

Prof. Dr. Conrado Ramos Moreira Afonso
UFSCar

Profa. Dra. Maria Inês Basso Bernardi
USP

ACKNOWLEDGEMENT

Foremost, I would like to thank God and the Brazilian government for giving me such an opportunity. I also thank CNPq for the funding of this masters project.

I would like to express my sincere gratitude to the Federal University of São Carlos (UFSCar), materials science and engineering department (DEMa), materials science and engineering graduate program (PPGCEM) and staff especially my advisor, Prof. Dr. Márcio R. Morelli for his help, guidance, support, expertise, patience and encouragement during these years. The completion of this dissertation would not have been possible without his participation and support.

To my co-advisor, Prof. Dr. Cauê Ribeiro, thank you for your numerous feedbacks, suggestions, support and profound interest in the research project. I appreciate the opportunity of being a member of your research group at Embrapa Instrumentation. Also, my profound gratitude to Embrapa Instrumentation.

I would like to thank my fellow graduate students and members of the nanotechnology research group (Embrapa Instrumentation) for the encouragement, support and advice. In particular, Gabriela Byzynski, Lilian Cruz, Kele Carvalho, Osmando Ferreira Lopes, Roger Piva and Andre Esteve.

I am grateful to the following research technicians (DEMa/UFSCar and Embrapa Instrumentation) for their collaboration and support: Adriana Tomaz, Viviane Soares, Paulo Lasso, Silviane Hubinger, Alexandra Manzoli, Walter Mariano, José Roberto Binotto, José Luiz dos Santos, and José Rodrigues da Silva.

I thank my family for their love and emotional support over the years.

ABSTRACT

This dissertation studies the application of rutile substrate as an alternative support for anatase films, specifically, on the growth and properties of anatase films. The films were utilized as catalysts for the photodegradation of water contaminants (Atrazine and Rhodamine B). Ti^{4+} precursor resin was prepared by the polymeric precursor method and deposited by spin coating onto polycrystalline rutile and rutile coated glass substrates. The films were calcined at different temperatures (350 °C to 500 °C) to form anatase TiO_2 films. The influence of temperature on the properties of the films has been reported in this study. A comparative study of the films was also done using X-ray diffraction technique (XRD), grazing incidence X-ray diffraction (GIXRD), atomic force microscopy (AFM) and scanning electron microscopy (SEM). XRD and GIXRD results confirmed the formation of anatase on the (101) plane depending on the calcination temperature. Bandgap modification of the films with respect to calcination temperature was measured by UV visible diffuse reflectance spectroscopy. The bandgaps were in the range of 2.74 to 2.85 eV. Photocatalytic activity of the films supported on rutile substrate was studied for the degradation of Atrazine (ATZ) and Rhodamine B (Rhod-B) under UV light. Further, the stability of the films was evaluated on four consecutive cycles where the films maintained their photocatalytic properties in all cases. The kinetics of Rhod-B and ATZ degradation followed a pseudo first order and first order exponential decay respectively. The films calcined at 450 °C and 500 °C showed superior photocatalytic activity for Rhod-B degradation than the films calcined at 350 °C and 400 °C. This is attributed to the adequate crystallinity of anatase. For ATZ degradation, the films were also efficient but no specific trend was observed. The results can contribute towards the development of TiO_2 films on rutile phase substrates.

ESTUDO DE FILMES NANOESTRUTURADOS DE ANATASE SUPORTADO SOBRE RUTILO COMO FOTOCATALISADORES PARA DEGRADAÇÃO DE CONTAMINANTES DA ÁGUA.

RESUMO

Esta dissertação estuda a aplicação de substratos de rutilo como suportes alternativos para filmes de anatase, especificamente, sobre o crescimento e propriedades de filmes de anatase sobre rutilo. Os filmes foram utilizados como catalisadores para a fotodegradação de contaminantes de água (Atrazina e Rodamina B). A resina de Ti^{4+} foi preparada pelo método de precursores poliméricos e depositada por *spin coating* sobre rutilo policristalino e em substratos de vidro revestido de rutilo. As amostras foram calcinadas a diferentes temperaturas (350 a 500 °C) para formar filmes de anatase TiO_2. Um estudo comparativo dos filmes foi feito usando a técnica de difração de raios X (DRX), difração de raios X com ângulo rasante (DRXR), microscopia de força atômica (AFM) e microscopia eletrônica de varredura (MEV). Os resultados de DRX e DRXR confirmaram a formação de anatase nos filmes ao longo do plano (101) dependendo da temperatura de calcinação. Modificações do *bandgap* dos filmes de acordo com a temperatura de calcinação foram medidas por reflectância difusa de UV-visível onde os *bandgaps* variou de 2,74 para 2,85 eV. Atividade fotocatalítica dos filmes imobilizados sobre substrato de rutilo foi estudada para a degradação de Atrazina (ATZ) e Rodamina B (Rhod-B) sob luz UV. Além disso, a estabilidade dos filmes foi avaliada em quatro ciclos consecutivos onde os filmes mantiveram suas propriedades fotocatalíticas em todos os ciclos. As cinéticas de degradação de Rhod-B e de ATZ seguiram um ajuste de pseudo-primeira ordem e decaimento exponencial de primeira ordem, respectivamente. Os filmes que foram calcinados a 450 °C e 500 °C mostraram atividade fotocatalítica superior para a degradação de Rhod-B aos filmes calcinados a 350 °C e 400 °C. Isto foi atribuído à cristalinidade adequada da fase anatase. Para ATZ, os filmes foram eficientes mas nenhuma tendência especifica foi observada. Os resultados podem contribuir para o desenvolvimento de filmes de TiO_2 imobilizados sobre substratos de rutilo.

PUBLICATIONS

DAWSON, M.; RIBEIRO, C.; MORELLI, M. R. Rutile supported anatase nanostructured films for the degradation of water contaminants. **Ceramics International**, v. 42, n. 1, p. 808-819, 2016.

x

TABLE OF CONTENTS

LIST OF FIGURES

xx

LIST OF TABLES

ABBREVIATIONS

AFM	Atomic force microscopy
ATZ	Atrazine
DLS	Dynamic light scattering
EDX	Energy dispersive X-ray spectroscopy
FEG	Field emission gun
GIXRD	Grazing incidence X-ray diffraction
Rhod-B	Rhodamine B
SEM	Scanning electron microscopy
TEM	Transmission electron microscopy
XRD	X-ray diffraction

1 INTRODUCTION

Brazil is currently the largest consumer of pesticides in Latin America [1]. Although pesticide use in Brazil is beneficial to agriculture and the economy, it can also cause water and soil pollution. A case study on the aquifer of Tiangua municipality in Ceara state of Brazil from 2003 to 2006 revealed that some underground wells that supply water to the community had levels of Atrazine (herbicide) above the allowed concentration for human consumption [2]. Jamoni et al. (2011) examined Ametryn levels in water and sediment samples taken from Baixo Pardo area, northeastern part of São Paulo state where sugar cane production is predominant [3]. The study showed that Ametryn concentration in the sediments was higher than that of the water samples from some particular sampling areas indicating that the persistence of pesticides in sediments is very high. Persistent pesticides are a problem due to their long term transportation and contamination. Nogueira et al. (2012) tested water samples collected from Campo Verde and Lucas do Rio Verde cities in Mato Grosso state, for Ametryn [4]. The samples were extremely high in Ametryn (28 $\mu g.L^{-1}$) compared to the allowed concentration limit (2 $\mu g.L^{-1}$). These alarming findings show that there is indeed underground water pollution in some regions of the country and the habitants of areas near agriculture intensive lands may be exposed to long term health risk. Thus in areas of intense agricultural activities, there is a growing concern about the quality of drinking water.

Fortunately, the permitted amount of certain pesticides in drinking water is well established in Brazil [5]. Also, according to Autonomous Water and Sewage Service (SAAE), pesticide concentration in drinking water is monitored [6,7]. In spite of these efforts, there is no defined protocol to follow in the event of high concentration. It is therefore worth considering in the future, the gradual substitution of conventional water treatment for technologies such as advanced oxidative processes which can eliminate a variety of organic substances [8].

The development of suitable catalysts for continuous flow systems is a crucial step in water treatment on a large scale employing advanced oxidative processes. Titanium dioxide powder (catalyst) has been well studied and has disadvantages for flow systems [9]. However, the catalyst (TiO_2) immobilized on

a substrate allows easy handling for flow systems. Furthermore, the substrate can participate in the photocatalytic process [10].

Research attention has been paid to semiconductor photocatalysis during the past decades because it has a bright future for providing versatile solutions to pollution problems. It is not surprising, therefore, that quite a number of emerging technologies for water purification, air purification, sterilization and self cleaning surfaces are based on photocatalysis [11]. The main semiconductors used for photocatalysis are TiO_2, SnO_2, ZnO, CdS due to their peculiar electronic structure [12-15]. TiO_2 is by far the most utilized and investigated photocatalyst; in particular, it has unique properties such as high photo-oxidization, high photostablility, low cost and non-toxicity [16].

TiO_2 exists in three polymorphic phases: anatase (tetragonal), rutile (tetragonal) and brookite (orthorhombic). The type of phase present in the semiconductor is crucial for its application since it controls the properties of the semiconductor. For instance, rutile phase is rarely utilized as a photocatalyst due to its poor photoreactivity [17]. On the other hand, rutile has a high refractive index and high ultraviolet absorption, key properties for pigments and paints [18]. For photocatalysis, anatase phase is known to have superior properties than brookite and rutile phase. But, when it comes to phase stability, anatase and brookite phase are metastable compared to rutile [19]. This implies that they are readily transformed to stable rutile phase at high temperatures. Anatase phase transformation is a problem since it can compromise photocatalytic activity for high temperature applications. Further, it imposes a temperature limitation on anatase synthesis. Accordingly, the studies and development of alternative methods for anatase phase stabilization are of great importance.

Most photoreactions take place on a semiconductor’s surface as such there is continuous effort to improve and maximize surface area [20-24]. An easy approach for improving surface to volume ratio is utilizing nanometric semiconductor powders. Despite being successful, the method requires posterior separation of the powder after use, especially for slurry based applications which mar the method as not energy and cost-effective [25]. In

order to avoid these problems, researchers are now utilizing TiO_2 films immobilized on substrates. This alternative also permits the exploration of surface properties of TiO_2 for application such as antibacterial coatings [26,27] and dye sensitized photovoltaic cells [28].

There are three categories of film deposition techniques namely, chemical vapor deposition (CVD), physical vapor deposition (PVD) and wet chemical deposition techniques [29]. In practice, CVD and PVD techniques are faced with problems such as high deposition temperature, expensive precursors, toxic byproducts and a large number of process variables. Because of these problems, wet chemical deposition methods tend to be more attractive and practical. A typical example is sol-gel, a wet chemical method that allows the variation of precursors and process parameters. Furthermore, high degree of homogeneity at molecular level has been reported [30,31]. The synthesis of TiO_2 film (anatase) by sol-gel requires subsequent calcination to eliminate organic matter present in the film and induce crystallization.

Considering that anatase phase is thermodynamically unstable, the calcination temperature chosen can affect the crystallinity and polymorphic transformation of anatase to rutile. Studies have shown that doping and particle size control can increase the stability of anatase phase [32,33]. However, few studies have investigated the effect of substrates on the transformation of anatase. This effect occurs in different materials, in which the substrate promotes phase retention of the formed layer, thereby preventing the transformation of the metastable phase. Furthermore, substrates with low surface area may induce nucleation of the stable crystalline phase, favoring the transformation of the metastable phase.

A number of substrates have been utilized for the growth of anatase films such as glass, $SrTiO_3$ and $LaAlO_3$ [34-37]. Apart from glass, most of these substrates are in the form of single crystals especially for the purpose of oriented growth and single anatase crystal films. These films are mostly studied for their structural and optical properties than photocatalytic properties. However, oriented anatase films can be beneficial to photocatalytic activity due to enhanced charge carrier [38]. From a practical and economical viewpoint, the

substrate must be easily attainable and cheap. It is in this regard that polycrystalline rutile substrate can be considered as a potential candidate for the oriented growth (epitaxy) of anatase because it is chemically and structurally similar to anatase and could be cheaper than single crystal substrates.

In the literature, the strategy of growing anatase films on polycrystalline rutile substrate has been rarely reported even though a vast number studies have explored anatase-rutile transformation. In addition, little attention has been drawn to the possible role of rutile as a seed for oriented growth of anatase particularly the tendency of rutile to induce or constrain the premature phase transformation of anatase during calcination. Furthermore, studies on the mutual orientation between anatase and rutile during phase transformation (topotaxy) has not been explored either.

Rutile as a substrate would allow electronic transition between anatase and rutile since the difference between their bandgaps is very small. Furthermore, previous studies demonstrate that the combination of anatase and rutile contributes to the photocatalytic property of Degussa P25 TiO_2 commercial powder. It contains 80% of anatase and 20% of rutile and in general, the mixture of the phases is the main reason for its high photoactivity [39-40].

1.1 Objectives

With the aforementioned factors and motivation, the main objective of this research is to develop biphasic asymmetric TiO_2 substrates with rutile phase as a dense support for anatase film. The films will be tested as potential catalysts for future water treatment. The research seeks to contribute to the body of knowledge in biphasic substrates and anatase–rutile transformation studies especially, the effect of rutile phase on the growth of anatase and if it induces or constrains the oriented growth and phase transformation of anatase. Also, to highlight the potential of the films as catalysts for water contaminants.

2 LITERATURE REVIEW

The literature review aims to establish a theoretical background on the main concepts and the state of art underlying the project despite the limited literature on anatase phase supported on rutile phase or similar assembly.

2.1 Advanced oxidative processes

Advanced oxidative processes are based on the production of oxidants, mainly hydroxyl ($^{\cdot}OH$) and superoxide ($O_2^{\cdot -}$) radicals for the mineralization (complete oxidation) of organic and inorganic pollutants [41]. Employing these processes, organic and inorganic pollutants can be transformed into simple compounds such as carbon dioxide and water. This transformation can be observed through color change (dyes), reduction of chemical and biochemical oxygen demand of a system.

The oxidizing behavior of hydroxyl radicals comes from the instability associated with the unpaired electrons located in their valence bands. The oxidizing power of a radical is measured by its standard oxidation potential of which hydroxyl radical presents a value of 2.8 V, second to fluoride (3.0 V) as the most potent oxidant. Thus, the radical is non-selective towards the degradation of organic and inorganic compounds.

Advanced oxidative processes can be classified into photochemical and non-photochemical processes. The criterion for this classification is based on the role of ultraviolet light (UV) in the generation of $^{\cdot}OH$ radicals, where the presence of ultraviolet light (UV) is essential for the generation of radicals via photochemical processes while for non-photochemical processes ultraviolet light (UV) is not employed [42]. Some examples of non-photochemical processes are O_3/OH^- (ozone/hydroxide radical), O_3/H_2O_2 (ozone/hydrogen peroxide), Fenton processes, electrochemical oxidation, plasma and ultrasound treatment.

For photochemical processes, some classic examples are subcritical and supercritical water oxidation, vacuum and ultraviolet light mediated water

photolysis (UVV), UV/H_2O_2, O_3/UV, H_2O_2/UV/O_3, photo-Fenton processes and semiconductor photocatalysis. Huang et al. (1993) introduced a different classification of advanced oxidative processes based on the presence or absence of a catalyst [43], where processes that employ catalysts for radical generation are predominantly heterogeneous and those that occur without catalysts are homogeneous.

Most homogeneous photochemical processes are applied on a large scale for water treatment. Despite their statuses, they are faced with numerous challenges. For instance, the UV/O_3 system can generate toxic byproducts, bromate ion (BrO_3^-), formed from the oxidation of bromide ions (Br^-) present in the untreated water [44]. Bromide ions are naturally present in sea water and subsurface brines therefore UV/O_3 treatment of water from coastal regions is susceptible to bromate ion formation. Studies on bromate ions have shown that they are carcinogenic, as such; the maximum allowable amount of contamination in portable water is 10 $\mu g.L^{-1}$ both in Europe and the United States [45].

Another prominent example is the H_2O_2/UV system [46]. Elements such as Fe, Ca and Mg reduce the efficiency of the system since they absorb more UV light than hydrogen peroxide reducing the dissociation of the latter into OH radicals. In addition, traces of carbonate ions (CO_3^{2-}) and bicarbonate ions (HCO_3^-) in saline waters scavenge hydroxyl radicals generated [47]. The above problems have motivated the search for other alternative water treatment methods.

Heterogeneous photocatalysis in the presence of a semiconductor has been studied as a potential method for water treatment on a large scale and presents future prospects for the replacement of homogeneous processes or as a complement to these processes.

The features that highlight the viability of heterogeneous photocatalysis are room temperature working conditions, no additional reagents needed, complete mineralization, generation of intermediate compounds with no risk of secondary pollution and low operation cost [9].

2.1.1 Photocatalysis TiO_2

Photocatalysis refers to the acceleration of a photoinduced or light-activated reaction in the presence of a catalyst. Semiconductors (TiO_2, SnO_2, ZnO, ZnS, CdS, among others) have chemical and physical properties associated with their electronic structure that permit their use as photocatalysts [48]. TiO_2 is the most widely utilized photocatalyst due to its chemical stability, non-toxicity, low cost and high oxidizing power. It presents three main polymorphs: anatase (tetragonal), rutile (tetragonal) and brookite (orthorhombic). Figure 2.1 presents the electronic structure of TiO_2.

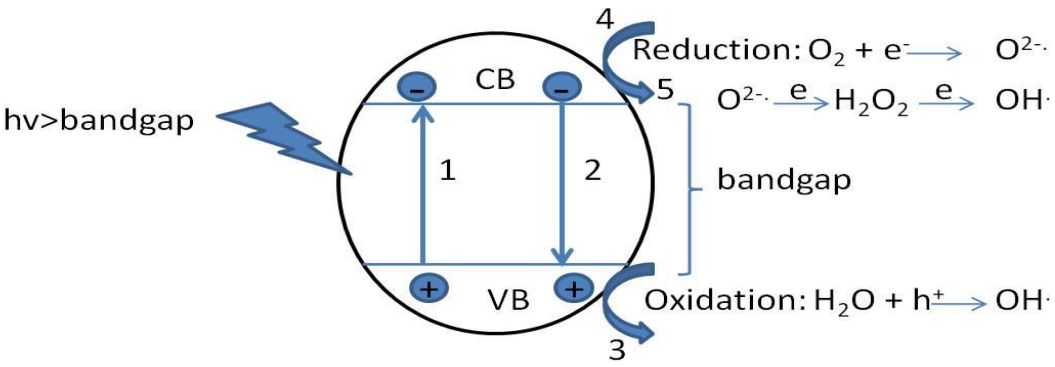

Figure 2.1 - Electronic structure and photocatalytic mechanisms of TiO_2 [48].

The electronic structure of TiO_2 consists of a filled valence band (VB) and an empty conduction band (CB) (Figure 2.1). The energy needed to translate electrons from the valence band to the conduction band is represented by the bandgap or the energy barrier between the bands. The bandgap of anatase and rutile is 3.2 eV and 3.0 eV respectively [49].

The photoactivation of TiO_2 occurs through the absorption of photons of energy equal to or greater than the bandgap energy, allowing the transition of electrons from the valence band to the conduction band (process 1 Figure 2.1). This transition creates holes in the valence band and equivalent electrons in the conduction band. When TiO_2 is activated, the electrons in the conduction band can return to their ground state (valence band) annihilating the electron/hole pairs in a process called recombination as shown by process 2 in Figure 2.1. The efficiency of a photocatalytic process is governed by the competitive photogeneration of electron/hole pairs and electron/hole recombination. Faster

recombination is undesired because it reduces the lifetime of charge carriers and oxidizing species. Studies show that surface or structural modification of TiO_2 with metals (Ag, Pt, Pd) can decrease recombination [50].

Photogenerated holes are powerful oxidants (+1.5 to +3.5 V versus normal hydrogen electrode) capable of forming hydroxyl radicals responsible for the degradation of organic substances in solution [51]. They accept electrons from donor adsorbed species, turning them into unstable reactive organic radicals that undergo subsequent degradation reactions [52]. However, for the degradation of free molecules in solution, dissociated water molecules or OH groups attached to the surface of TiO_2 are oxidized by holes to form hydroxyl radicals as shown in Figure 2.1 as process 3 [53].

The electrons promoted to the conduction band, on the other hand, are good reducing agents (+0.5 to 1.5 V). They can reduce absorbed oxygen to form superoxide radicals (process 4 Figure 2.1). Superoxide radicals despite not being very potent, contribute to the degradation of organic substances since they react with water or hydrogen peroxide to form hydroxyl radicals (process 5 Figure 2) [54].

The degradation of organic compounds in solution through TiO_2 photocatalysis consists mainly of three steps: adsorption of compounds on the photoactivated TiO_2 surface, mineralization of the adsorbed compounds through oxidation and reduction reactions and desorption of the mineralized products. In all these processes, mass transfer is required so it can be a rate limiting factor of the photodegradation process [55].

With respect to photocatalytic activity, anatase phase has superior photoactivity than rutile and brookite phase. There are several hypotheses behind the appreciable photoactivity of anatase compared to rutile phase. Among them, the differences in electronic structure of anatase and rutile phases with regard to Fermi level and the type of bandgap are popular [56]. All things being equal, the Fermi level of anatase is lower than rutile and as a consequence, the barrier to electron emission and holes generation is lower for anatase than rutile. The same Fermi energy is responsible for the degree of oxygen affinity and formation of hydroxyl radicals which are directly related to

photoactivity. The type of bandgap is also a determining factor, being that the lifetime of photogenerated carriers is longer in an indirect bandgap (anatase) than in a direct bandgap (rutile).

TiO_2 photocatalysis has a great potential for water treatment and has been widely studied. According to Lee et al. (2013), an ideal semiconductor photocatalysis system for water remediation needs to function at room temperature or pressure, present complete mineralization without secondary pollution and incur low operation cost. Almost all of these factors are attainable utilizing TiO_2 [57]. To date, TiO_2 water remediation plants are in the pilot project stage. An example of a pilot plant undergoing assessment is located at INETI (Instituto Nacional de Engenharia, Technologia Industrial e Inovacao, Portugal) where most feasibility data of the process are analyzed.

In general, there are three types of photoreactors for water treatment under research and development: reactors with suspended catalyst particles, reactors with immobilized catalyst particles on a substrate and reactors with photocatalytic membrane [55]. Suspended catalyst reactors require an additional separation step which makes the process noncontinuous. On the other hand, immobilized catalyst and membranes offer a continuous process. Chin et al. (2006) reported that membranes with immobilized TiO_2 catalyst particles could undergo degradation due to harsh UV and hydroxyl environments [58]. In some cases, the pores of the membrane can be blocked after prolonged use. Therefore, a suitable substrate for immobilized TiO_2 particles is very important.

The success of a photocatalytic plant depends on several operational factors such as TiO_2 loading, light intensity, pH of the reaction medium, dissolved oxygen among others [55].

2.1.2 Immobilized anatase

To maximize the photoactivity of TiO_2, the particles must have high surface to volume ratio to offer high specific surface areas and reactivity. Unfortunately, the use of fine particles for photocatalysis on a large scale is

limited due to the high cost of post filtering, aggregate formation and low photocatalytic activity [59,60].

Titanium oxide (TiO_2) films are of interest for various applications including microelectronics, optical cells, solar energy conversion and catalysts [61]. The trend in technology nowadays is the miniaturization of various systems and it is evident in the increasing studies on TiO_2 films for photocatalysis. Considering that catalytic processes are surface related, films offer an option for miniaturization and at the same time enhancing surface properties.

Film technology involves obtaining desired properties through the manipulation of microstructural parameters and film thickness [61]. Anatase films have been immobilized on various supports such as glass, silica, quartz, activated carbon, zeolite, fiberglass, stainless steel, ceramics, fabrics, fibers, and polymer monolith [62-67].

Pozzo et al. (1997) studied the photoactivity of supported TiO_2 catalysts and concluded that a good support should be transparent to UV radiation, present strong physical and chemical affinity with TiO_2 without altering the properties of TiO_2, have a high specific area and should be chemically inert [60]. A substrate can have functions associated to photocatalysis. For example, silica assists in the adsorption of organic compounds during photocatalytic processes [68-70]. Kim and Yoon (2001) reported that zeolite slowed the recombination of charges due to its charged surface [71]. Sasikala et al. (2010) demonstrated that the optical properties of TiO_2 were improved when it was supported on ZrO_2 [72].

A substrate also plays a key role in the nucleation and growth of films. A crystalline film can be grown on a substrate such that it has a well defined orientation with respect to the substrate's crystal structure. In this case, the deposited film may grow preferentially in one or more crystallographic orientations of the substrate's crystals [73]. This phenomenon is termed as epitaxy. Crystal structure and/or chemical composition are known to induce epitaxial growth. Epitaxial growth of TiO_2 was observed on NaCl substrates [74]. $LaAlO_3$ (LAO) and $SrTiO_3$ (STO) substrates with (100) and (110) orientations respectively, were utilized for the growth of epitaxial TiO_2 films [75]. Epitaxial

growth of TiO_2 on $SrTiO_3$/TiN replicates has also been reported. The films were highly oriented in the c axis direction of the lattice of anatase [76].

The possibility of rutile phase inducing epitaxial growth of anatase has not been studied. In fact, there are limited publications on the use of rutile support for anatase film. Xie et al. (2015) prepared anatase films coated on the surface of rutile TiO_2 nanowires to form a one dimensional core-shell base structure by hydrothermal synthesis of a mixed phase powder. In this study, epitaxy was not studied [77]. In another study, nanostructures formed of anatase layer deposited on rutile layer were obtained through layer by layer (LbL) assembling technique. Through this technique, nanoparticles of anatase were deposited on the surface of rutile nanorods employing poly sodium-4-styrenesulfonate (PSS) adhesion layer. With this method, the polyelectrolyte was crucial for the adhesion of anatase nanoparticles to the rutile nanorods [78]. A research study also focused on anatase thin films deposited by sputtering coupled with sol-gel on a 165 nm thick rutile film [79]. The efficiency of the films in degrading CH_3CHO gas was linked to the nanoscale heterojunction between the phases. Hence, the use of rutile as substrate has a potential in the development of anatase films with interfaces that aid in photoactivity. In addition, charge separation can be enhanced if there is effective electronic transition between the substrate and film. For example, epitaxial TiO_2:SnO_2 structure has superior photoactivity as compared to pure TiO_2. The improved photoactivity reported is attributed to the migration of generated electrons from TiO_2 to SnO_2. Thus, the lifetime of holes in TiO_2 is increased and recombination is reduced [80].

In the previously mentioned studies, anatase phase was already formed in the raw material which is different from the experimental approach adopted in this dissertation where the phase is developed during the synthesis process.

2.2 Sintering of dense rutile compacts

Ceramic and metal components manufactured by powder consolidation must undergo sintering to develop adequate final properties. Sintering forms

part of the processing of powder compacts where thermal energy is applied in order to increase density and mechanical strength. The driving force for sintering is the reduction of total interfacial energy [81]. Interfacial energy is associated with the surface area of powder particles and surface defects. Thermodynamically, the variation of a system's energy can be represented by Equation 2.1:

$$\delta G_{system} = \delta \int \gamma_{sv}\, dA_{sv} + \delta \int \gamma_{ss} dA_{ss} \tag{2.1}$$

where δG_{system} is the change in the free energy of the system, γ_{SV} is the energy per unit area of the solid-vapor interface, and γ_{SS} is the energy per unit area of the solid-solid interface.

For solid state sintering, the reduction of a system's free energy is related to densification (reduction of solid/vapor interface (pores)) and the increase in the solid/solid interfaces (grain growth and coarsening). Densification and grain growth/coarsening contribute to the decrease in the free energy of the system. Due to this, both mechanisms are competitive. Therefore, to obtain high density sintered bodies, it is necessary to control the sintering process such that densification becomes dominant for the reduction of surface energy [82]. The degree of densification is controlled by the microstructure of the green body and sintering parameters. These factors can be categorized into two major variables: material and process variables [83]. The variables related to raw materials include the powder's chemical composition, particle size, morphology, particle size distribution and degree of agglomeration. Raw material properties influence powder flow, compressibility during pressing and reactivity during sintering. Because the reactivity of fine powders is high, it is desirable that the starting powder for dense sintered compacts must be fine but with sufficient flowability and compressibility for adequate green compact properties. In addition, the particle size distribution of the powder has to be narrow so that there is minimal variation in density and pore volume which reduces the probability of abnormal grain growth during sintering. The total volume of pores in a green compact is related to its particle size and distribution as well as compacting pressure. Accordingly, a powder with small particles and narrow

size distribution tends to have smaller pore size and pore volume. In this way, densification by pore elimination is favored. Also, microstructural inhomogeneities in a green compact (e.g. variations in density, pore volume, particle size, and composition) result in low density after sintering [82].

Temperature is an important factor in sintering processes because it provides the activation energy for various diffusion and mass transport processes. Depending on the sintering temperature, certain densification related processes may or may not be activated. For example, in solid state sintering, mass transport from particle surfaces to the neck region between particles does not cause densification while diffusion from grain boundary to the neck region induces densification [81].

Dense rutile bodies have been reported in the literature. Real et al. (2001) attained a density of 95 to 98% after sintering rutile compacts with 72% green density at 1500 °C in air [84]. In this study, the powders were milled before sintering. Li et al. (2007) prepared a sintering master curve for rutile pellets [85]. The validity of the curve was tested with pellets isostatically pressed and sintered at 900 °C/4h, 1000 °C/3h and 1100 °C/2h in air. The resultant densities were 61%, 80% and 92% respectively.

Dense rutile bodies can be obtained by sintering compact anatase powders. For example, a commercial anatase powder with average particle size of 32 nm was uniaxially pressed and sintered in air at 1200 °C/6h. Density after sintering was between 93 and 97% [86]. In another work, titania in the form of spheres were compacted in an isostatic press to form green bodies with 55% theoretical density. The green bodies were sintered at 1030 °C/2h and a density of 99% was reported [87]. In general, the temperature range for sintering of rutile bodies varies from 800 °C to 1500 °C depending on the characteristics of the starting powder.

2.3 Heterostructure anatase-rutile

Anatase is widely accepted as the TiO_2 phase which presents superior photoactivity. However, two major problems arise in the application of TiO_2 as a

catalyst. The first is that TiO_2 is activated only under UV irradiation for wavelengths lesser than 387 nm because of its bandgap (3.2 eV). Thus, the use of solar spectrum, a cheap source of light for activation of anatase is not viable. In order to improve the photoactivity of TiO_2, several modifications have been developed to increase its light absorption such as non-metallic doping using for example carbon [88], nitrogen [89] and sulfur [90] to promote the excitement of TiO_2 under visible light. The second problem is the recombination of photogenerated charge carriers that reduce considerably catalytic efficiency. The incorporation of metals into the structure of TiO_2 and TiO_2 composites have shown to be effective for inhibiting the recombination of electrons and holes as well as increasing their lifetime [91].

Among TiO_2 composites, anatase-rutile composites have attracted a lot of attention due to the separation of photogenerated charge carriers and improved photoactivity. Although rutile has inferior photoactivity than anatase, it has a lower bandgap compared to anatase. The contribution of rutile to the photoactivity of anatase-rutile composites was discovered in Degussa P25 commercial powder composed of anatase and rutile phase in the ratio of 4:1. There are several models explaining the synergistic effect between anatase and rutile on photocatalytic activity.

Figure 2.2 shows the traditional model for charge separation and synergism between anatase and rutile.

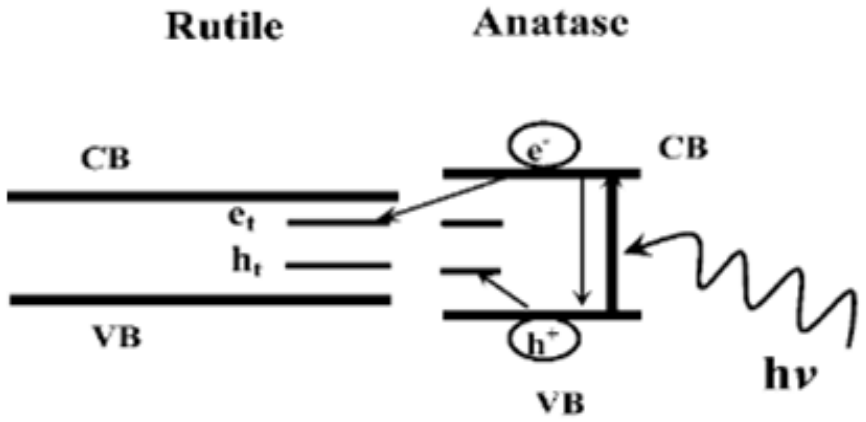

Figure 2.2 - Synergism and charge separation between anatase and rutile under UV irradiation proposed by the traditional model [93].

The traditional model is based on the activation of the composite under UV light absorption, a condition where only anatase is excited. The excited electrons from the conduction band of anatase are transitioned to electron trapping sites located in rutile electronic structure which results in charge separation and prolonged lifetime of the holes needed for hydroxyl radical production [92]. Hurum et al. (2003) proposed a different theory with the replacement of UV light with visible light [93]. Thus, only rutile can be activated under visible. Figure 2.3 shows the excitation of rutile, the electron transfer from rutile to anatase and consequent charge separation.

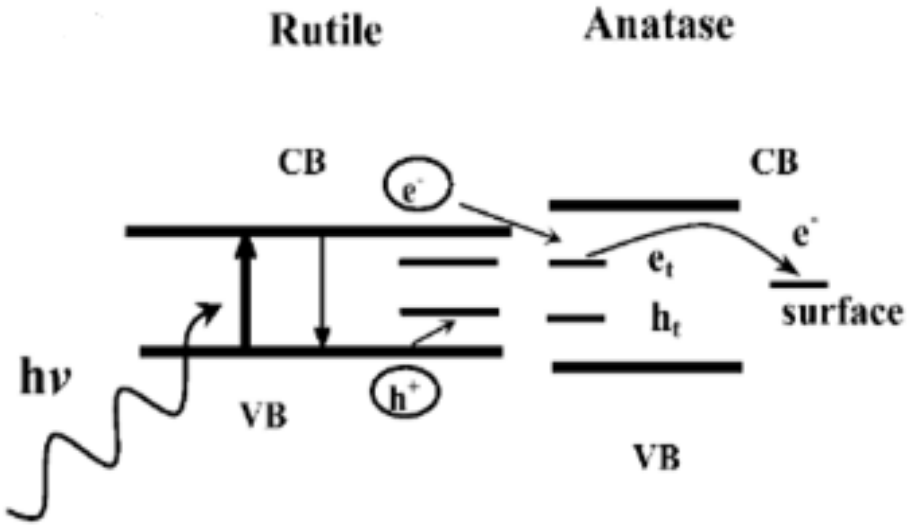

Figure 2.3 - Synergism and charge separation between anatase and rutile in the visible region [93].

The generated electrons are transferred from the conduction band of rutile to electron traps on anatase, specifically to localized traps that lie just below the conduction band of anatase. The process results in availability of holes in rutile for oxidative reactions in the visible region.

Composites formed of semiconductors with different bandgaps are characterized by discontinuities in the valence band and/or conduction band (usually both). The interface where their bands align is called a heterojunction.

Figure 2.4 shows a representation of a heterojunction formed as a result of anatase and rutile phase bandgap alignment.

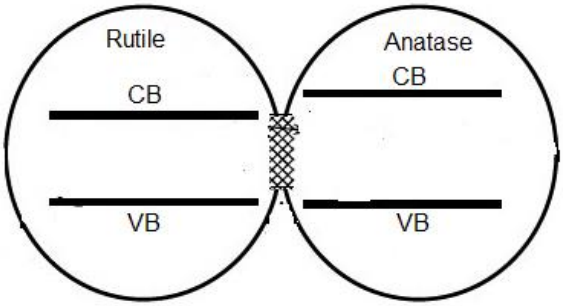

Figure 2.4 - Heterojunction formation through band alignment of anatase and rutile.

The synergistic effect between two phases depends on the quality of the interface formed between them [94]. Li et al. (2007) stated that the alignment of the interfaces is one of the most important factors for effective transfer of photogenerated charges for photocatalytic activity [94]. Synthesis methods control interface growth in terms of imperfections in the interface and fluctuation in the chemical composition in the latter. Compositional fluctuations generate localized variations in the heterojunction of the semiconductors [95]. In this way, the quality of the interface affects the efficient flow of electrons at the heterojunction.

There are several methods for the synthesis of heterostructured titanium dioxide such as gas phase methods, hydrothermal methods, microwave synthesis, sol-gel among others. Kawahara et al. (2003) synthesized TiO_2 particles containing anatase and rutile through dissolution and reprecipitation [96]. The study demonstrated that the photoactivity of the particles obtained through physical mixing without dissolution process was low due to low crystallinity, low surface area and most importantly poor interface between anatase and rutile. Ohno et al. (2003) studied TiO_2 powders prepared by the physical mixture of rutile and anatase particles and another group of particles obtained from the partial conversion of anatase phase to rutile phase through heat treatment [97]. It was reported that particle size and crystallinity of the resultant phases contributed to the synergism observed for the degradation of naphthalene.

Anatase-rutile heterostructure can be synthesized by sol-gel since it is a simple method for producing high purity materials in the form of powders and thin films [98]. Heterostructures of anatase-rutile can be obtained by calcination of TiO_2 sols or resins. The ratio of anatase to rutile depends on the calcination temperature and atmosphere [99]. These same factors also affect anatase-rutile transformation hence their control during synthesis determines the amount of each phase formed.

The morphology of anatase-rutile composites has been reported by various authors. According to Knorr et al. (2007), the composite structure is formed of individual particles with anatase core surrounded by rutile layers [100]. Park et al. (2000) also proposed that a single particle has both anatase and rutile phase [101]. Datyle et al. (1995) through high resolution transmission electron microscopy and X-ray diffraction of Degussa P25 powder, observed that nanoparticles of rutile and anatase are separated but in close contact through anatase-rutile interface [102]. Ohno et al. (2001) noted that after the dissolution of Degussa particles in hydrofluoric acid (HF) solution, rutile particles did not form as a layer on anatase particles instead anatase and rutile particles are separated and distinct [103].

2.4 Anatase-rutile transformation

TiO_2 polymorphs are built on TiO_6 octahedra that are connected by either sharing oxygen atoms through edges or vertices [104]. A unit of TiO_6 octahedron consists of a Ti^{4+} cation coordinated by six oxygen anions. Anatase and rutile polymorphs can be described as homogeneous isomers as their coordinations consist of TiO_6 octahedra with different structural arrangements.

Figure 2.5 shows the crystal structure of rutile and anatase TiO_6 polymorph with their respective octahedra arrangement. The parameters of each polymorph are also indicated. Anatase and rutile belong to the tetragonal crystal lattice system where the parameters a and b have equal dimensions that differ from the dimension of the c parameter.

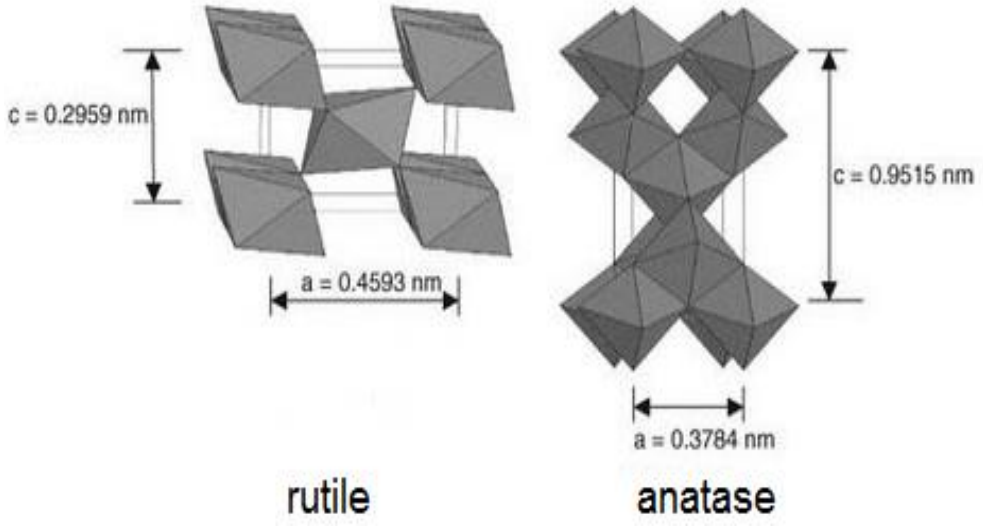

Figure 2.5 - The crystal structure of rutile and anatase with their respective lattice parameters [104].

For anatase a = b = 0.3784 nm and c = 0.9515 nm whiles for rutile a = b = 0.4593 nm and c = 0.2959 nm. The unit cell of rutile contains two TiO_2 atoms with titanium ions in the (0, 0, 0) and (1/2, 1/2, 1/2) positions and the oxygen ions in the positions ± (u, u, 0), ± (u + 1/2, 1/2-u, u) where u = 0.305 Å [105]. Each octahedron in the rutile structure shares two edges with other octahedra and forms a linear chain along the [001] direction. The chains are linked to neighbouring chains through corner sharing.

Anatase unit cell contains four TiO_2 atoms with Ti^{4+} ions in the (0, 0, 0) and (0, 1/2, 1/4) positions and oxygen ions at (0, 0, u), (0, 0,-u), (0, 1/2,1/4 + u) and (0, 1/2, 1/2-u) positions where u = 0.208 Å [105]. Each octahedron that forms anatase phase shares four edges with other octahedra resulting in zig-zag chains in the [100] and [010] directions. With regard to oxygen packing in the polymorphs, rutile presents a compact hexagonal arrangement that is almost distorted, and anatase presents a compact cubic configuration. The density of polymorphs is related to the extent of edges sharing. Due to the lower edge sharing in anatase, it presents a more open structure than rutile [106]. This configuration is responsible for the density of anatase, approximately 9% lower than rutile, as well as greater specific area [107].

The difference in the crystal structure of anatase and rutile phase accounts for the distinct chemical properties and stability presented by the phases. In general, rutile phase is stable under all conditions of temperature and pressure. Anatase phase is metastable and transforms into rutile during heating. The transformation temperature is affected by various factors such as: concentration of bulk defects, surface defects, particle size, pressure, calcination atmosphere and dopants [99].

The transformation temperature of pure anatase into rutile is a subject of controversy and several studies report various temperatures. In general, the transformation temperature starts around 600 °C [108-110]. Reported transition temperatures vary in the range of 400 to 1200 °C [99]. Hydrothermal methods enable the transformation of anatase to rutile at room temperature. Yu et al. (2001) reported that the homogeneous precipitation with precursors of $TiOCl_2$ facilitates the transformation of anatase to rutile at room temperature [111].

When heated, anatase nanocrystals transform into rutile phase only after a critical specific surface area and particle size are reached. Hence, surface energy associated with particle size influences the stability of polymorphic phases. According to Levchenko et al. (2006) anatase is stable for particles with specific surface area greater than 50 $m^2.g^{-1}$ and for rutile phase, low specific surface area nanopowders below 7 $m^2.g^{-1}$ [112].

Zhang and Banfield (2000) studied the synthesis of anatase and observed that anatase is stable for particle size smaller than 14 nm and for particle size above 35 nm, rutile phase is stable [113]. Hwu et al. (1997) also noted that for particle size greater than 50 nm, rutile phase is stable [114].

The transformation of anatase to rutile occurs by nucleation and growth of rutile particles by coalescence. Nucleation initiates at point defects, oxygen vacancies, secondary inclusions present in the interface and/or the surface of anatase.

The nucleation of rutile phase proceeds with anatase being consumed by the growth of rutile phase. For pure anatase, nucleation of rutile was observed in twin interfaces and it grows in lathes with rutile {110} planes parallel to {112} anatase planes [115].

Common structural configurations have been observed for anatase and rutile. It has been reported that the {112} oxygen planes of anatase have structural elements similar to {100} oxygen planes of rutile [116]. Through computer simulation, the interplanar spacing of the titanium matrix in the (101) plane of anatase has been observed to be close to that of (101) rutile plane. These surfaces can act as nucleating site for rutile phase provided that their activation barriers for nucleation are low. The relationship between the lattice orientation of crystalline anatase and rutile has been expressed as follows: anatase (101) plane parallel to rutile (101) and anatase <201> direction parallel to rutile <111> direction in the (101) plane of anatase [117].

Anatase-rutile transformation is also a reconstructive process, i.e. it involves the breaking and rearrangement of TiO_2 lattice structure [116]. In the process, two of the six Ti-O bonds in the structure of anatase are broken to form rutile structure, followed by the local adjustments of the atoms to accommodate the new structure. The rearrangement and transformation of anatase to rutile phase are promoted by the relaxation (decreased structural rigidity) of the oxygen lattice through oxygen vacancies [118,119]. The oxygen vacancies promote the formation of rutile. Doping of anatase with ions of lower valence than Ti also increases the level of oxygen vacancies which consequently promotes anatase transformation to rutile [120]. In this case, any condition that increases oxygen vacancies in anatase will accelerate the transformation of anatase to rutile.

2.5 Topotaxy

Topotaxy is the phenomenon of mutual orientation of different crystals resulting from chemical reaction or solid-state transformation. It can also be defined as the transformation of a parent crystal into a product of different chemical composition, without any significant change in axial direction, shape and orientation of the product crystal [121]. So, there is a reproducible relationship between the parent crystal and the product crystal. The degree of topotaxy can be measured through the difference in orientation between the

parent and product crystal. The degree of topotaxy is considered to be high when there is only change in secondary coordination without rupture of primary bonds as noted in displacive phase transformations.

With these transformations, there is structural similarity between the initial and final structures and the preservation of at least one axes of symmetry. If however the atoms arrange themselves by breaking of bonds, usually observed in reconstructive phase transformations then topotaxy is said to low [116].

The transformation of anatase to rutile involves the breaking of bonds and rearrangement of atoms in a reconstructive transformation. The transformation is affected by two factors: (1) the spatial disturbance of oxygen ions (2) the number of bonds broken. The spatial disruption of oxygen ions and the number of bonds broken must be minimal.

According to Shannon and Pask (1964), the mutual orientation and preservation of some structural elements ranks the transformation as intermediate [116]. Currently, there are limited studies on the topotaxy between rutile and anatase since the transformation has been classified as a case of intermediate topotaxy [116].

2.6 Epitaxy

Epitaxy is the growth of crystalline films on top of substrates where the substrate determines the orientation and structure of the film formed [122]. Epitaxial growth has become increasingly important for the growth of crystalline thin films with electronic, optical and magnetic properties tailored for technological applications.

For example, the production of layers of semiconductor films in integrated circuits, optoelectronic devices, solar cells andphotocatalytic films. Epitaxial films are ideal systems for the study of interfaces and processes of nucleation and growth [123].

There are two types of epitaxy: homotaxy and heterotaxy. Homotaxy occurs when the substrate material and the film are identical in terms of

chemical composition and crystalline parameters. The growth of Si films on Si substrate is a classic example. On the contrary, heterotaxy occurs when the material of the film is different from the substrate as is presented in the growth of AlAs on GaAs substrate. Usually, heterotaxy is employed to grow crystalline films of materials for which individual crystals cannot be obtained easily.

For the growth of epitaxial films there must be a well-defined crystal orientation relationship between the crystal of the film and the substrate, i.e. the crystalline structure of the film has to be almost identical to the structure of the substrate. Lattice planes and directions play a dominant role in the growth of these films and orientation relationships are affected by the lattice misfit between the substrate and film. The misfit is calculated as the difference in the lattice parameters of the substrate and the film divided by the substrate lattice parameter (Equation 2.2).

$$lattice\ misfit = \frac{b - a}{b} \tag{2.2}$$

where a = lattice parameter of film and b = lattice parameter of substrate.

Lattice misfit further affects the structural defects in the interface between the substrate and the film, film morphology and epitaxial orientation [124]. The smaller the misfit between the substrate and the film, the lower the strain during growth resulting in good interface formation.

Thermal strains arise in epitaxial films due to significant difference in thermal coefficient between the film and substrate. For many applications, minimal differences in thermal and structural properties are always desired to minimize defects and increase mobility of electrons in the interface.

The calculated lattice mismatch between anatase and rutile using lattice parameter a is about 18%. The mismatch is quite large compared to the lattice mismatch of other substrates. For example, Si (001) and $SrTiO_3$ have a 1.6% and 3% misfit with anatase phase respectively [125,126].

Theoretically, the growth of epitaxial anatase requires smaller lattice misfit between the substrate and anatase in order to stabilize the phase. However, epitaxial growth between materials of dissimilar crystal systems and apparently large misfit is possible. An example is rutile TiO_2 on hematite Fe_2O_3

where rutile is tetragonal and hematite trigonal but the similar spacing between the atoms in the (100) plane of rutile and the (001) plane of hematite induced epitaxial growth [127]. This particular case shows that structural similarities in terms of lattice planes and directions can serve as sites for epitaxial growth which could be the case of anatase on rutile.

The synthesis methods of epitaxial films include molecular beam epitaxy, liquid phase epitaxy and gaseous phase epitaxy [128,129]. Liquid phase epitaxy is more suitable for a vast range of precursors. The substrate is immersed in the precursor solution at an appropriate temperature followed by heat treatments for film growth.

Liquid phase methods are advantageous in terms of simplicity, high deposition rate, high crystallinity of the films, stoichiometry control, low defect concentration and cost efficient. The epitaxial growth relationship between anatase and rutile has not been reported due to the limited use of rutile substrate.

3 MATERIALS AND METHODS

This section introduces the methodology and materials required for the preparation of supported anatase film on dense rutile substrate. It focuses on the synthesis of Ti^{4+} precursor resin, powder pressing, sintering of compact rutile (TiO_2) substrates and film deposition by spin coating. Further into the section, characterization techniques are also outlined.

3.1 Materials

Rutile titanium dioxide pigment, Dupont R-902+ was used as raw material for the substrates. It has a purity of 93% with traces of alumina, amorphous silica and carbon black undertone. A binder, Dextrin is also used during pressing. The raw materials for the Ti^{4+} precursor resin are as follows: Titanium Isopropoxide ($Ti[OCH(CH_3)_2]_4$) 97% purity (Aldrich), monohydrate citric acid ($C_6H_8O_7.H_2O$) 99.5% purity (Nuclear) and Ethylene glycol ($C_2H_6O_2$) 99.5% purity (Vetec). Rhodamine B 95% purity (Sigma) and Atrazine (Sigma-Aldrich) were chosen as substrates for the photocatalytic tests.

3.1.1 Rhodamine B

Rhodamine B (Rhod-B) is a dye with a central xanthene chromophore group [130]. Figure 3.1 shows the chemical structure of the xanthene group and Rhod-B with the attached functional groups.

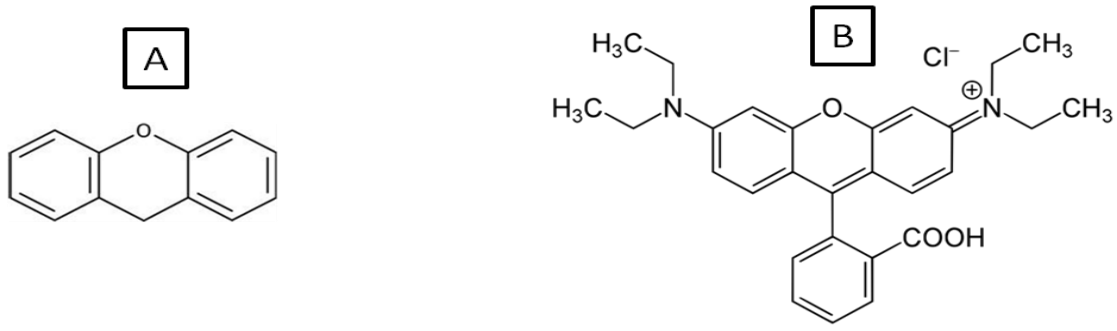

Figure 3.1 - The chemical structure of *A)* Xanthene chromophore; *B)* Rhod-B [130].

Rhod-B is one of the most utilized dyes for measuring the photocatalytic activity of novel catalysts. In some cases, it serves as a model to test the remediation of water contaminated with xanthenes dyes. A dye should be employed as a model to test a catalyst in situations where the degradation of the specific dye is the focus of the study in order to avoid generalized assumption of the photoactivity of a catalyst [131]. The evaluation of catalysts using dyes has been criticized by Rochkind et al. (2015) especially for catalysts with enhanced properties in the visible region [131]. Dyes in virtue of visible light irradiation undergo dye sensitization mechanisms which contribute to part of the photocatalytic oxidation of the dye, a condition where true photocatalytic activity of the catalyst cannot be properly evaluated. The use of dyes is encouraged for the evaluation of UV photoactivity of catalyst and the study of specific dye degradation. Accordingly, Rhod-B was employed for the evaluation of UV photoactivity of the prepared catalyst.

3.1.2 Atrazine

Atrazine (2-chloro-4-(ethylamino)-6-(isopropylamino)-s-triazine) is a very important herbicide recognized as efficient in exterminating weeds that emerge during the production of crops such as corn, cotton, sorghum and sugarcane [132]. It belongs to a subset of compounds called s-triazine. The s-triazines have a basic structure unit consisting of three carbon atoms and three nitrogen atoms in a close hexameric symmetric ring, in which each carbon atom is linked to an adjacent nitrogen atom through alternating single and double bonds (Figure 3.2).

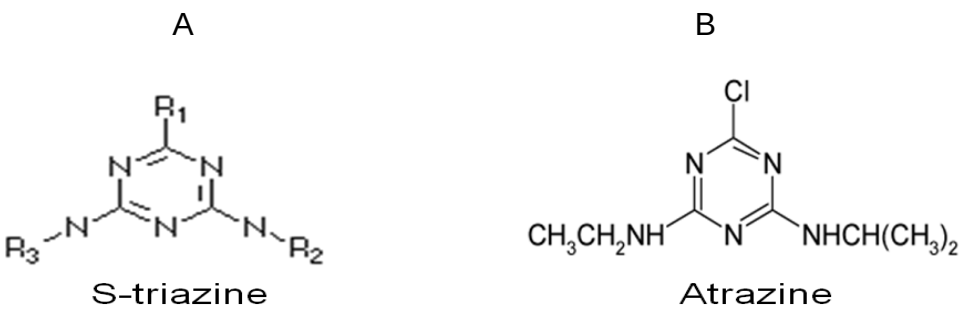

Figure 3.2 - The chemical structure of *A)* S-triazine; *B)* Atrazine [132].

The carbon atoms in the ring form bonds with side chains containing functional groups (R_1, R_2 e R_3). The chemical properties of s-triazines are controlled by the substituted groups. Atrazine has Cl, C_2H_6 and C_3H_8 as functional groups in the R_1, R_2 and R_3 positions respectively (Figure 3.2B).

Atrazine (ATZ) is a common source of water pollution associated with agricultural practices. Atrazine molecules are transported into groundwater and water bodies either by runoff of Atrazine bound soil particles or by leaching. The properties of ATZ (water solubility, vapor pressure, chemical structure) account for its high persistence in water. Figure 3.3 shows the degradation pathways of ATZ.

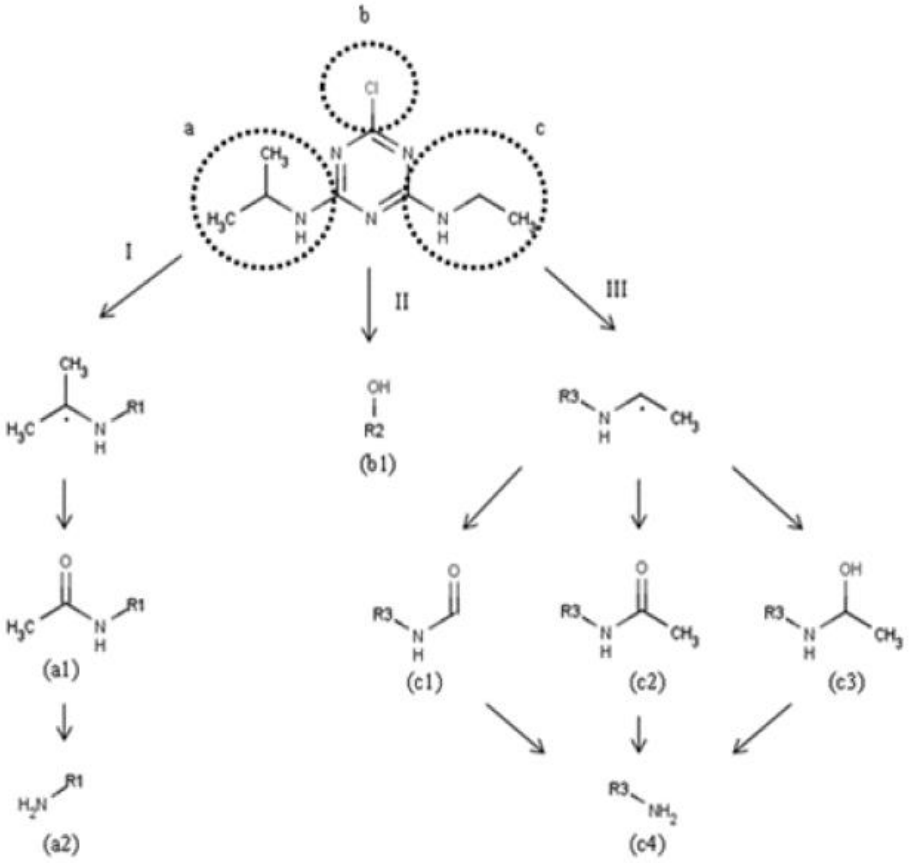

Figure 3.3 - Atrazine degradation pathways through chemical modification of the three major functional groups *I)* Isopropylamino *II)* Chloro *III)* Ethylamino [133].

The decomposition of ATZ occurs by three major paths dependent on functional group: (a) Isopropylamino (b) Chloro and (c) Ethylamino. The

degradation of ATZ is complex mainly due to the nature of the functional groups which results in several transformations of the herbicide and formation of numerous byproducts [133].

3.2 Uniaxial pressing

Ceramic conformation methods are selected such that they are feasible with final product geometry, dimensional tolerance, properties and applications. As mentioned previously, this project aims at producing dense circular substrates to support anatase films. Powder pressing is a simple shaping technique for obtaining the required geometry and properties of the substrates. The rutile powder for the substrates was characterized and prepared for pressing. A first batch of substrates was pressed for the sole purpose of constructing a compaction curve. From the compaction curve, a compacting pressure was chosen for the pressing of the second batch of substrates utilized for the project.

3.2.1 Characterization and preparation of rutile powder

3.2.1.1 X-ray diffraction (XRD)

In order to certify the content of the as-received rutile powder, XRD was utilized. With this method, the chemical composition, crystalline structure and the phase composition of the powder can be verified. The powder was analyzed in an X-ray diffraction equipment (ULTIMATE IV Rigaku, Institute of Physics São Carlos-University of São Paulo) and the spectra were collected with a Cu ($\lambda_{Cu\text{-}K\alpha}$, 0.154 nm) anode, from 2θ = 20 - 80° with a step of 0.02° and speed of $2°.min^{-1}$.

The properties of the powder were extracted from the resulting diffractogram with the help of a crystallographic database (Joint Committee on Powder Diffraction Files- JCPDF) and Match software. The crystallite size of the powder was estimated by the Scherrer formula (Equation 3.1) [134].

$$d = \frac{0.9\lambda}{\beta \cos\theta} \quad (3.1)$$

where d is crystallite size, λ is the X-ray wavelength (0.154 nm), θ is the Bragg angle (degrees), and β (radian) is the full width at half maxima of the diffracted peak.

With this formula, the full-width at half-maximum (β) of the broadening of each diffracted peak was calculated and an average crystallite size was determined.

3.2.1.2 Brunauer, Emmett and Teller (BET) specific surface area

To determine the BET specific surface area by N_2 adsorption, Micrometrics ASAP 2000 equipment available at Embrapa Instrumentation São Carlos was utilized. Figure 3.4 shows the Micrometrics ASAP equipment.

Figure 3.4 - Micrometrics equipment utilized for the measurement of BET specific surface area.

The BET method (Brunauer-Emmett-Teller) depends on nitrogen isotherms produced by pressure variations of a powder due to liquid nitrogen adsorption (77K) [135]. From the isotherms and mathematical models, the specific surface area (BET) of the rutile powder was estimated.

Assuming that the rutile powder consists of spherical particles, its crystallite size can be estimated by Equation 3.2:

$$d = \frac{6000}{\rho . S} \quad (3.2)$$

where

d= particle diameter;

p= theoretical density of TiO_2 rutile (4.23 $g.cm^{-3}$);

S= BET specific surface area.

3.2.1.3 Scanning electron microscopy (SEM)

The morphology and particle size of the powder were verified by SEM images taken with a JEOL SEM 6310 microscope (Embrapa Instrumentation São Carlos). The particle size and distribution were estimated from the SEM micrographs. Each particle in the micrograph was manually measured using Image J software and a frequency count was done.

3.2.1.4 Dynamic light scattering (DLS)

The particle size and distribution of the powder are important properties that control powder flow, packing density and reactivity during sintering. Dynamic light scattering technique was employed to measure the particle size of the dispersed powder in solution.

In general, particles in solution tend to undergo Brownian motion and their velocities can be related to their size. In general, smaller particles scatter less light in comparison to larger particles due to their faster translational diffusion.

The fluctuation in light scattering intensity (D) is associated to size and diffusion speed through the Einstein-Stokes equation (Equation 3.3) [136].

$$D = \frac{kT}{6\pi D\eta} \quad (3.3)$$

where

D is hydrodynamic diameter;

k is Boltzmann constant;

T is absolute temperature;

η is the viscosity of the solvent.

The hydrodynamic diameter is the sphere that diffuses at the same speed as the measured particle. The result is presented as a graph of intensity distribution versus particles in solution. For the measurement, a solution of the powder with 0.1 $mg.L^{-1}$ concentration was prepared using water as solvent. The solution was placed in a polystyrene cuvette which was then inserted into a Malvern Zetasizer Nano ZS equipment available at Embrapa Instrumentation São Carlos (Figure 3.5).

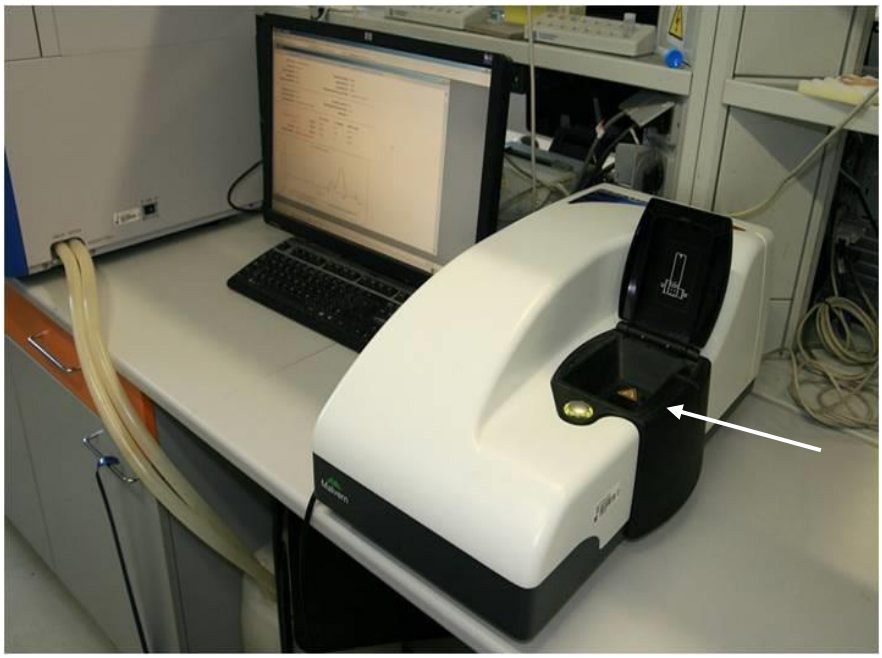

Figure 3.5 – A sample Malvern Zetasizer Nano ZS equipment showing where the curvette is inserted (Choboticks Chemical Robotics).

A monochromatic laser was passed through the solution and the number or volume of particles against hydrodynamic diameter is provided as a result.

Although the properties measured are related to the rutile powder dispersed in water, they can provide qualitative information about the powder.

3.2.2 Uniaxial pressing of the substrates

The pressing of the powders was done in a uniaxial press with 5 ton force capacity. Figure 3.6 shows the uniaxial press (Ceramics laboratory, Materials science and engineering department, UFSCar) employed for the compaction of the prepared powder for the substrates.

Figure 3.6 - Uniaxial pressing machine utilized for the compaction of the substrates.

For the preparation of the powder for pressing, it was mixed with Dextrin (0.5% by weight) and water (3% by weight) to improve the flow properties of the powder for die filling. The prepared powder was passed through a 300 mm mesh.

In order to attain dense sintered bodies, high green density must be taken into consideration. Compacting pressure is one of the factors that control green compact density. The effect of pressure on green compact density is perceived through the application of various pressures and the measurement of resultant green density.

Seven compacting pressures of 62, 78, 94, 109, 125, 140 and 156 MPa were selected. For each compacting pressure, five substrates were assigned. For each substrate, 2.5 g of powder was poured into a circular die with an inner

diameter of 20 mm and was pressed unaxially at the mentioned pressures.Thus, seven groups of five compacts were prepared in total.

3.2.2.1 Measurement of Physical properties and Selection of compacting pressure

The densities of the green compacts were measured by the mass/volume technique where mass, diameter and width were taken for the estimation of density. Green density was divided by the theoretical density of rutile TiO_2 (4.23 $g.cm^{-3}$) to obtain relative density.

A compaction curve was constructed by plotting the average relative density of the green compacts in each group versus the compacting pressure applied.

The compacts were dried at 100 °C/24h and sintered at 1450 °C/2h at a ramp rate of 5 $°C.min^{-1}$. Figure 3.7 shows the appearance and dimensions of a sample taken from the sintered substrates.

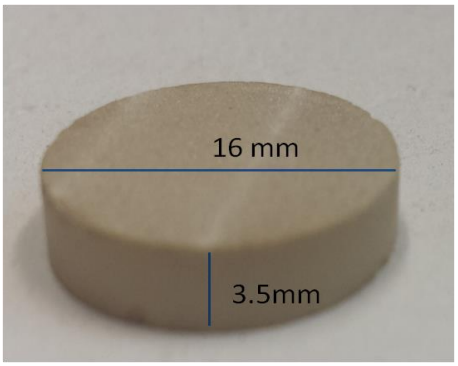

Figure 3.7 - Sintered rutile substrate.

3.2.2.2 Measurement of physical properties of the sintered substrates and selection of compacting pressure

Density after sintering was estimated based on the Archimedes principle. The dry mass (M_d) of the sintered substrates, saturated mass after immersion in

water for 24 hours (M_{sat}) and the suspended mass (M_{susp}) of the substrate by Archimedes method were measured. The properties were correlated to apparent density through Equation 3.4:

$$\rho = \left(\frac{M_d}{M_{sat} - M_{susp}}\right) . \rho_{H_2O} \quad (3.4)$$

where ρ is apparent density, M_d is dry mass after sintering, M_{sat} is the saturated mass after immersion in water, M_{susp} is the suspended mass in water based on Archimedes principle and ρ_{H2O} is the density of water. To obtain relative density, the apparent density value was divided by the theoretical density of rutile TiO_2 (4.23 $g.cm^{-3}$).

Shrinkage was calculated according to Equation 3.5:

$$S = \left(\frac{d_g - d_s}{d_g}\right) * 100 \quad (3.5)$$

where S = shrinkage; d_g = diameter of green body; d_s = diameter after sintering.

To calculate water absorption, the dry mass of the substrates and mass after immersion in water for 24 hours were utilized. The amount of water absorbed was estimated according to Equation 3.6:

$$A = \left(\frac{M_{sat} - M_d}{M_d}\right) * 100 \quad (3.6)$$

where A is water absorption; M_d is dry mass after sintering; M_{sat} is the saturated mass after immersion in water.

Apparent porosity was calculated using Equation 3.7:

$$P = \left(\frac{M_{sat} - M_d}{M_{sat} - M_{susp}}\right) * 100 \quad (3.7)$$

where P is apparent porosity; M_d is dry mass after sintering; M_{sat} is the saturated mass after immersion in water and M_{susp} is the suspended mass by immersion technique based on Archimedes' principle.

Green density and physical properties were utilized as criteria for selecting the compacting pressure of the next set of substrates for the project. After the definition of the compacting pressure, forty substrates were uniaxially

pressed. Green densities of the substrates were estimated and after, the substrates were sintered at 1450 °C/2h. The physical properties (relative density, apparent porosity, water absorption and shrinkage) of the substrates were measured as previously described. A number of techniques were utilized to further characterize the substrates. For this purpose, a substrate was selected randomly.

3.2.2.3 X-ray diffraction

Although the raw material for the substrates was rutile, during sintering, many reactions can occur that may alter the phase composition of the sintered body. Therefore, the phase formed after sintering was verified by XRD. The analysis was carried out in a Shimadzu XRD 6000 equipment (Embrapa Instrumentation São Carlos) and the spectra were collected with a Cu ($\lambda_{Cu\text{-}K\alpha}$, 0.154 nm) anode, from 2θ = 20 - 80°, at $2°.min^{-1}$.

3.2.2.4 Scanning electron microscopy

Microstructure of the substrate related to grain morphology, grain size and pores was observed by scanning electron microscope (JEOL SEM 6310). Prior to the analysis, the surface of the substrate was polished with an alumina abrasive paper. The polished surface was thermally etched in a muffle at 1350 ^{o}C/1h to enhance microstructural features for observation.

3.2.2.5 Atomic force microscopy

The topology of a substrate to some extent controls the properties of deposited films since it serves as a base for structural growth. Not only can the technique provide information on the topography of a surface but also estimates surface roughness. In order to map the surface of the substrates, an atomic force microscope (Reevo V dimension, Embrapa Instrumentation São Carlos)

was employed. The images were taken in the tapping mode where a silicon tip was attached to a microcantilever whose spring constant is 48 $N.m^{-1}$ and resonance frequency is 190 K.Hz.

3.3 Polymeric precursors method

The polymeric precursor method is one of the variations of sol-gel synthesis method, a wet chemical route for obtaining nanometric and sub-micrometric oxide powders. The success of the polymeric precursors method lies in the fact that it is compatible with a wide range of oxides and presents few process parameters. The concept underlying the polymeric precursor method is summarized as follows:

i) the ability of hydrocarboxylic acids (citric acid, etcetera) to form stable complexes with metal cations in solution (Figure 3.8);

ii) esterification of metallic complexes (polymeric precursors) by the addition of alcohol (Ethylene glycol) which results in a resin containing dispersed cations (Figure 3.9);

iii) finally, the thermal treatment of the resin [137].

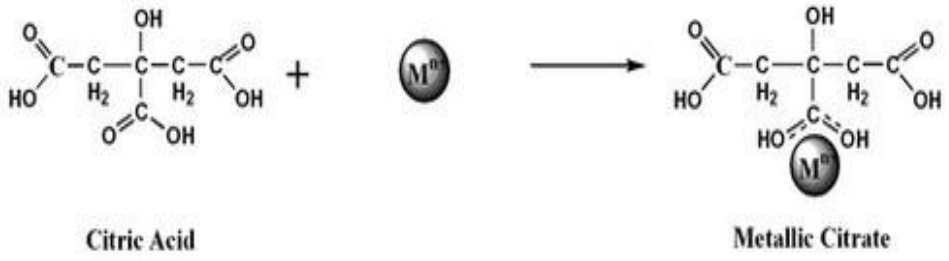

Figure 3.8 - Formation of metallic citrate [137].

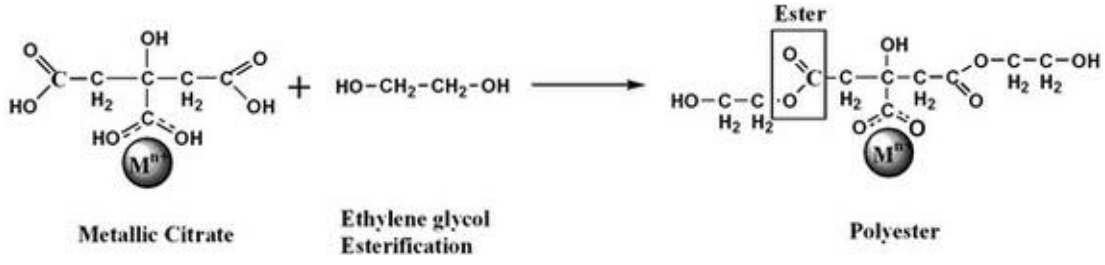

Figure 3.9 - Polymerization of metallic citrate [137].

The polymeric network is particularly important as it ensures minimal segregation of the ions during heat treatment. Some of the distinct characteristics of powders obtained via this method are homogeneity at molecular level and controlled stoichiometry – which are particularly important for complex oxide powders and mixed phase powders.

3.3.1 Synthesis of Ti^{4+} precursor resin

A solution of citric acid, a chelating agent, was prepared and maintained at 70 °C. Titanium isopropoxide (Ti^{4+} precursor) was added to the citric acid solution upon stirring, in a molar ratio of 1:3 respectively, forming titanium citrate (complex). The resultant solution was polymerized by esterification. This was done by adding ethylene glycol to the solution, where the molar ratio of ethylene glycol to citric acid was 2:1. The polymerized solution was then transferred to a reflux condenser, where it was kept at 120 °C for 24 hours until a resin was formed. Excess water was eliminated to adjust the viscosity of the resin.

Figure 3.10 presents the flow chart of the synthesis process of Ti^{4+} precursor resin.

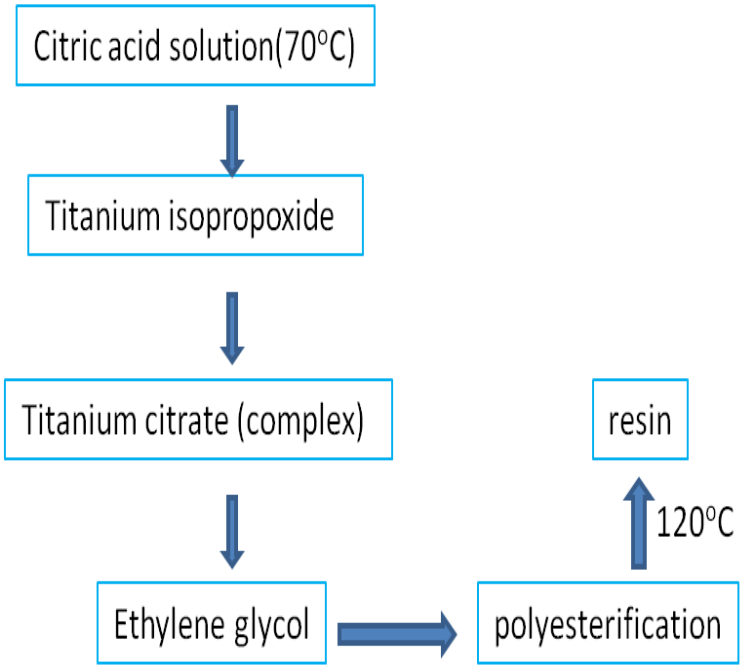

Figure 3.10 - Flow chart for the synthesis of the Ti^{4+} resin.

3.3.2 Resin characterization

3.3.2.1 Loss on ignition

Loss on ignition is a simple technique which provides an approximate estimate of the quantity of inorganic and organic content in a given material. It is based on the measured weight loss after ignition at a temperature enough to volatize components that are not desired. The quantification of inorganic content of precursors is of interest especially in film catalysts because it provides information on the cation concentration in a volume of resin. As such, loss on ignition test was carried out on the Ti^{4+} polymeric precursor resin to estimate the concentration of Ti^{4+} cations.

For the test, three crucibles were ignited at 1000 °C/5h in a muffle furnace in order to remove any impurities therein. The empty crucibles (C) were weighed and approximately 2g of resin was placed in each crucible. The crucibles with resin were weighed (C_{resin}) before ignition at 850 °C for 4 hours. After ignition, the weight of the crucibles with residue ($C_{residue}$) was noted. Based on the ignition temperature, the residue formed can be assumed as TiO_2 and the percentage loss on ignition is calculated using Equation 3.8:

$$\%wloss = \frac{C_{resin} - C_{residue}}{C_{resin} - C} \tag{3.8}$$

where w is weight; C is weight of empty crucible; C_{resin} is weight of crucible with resin and $C_{residue}$ is weight of the crucible with residue.

To find the concentration of Ti^{4+} in the resin, the calculated percentage loss on ignition was converted into concentration ($g.L^{-1}$) using the molar mass of TiO_2, density of ethylene glycol and volume of resin used for the test.

3.3.2.2 Brookfield Viscosity

In film processing, resin viscosity controls film thickness and the ease of coating. Viscosity values up to $3.20x10^6$ centipoises (cP) can be measured with

a Brookfield viscometer depending on the model. Brookfield viscosity is obtained by measuring the torque produced by a moving spindle in a fluid at constant speed. This torque depends on the resistance of the spindle to rotational movement a result of the fluid. Thus, the viscosity of the fluid is calculated in function of the toque and spindle properties (speed, size and shape). To measure the viscosity of the Ti^{4+} precursor resin, a spindle 18, a speed of 30 rpm and temperature of 25 °C were selected. The viscometer was programmed to rotate the spindle at 30 rpm for 1 min.

3.3.2.3 X-ray diffraction

A volume of the resin was separated into four parts and each part was calcined in air at a specific temperature, the same temperature at which the posterior precursor films will be calcined. The calcinations were done in two thermal cycles. The first cycle was heating to a ramp of 150 °C at a ramp rate of $1°C.min^{-1}$ and 2 hours dwell time. After, the temperature is further raised at a ramp rate of 1 $°C.min^{-1}$ to the final calcination temperature and dwell time: the conditions were 350 °C/12h, 400 °C/2h, 450 °C/2h and 500 °C/2h. The powders were cooled at the same ramp rate to room temperature (30 °C).

The as-prepared powders were submitted to XRD in a Shimadzu 6000 equipment (Embrapa Instrumentation São Carlos) with a Cu ($\lambda_{Cu\text{-}K\alpha}$, 0.154 nm) anode in order to detect the major phase in the powders. It is important that the precursor resin form pure anatase in order to eliminate the influence of contaminant phases on the growth of the TiO_2 films.

3.4 Film deposition

3.4.1 Spin coating

Spin coating is a technique for depositing films whose precursors are derived from wet chemical routes for example, sol-gel, Pechini and polymeric precursors method. The process of producing films from wet chemical routes

combined with spin coating is simple and the reproducibility of the process is very good. Compared with other deposition techniques, it is cost efficient and the process parameters can be easily controlled. Also, the number of film layers is not a limiting factor. Due to these advantages, spin coating was opted for the deposition of the films on rutile substrate and glass substrate. Figure 3.11 shows the main stages of the process.

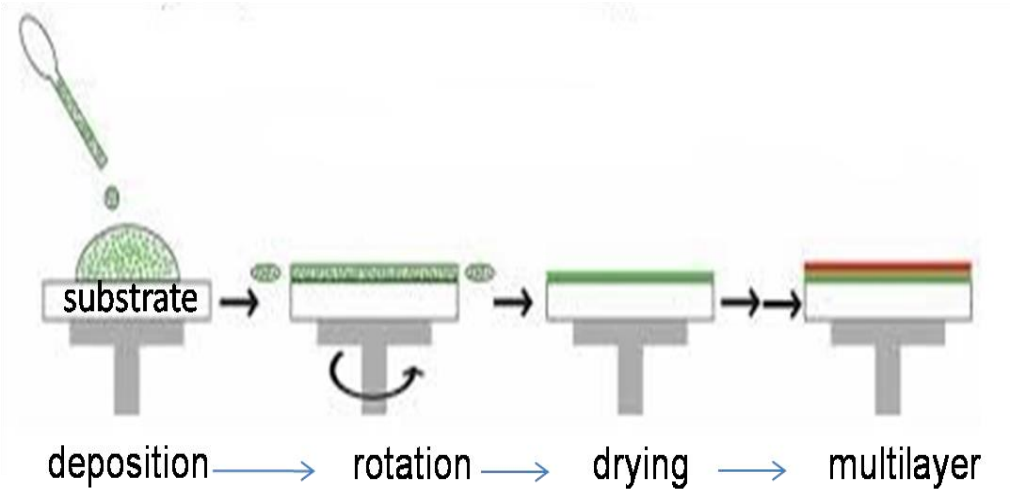

Figure 3.11 - Spin coating process [138].

In the first stage, a quantity of the precursor is deposited onto the center of the substrate. The quantity deposited should be sufficient to ensure that in the next stage of the process, the whole substrate will be coated. Also, the viscosity and wettability of the solution must be such that it easily spreads over the substrate and maintain good adhesion with the substrate [139]. For the next stage, the substrate with the fluid is then rotated at a defined speed and time resulting in a centripetal force that causes the film to spread homogeneously on the substrate and at the same time remove excess material. Therefore, the quality and thickness of the film do not only depend on the parameters of the spin coating process (rotation speed and time) but also on the properties of the precursor such as viscosity, quantity of precursor and superficial energy.

The numerous parameters involved at the rotation stage makes it crucial for the properties of the film as the likelihood for defects is mainly encountered here. The third stage is characterized by drying, where excess fluid is

evaporated from the film and the film is further thinned. Drying is an optional stage. For multilayered precursor film, another layer is deposited on the dried film and the process is repeated until the desired number of layers is formed.

3.4.2 Films on glass substrate

Here, TiO_2 films were deposited on glass supported rutile films. In an attempt to reproduce rutile substrate on glass, a solution was prepared from the rutile powder. A volume of the solution was deposited onto the glass substrate which was held in place by a substrate holder in a Model 400B-66NPP/LITE spin coater (Embrapa Instrumentation São Carlos). Figure 3.12 presents the spin coater and substrate holder.

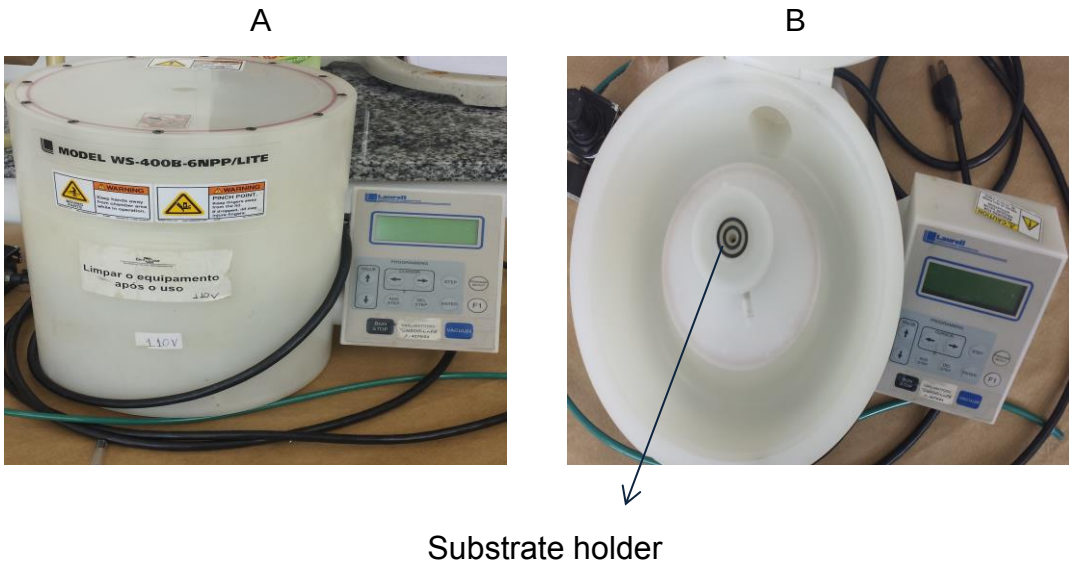

Figure 3.12 - Spin coater Model 400B-66NPP/LITE *A)* closed; *B)* open exhibiting the substrate holder.

The glass substrate was spinned at 3000 rpm for 30 s followed by 6000 rpm for 30 s in order to remove excess solution and to form a uniform layer on the substrate. Here, drying of the films was not done in between layers. Subsequent four layers were formed in the same manner resulting in five layers on the substrate. Four additional glass substrates with rutile films were prepared and the resultant multilayered rutile films were calcined in air at 550 °C/2h in

two steps: a ramp rate of 1 °C.min^{-1} to 150 °C with 2 hours dwell time followed by a ramp rate of 1 °C.min^{-1} to 550 °C with 2 hours dwell time. After, the glass substrates with rutile films served as substrates for the deposition of the TiO_2 precursor film.

For the deposition of the precursor films, a quantity of the precursor resin was deposited on the as-prepared glass supported rutile films and the substrate was spinned at 3000 rpm for 30 s followed by 6000 rpm for 30 s. The process was repeated to form five multilayers on each of the four substrates. Once again, drying was not done in between layers. Each substrate with the films was calcined at: 350 °C/12h, 400 °C/2h, 450 °C/2h and 500 °C/2h where an initial ramp of 150 °C/ 2h and ramp speed of 1°C.min^{-1} were respected.

The samples were designated according to calcination temperature and G stands for glass: G350, G400, G450 and G500. The glass substrate with only rutile film was identified as SUB.

3.4.3 Films on sintered rutile substrate

For the deposition of the multilayered Ti^{4+} precursor films (10 layers), a volume of the precursor resin was deposited on the substrate. Then, the substrate was spinned at 3000 rpm for 30 s followed by 6000 rpm for 30 s, after which the first layer was formed.

The second layer was deposited using the same procedure but this time, the coated substrate was dried at 80°C for 5 minutes before the next layer was deposited. In summary, at the end of every even numbered layer deposition (layers 2, 4, 6, 8), the coated substrate was dried. The process was repeated until 10 layers were obtained.

A total of four samples were prepared. Each sample was calcined at a specific temperature and time condition: 350 °C/12h, 400 °C/2h, 450 °C/2h and 500 °C/2h where an initial ramp of 150 °C/2h and ramp speed of 1°C.min^{-1} were respected. The as-prepared films were named according to their calcination temperature in ascending order: SAM 1, SAM 2, SAM 3 and SAM 4. The pristine substrate was named SUB.

3.5 Characterization of films on glass substrate and rutile substrate

3.5.1 X-ray diffraction

The phase composition and phase transformation of the TiO_2 layer both on the substrate and glass were verified by XRD. The diffractions were done in a Rigaku RU200B model equipment at the Institute of Physics São Carlos (University of São Paulo) with a Cu ($\lambda_{Cu\text{-}K\alpha}$, 0.154 nm) anode. The scan range was 2θ = 20-80° and a scan speed of $1°.min^{-1}$ were respected. The crystallite sizes of the films on rutile substrate were estimated by the Scherrer formula.

3.5.2 Grazing incidence X-ray

In order to isolate the effect of the substrate on the phase analysis of the films, a grazing incidence angle of 2° was employed. The diffractions were carried out in a Rigaku RU200B model equipment at the Institute of Physics São Carlos (University of São Paulo) with a step scan mode of 0.02° at a speed of 1 $min.step^{-1}$ from 2θ = 15 - 30°.

The condition for the films on rutile substrate was grazing incidence angle of 2° , step scan mode of 0.02° at $15s.step^{-1}$ from 2θ = 20 - 80°. Crystallite size of the films on rutile substrate was estimated by the Scherrer formula.

3.5.3 Micro-Raman

The phase composition of the substrate and films was carried out by micro-Raman spectroscopy.

For the analysis, a Horiba Jobin Yvon HR550 model spectrometer (Interdisciplinary Laboratory of Ceramics and Electrochemistry (LIEC), UFSCar) with a charge coupled detector (CCD) cooled by a Peltier system (-70°C) was utilized. The substrates were excited at 514 nm wavelength radiation whose beam power is 7 mW.

3.5.4 Atomic force microscopy

The surface topography of the films formed as well as their roughness was observed by atomic force microscopy employing a Reevo V dimension microscope (Embrapa Instrumentation São Carlos). The images were taken in the tapping mode and the readings were done with a microcantilever (Silicon tip) whose spring constant and resonance frequency are 48 $N.m^{-1}$ and 190 K.Hz respectively.

3.5.5 Scanning electron microscopy

The morphology and homogeneity of the films on both substrates (rutile and glass) were observed by a scanning electron microscope. It provides information on the microstructural differences associated with calcination temperature and substrate.

The analysis of the films on glass were done in a JEOL SEM 6310 microscope (Embrapa Instrumentation São Carlos) while that of the films on rutile were done in a FEI Magellan 400 L microscope (Structural Characterization Laboratory (LCE), UFSCar). Apart from the general microstructural imaging, SAM 1 and SAM 2, both films on rutile substrate were fractured for cross sectional analysis by Field emission gun microscopy (FEG-SEM) and SEM respectively for the determination of film thickness.

After, a line energy dispersive X-ray spectroscopy (EDX) was performed in the region of the film for only SAM 2 to verify the certainty of the width estimation with respective to chemical composition. The thickness of the films on glass was not measured since it is not within the interest of the study.

3.5.6 UV-visible Diffuse reflectance

When a solid is illuminated with light, its optical properties determine the fate of the incident light. The response of the material will depend on the degree of absorption, transmission and reflection. For opaque materials, most of the

light incident is reflected on the surface. Diffuse reflectance spectroscopy focuses on the study of the optical and electronic properties of materials based on the amount of reflected light in different directions [140]. Accordingly, the optical properties of pristine rutile substrate and the films supported on rutile substrate were evaluated. The measurements were carried in a UV-vis NIR Cary 5G spectrometer (LIEC, UFSCar) operating in diffuse reflectance mode in the range of 200 to 800 nm.

3.6 Preparation of anatase-rutile powder samples

The properties of the substrate such as height and hardness limit the techniques by which it can be characterized. For example, the films were not analyzed by transmission electron microscope because the preparation of the films for analysis is very complex.

Since important properties of the films can be deduced from this technique, powder samples were produced. A convenient method is to dissolve the rutile powder in the resin. This decision was taken based on the analysis of the crystallite size of the resin powders and rutile powder, which showed a considerable difference in size. Thus, a mixture of the two could either result in rutile particles surrounded by anatase particles or anatase on top of rutile particles.

To prepare the powder samples, a quantity of rutile powder was dissolved in a volume of resin under magnetic stirring and the mixture was stirred for 24 hours. The mixture was divided into five parts and each part was calcined at a specific temperature. The temperature and time conditions used were identical to the films: 350 °C/12h, 400 °C/2h, 450 °C/2h and 500 °C/2h where an initial ramp of 150 °C/2h and ramp speed of 1 $°C.min^{-1}$ were respected.A part was calcined at 1000 °C/2h with the intuition that at this temperature all anatase phase transforms into rutile phase. So, it serves as a very good base for comparing the mixed phase powders. The powders were named according to their calcination temperature: P350, P400, P450, P500 and P1000.

3.6.1 Characterization of anatase-rutile powder

3.6.1.1 Micro-Raman

Micro-Raman was employed to verify the phases present in the mixed phase powder. The spectra were collected with a Horiba Jobin Yvon HR550 model spectrometer (LIEC, UFSCar) equipped with a charge coupled detector (CCD) detector cooled by Peltier system at a temperature of -70°C. The substrates were analyzed with wavelength radiation of 514 nm and 17 mW power.

3.6.1.2 Scanning electron microscopy

SEM micrographs were taken of sample P450 powder utilizing a JEOL SEM 6310 microscope (Embrapa Instrumentation São Carlos). The microstructure of the sample powder, P450 was analyzed by SEM to certify if it is indeed viable to correlate properties measured in the powder with that of the film on rutile substrate.

3.6.1.3 Transmission electron microscopy

Transmission electron microscopy (TEM) is a useful tool for obtaining detailed information on the microstructure and phase distinction of the powder at high resolution. In fact, the identical composition of anatase and rutile makes their phase distinction in microscopy limited. Transmission electron microscope utilized in the dark field mode produces a contrast image where anatase particles from rutile particles could be identified. Besides, bright field image coupled with electron diffraction, allows the identification of the type of interface formed between the phases and if the films present any form of oriented nucleation and growth. It also reveals particle morphology.

The microstructure of the TiO_2 powder was analyzed by TEM in a Philips CM 120 transmission electron microscope (LCE, UFSCar) operating at 120 kV. Electron diffractions were done at selected areas to obtain structural information as well as orientations between crystals.

3.7 Photocatalytic test

One of the essential properties of a photocatalyst is the ability to produce radicals responsible for the oxidation of organic or inorganic compounds when irradiated by a light source. The direct quantification of radicals formed on a semiconductor surface upon irradiation is not trivial as such a simple qualitative method is to irradiate a semiconductor immersed in an aqueous solution of a known molecule (photocatalytic test).

The reduction in the molecule`s concentration with time can be monitored and directly associated with the semiconductors' efficiency. UV-vis spectroscopy is a convenient technique for identifying molecules in solution and measuring changes in concentration through absorption spectrum.

Absorbance is measured along various wavelengths resulting in a continuous spectrum which is specific to a molecule. Hence, the reduction in the absorbance of a molecule at a particular wavelength over time can be related to the reduction in concentration of the molecule in solution. Majority of photocatalytic tests are performed in photoreactors.

Although there are several variations in photoreactors, they are designed to provide maximum illumination and isolation from external light. All photocatalytic tests that will be presented hereafter were performed in a photocatalytic reactor built by Embrapa Instrumentation São Carlos. The photoreactor allows the modification of temperature, type of illumination and intensity.

Figure 3.13 shows the photoreactor utilized for the photocatalytic tests.

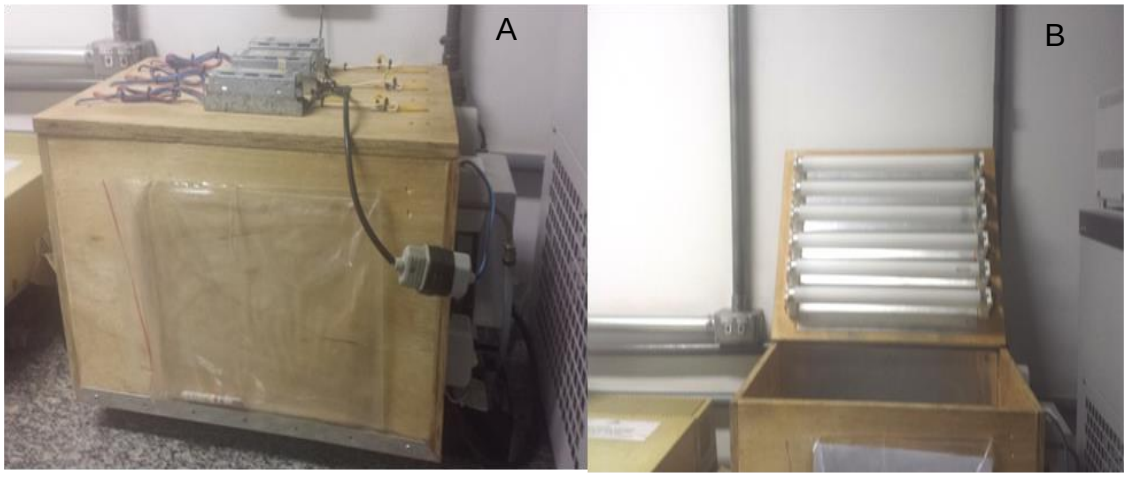

Figure 3.13 - Photoreactor *A)* closed *B)* open.

The photoreactor is composed of a wooden container whose two interior faces are covered with aluminum panels.The lid of the container is equipped with ballasts (exterior) and six sockets for lamps (interior). The outlets of the reactor are connected to a thermostatic bath and a fan in order to regulate temperature.

The photocatalytic efficiency of the films on rutile substrate in degrading Rhodamine B (dye) and Atrazine (herbicide) under ultraviolet light was evaluated. The test solutions were Rhodamine B solution (2.5 $mg.L^{-1}$) and Atrazine solution (1 $mg.L^{-1}$). The photocatalytic tests were divided into two sessions according to test solution; Rhodamine B (UV light) and Atrazine (UV light). For each session, four repetitions were done and the corresponding kinetic constants were calculated. Below is a detailed description of the experimental set up for the photocatalytic tests and the evaluation of photocatalytic activity.

3.7.1 Rhodamine B degradation

A solution of Rhod-B (2.5 $mg.L^{-1}$) was prepared and six beakers were filled with 20 mL each. In four of the beakers, a specific film was submerged: SAM 1, SAM 2, SAM 3 and SAM 4 where an ascending order in synthesis temperature was followed (350 °C, 400 °C, 450 °C and 500 °C). The Rhod-B

solution with no film was designated RHOD and the solution with a submersed pristine substrate was called SUB.

The solutions were then placed in a photoreactor equipped with six UVC lamps (TUV Philips, 15 W, with maximum intensity at 254 nm) where they were irradiated for 3 hours at 19 °C .During this period, aliquots of 3 mL were taken from each solution in intervals of 30 minutes for UV-vis measurements (Shimadzu-UV-1601 PC spectrophotometer). After the runs, the aliquots were returned into the beakers for further irradiation. The measurements focused mainly on monitoring the Rhod-B absorption peak at approximately 554 nm and a decrease of the latter with time was related to photodegradation.

The photocatalytic efficiency and stability of films after repeated use are very important properties to be considered in long term applications such as water plants. A very simple way to predict these properties is to test the films in cycles of photocatalytic tests where cycles refer to the number of times a catalyst has undergone photocatalytic test. Taking this into consideration, the anatase films were subjected to four cycle tests. Before a new cycle, a previously used film was washed thoroughly with water, ultrasonicated in water and then dried (40 °C). Also, a new testing solution was prepared for each cycle.

3.7.2 Atrazine degradation

An aqueous solution of Atrazine (1 $mg.L^{-1}$) was prepared and six beakers were filled with 20 mL each of the solution. In four of the beakers, a specific film was immersed: SAM 1, SAM 2, SAM 3 and SAM 4 where a descending order in synthesis temperature (350 °C, 400 °C, 450 °C and 500 °C) was followed. The beaker containing ATZ solution with no film was designated ATZ and the beaker with a submersed pristine substrate was called SUB.

The solutions were then placed in a photoreactor equipped with six UVC lamps (TUV Philips, 15 W, with maximum intensity at 254 nm), where they were irradiated for 5 hours at 19 °C. During this period, aliquots of 3 mL were taken from each solution in intervals of one hour for UV-vis measurements

(Shimadzu-UV-1601 PC spectrophotometer, Embrapa Instrumentation São Carlos). After the runs, the aliquots were returned into the beakers for further irradiation. The measurement focused mainly on monitoring the Atrazine absorption peak at 223 nm and 263 nm. The stability and efficiency of the films were evaluated for four cycles. For every cycle, a new solution was prepared and a previously used film was washed thoroughly in water, ultrasonicated in water and then dried (40 °C) prior to any photocatalytic test.

3.7.3 Determination of rate order

Chemical reactions can be classified according to their order of reaction. The order of a reaction is defined as the relationship between the concentration of individual species (reactant) and the rate of reaction. The investigation of rate order can be done experimentally by varying each reactant's concentration and measuring the rate of the reaction. If the reaction rate is independent of the concentration of a particular reactant, it is classified as zero order. This order is represent by a differential rate law (Equation 3.9). On the other hand, a first order reaction is one whose reaction rate is dependent on the concentration of a single reactant (Equation 3.10). Lastly, with a second order reaction the rate is proportional to the square of the concentration of a reactant (Equation 3.11).

$$r = k \tag{3.9}$$

where r = rate; k = rate constant.

$$r = k[A] \tag{3.10}$$

$$r = k[A]^2 \tag{3.11}$$

A special case of reaction order known as pseudo-order reaction is observed when the concentration of one or more reacting species remains constant [141]. The order of a typical pseudo reaction depends on the number of species whose concentration is changing during the reaction. Catalytic chemical reactions ideally fall into this category since their concentration do not

alter during reactions. Therefore, the order of reaction for the degradation of Rhod-B using catalytic films can be determined applying the pseudo reaction approach. With this approach, the TiO_2 photoactivated film surface is constant during the photocatalytic test and the concentration of Rhod-B changes with time. The first order pseudo rate differential equation can be written as Equation 3.12:

$$\frac{d}{dt}[Rhodamine\ B] = -k[Rhodamine\ B][TiO_2\ ] \tag{3.12}$$

where k = rate constant(s^{-1}) and t = time(s).

However, the rate constant k and TiO_2 term in the equation can be fused into a pseudo rate constant k`. Then Equation 3.12 becomes:

$$\frac{d}{dt}[Rhodamine\ B] = -k`\ [Rhodamine\ B] \tag{3.13}$$

where k`= pseudo rate constant = k [TiO_2] and t = time(s). An integral of Equation 3.13 results in Equation 3.14:

$$ln\frac{[Rhodamine\ B]}{[Rhodamine\ B]_0} = k`t \tag{3.14}$$

where k`= pseudo rate constant= k [TiO_2]; t = time(s) and subscript 0 represents Rhod-B concentration at time 0.

The integrated form of the rate order equation is helpful for the experimental verification of the order of the degradation of Rhod-B because concentration at time zero is easily measured as well as concentration at different periods. All these data are extracted by UV-vis spectroscopy. A plot of the change in concentration versus time should be a straight line whose slope is k`, the rate constant.

3.8 Summary

The raw material for the substrate was characterized and prepared for pressing of the first batch of substrates. The compacted substrates were

characterized before and after sintering. A compacting curve was constructed where the compacting pressure applied was plotted against average green density. The compacting pressure for the batch of substrates for the project was selected taking into consideration the properties measured before and after sintering. After the selection of the compacting pressure, the new set of substrates for the project were pressed and characterized.

The resin was prepared by the polymeric precursor method and was characterized. Five layers of the resin were deposited on rutile coated glasses by spin coating. The deposited films were calcined at 350 °C, 400 °C, 450 °C and 500 °C and were named G350, G400, G450 and G500. The as-prepared films were characterized. The resin was also deposited on rutile sintered substrates through spin coating technique to form ten layers. The substrates with the films were calcined at 350 °C, 400 °C, 450 °C and 500 °C and were named SAM 1, SAM 2, SAM 3 and SAM 4. The as-prepared films were characterized.

A mixture of the resin and rutile powder was calcined at 350 °C, 400 °C, 450 °C, 500 °C and 1000 °C and the powders were named P350, P400, P450, P500 and P1000.The powders were characterized by various techniques.

The photocatalytic performance of only the films on rutile sintered substrate was evaluated.

4 RESULTS AND DISCUSSION

4.1 Substrate raw material characterization

4.1.1 Phase analysis of the powder

X-ray diffraction technique was used to determine and identify the phase composition of the as-received rutile powder. Figure 4.1 shows the diffraction pattern of the powder.

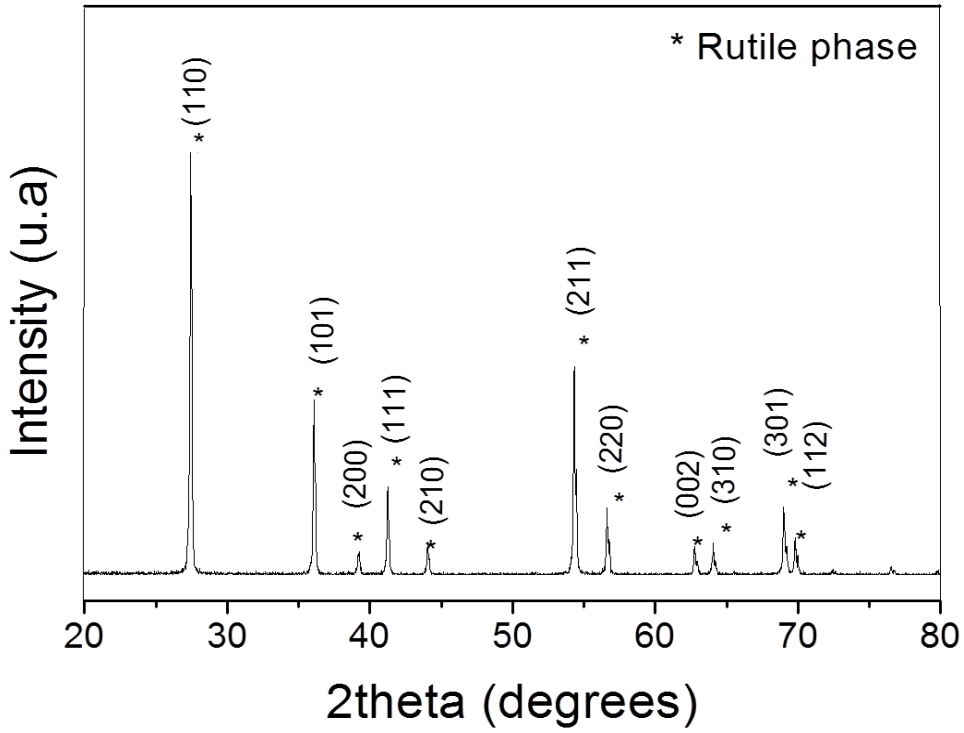

Figure 4.1 - Diffractogram of the as-received rutile commercial powder showing only the presence of rutile.

From Figure 4.1, diffractions from the identified family of lattice planes are at angles characteristic of rutile phase (# JCPDS 88-1175) [142].

Accordingly, the major phase in the powder is rutile as specified on the raw material. In general, the diffracted peaks tend to be sharp and narrow with an average crystallite size of 71 nm estimated by the Scherrer method. Thus, the powder is very crystalline.

Further, the (110) and (211) planes have higher intensities than the rest of the planes suggesting that the number of atoms in these planes is more compared to the other planes.

4.1.2 BET specific surface area

The specific surface area of the powder (pigment) was measured using the BET method and the BET particle size was calculated. The powder presented a surface area of 10 $m^2.g^{-1}$. A comparison of the specific area of the powder to other rutile pigments suggests that the specific surface area is quite high [143]. A particle size of 142 nm was estimated from the BET surface area and it is important to note that the degree of accuracy of the estimated particle size depends on the morphology, distribution and particle agglomeration. Specifically, the method is more accurate for agglomerate-free spherical particles with narrow particle size distribution [144]. The particle size and surface area of the powder are properties that can contribute to reactivity during sintering [82].

4.1.3 Powder morphology and particle size distribution

The particle properties of the powder were visualized by SEM, which permits the examination of the morphology of the particles, agglomeration state and direct estimation of particle size and distribution. Figure 4.2 contains a SEM micrograph of the powder and the estimated particle size distribution.

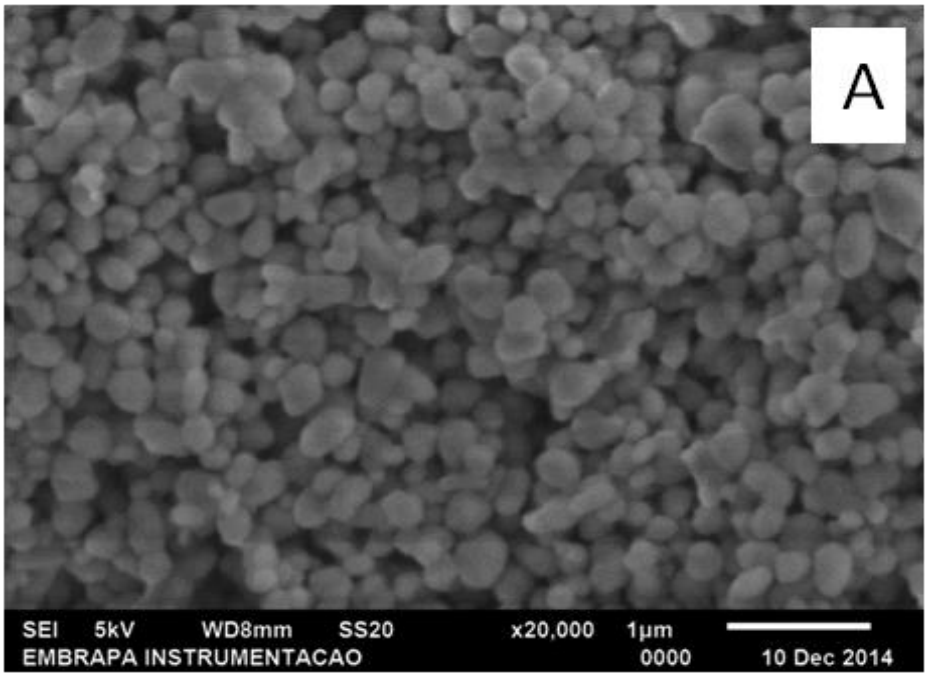

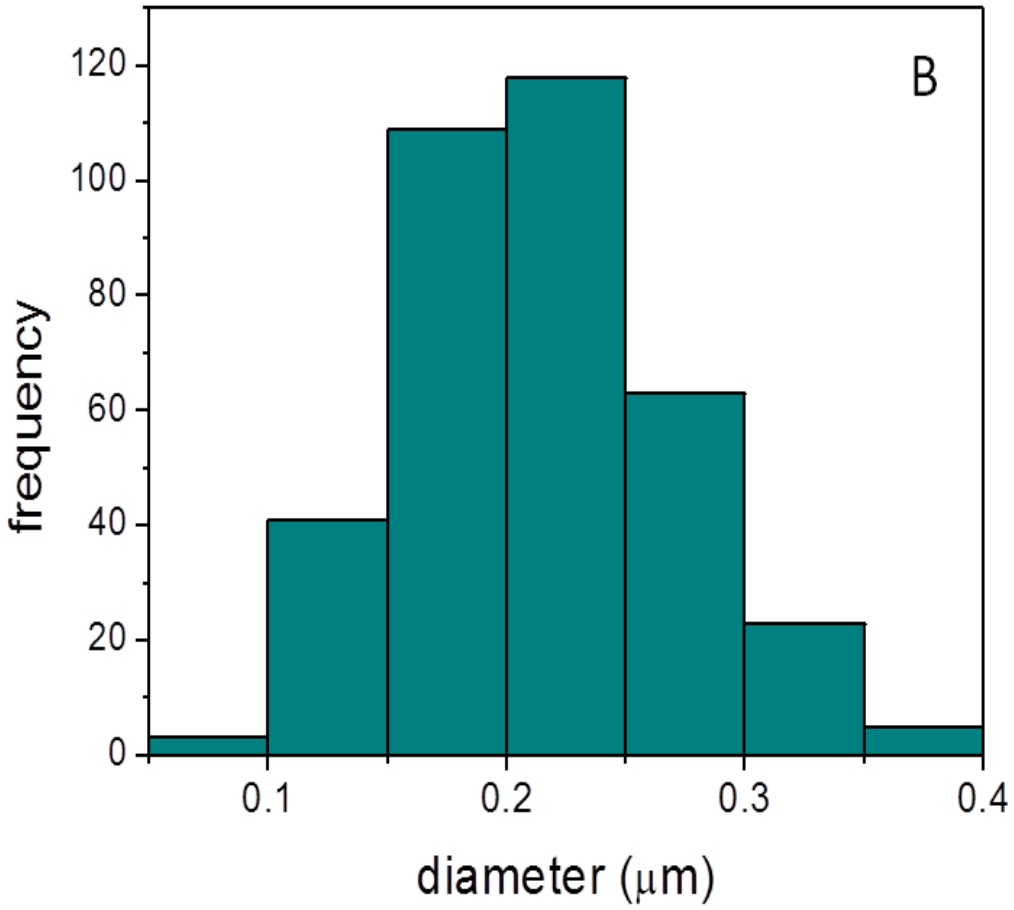

Figure 4.2 - SEM micrograph of the as-received rutile powder showing *A)* powder morphology and agglomeration and *B)* histogram indicating broad particle size distribution.

The powder is formed of spherical particles of different sizes as well as few agglomerates. To be more precise, the corresponding histogram shows the presence of particles smaller than 0.08 μm to agglomerates as large as 0.4 μm and the calculated average particle size is 0.219 ± 0.057 μm. The distribution and morphology of the particles can affect properties of the powder such as reactivity during sintering and packing density [81].

The particle size distribution of the powder was further analyzed by dynamic light scattering technique where a sample powder was dispersed in a solvent (water).

Figure 4.3 presents the particle size distribution of the dispersed powder according to fluctuations in the intensity of scattered light.

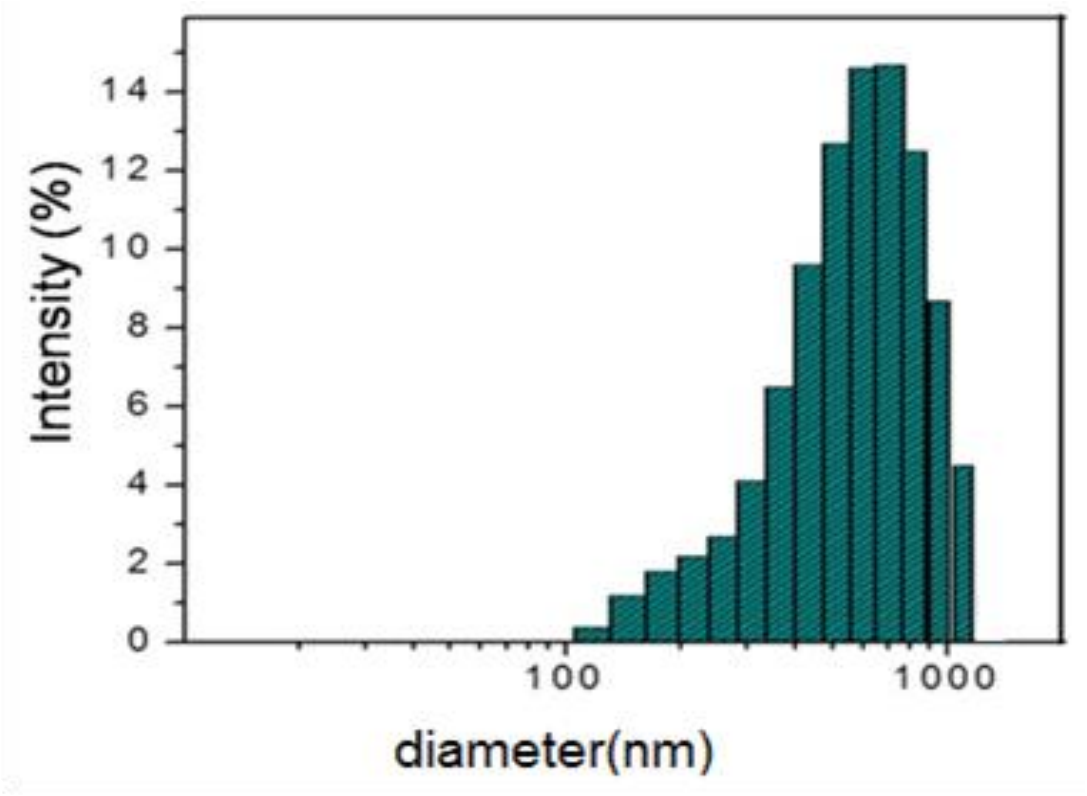

Figure 4.3 - Broad particle size distribution of rutile commercial powder by light scattering intensity.

In the dispersed form, the powder particles ranged from 164 nm to 1105 nm indicating a broad particle size distribution. A complementary result obtained from the DLS technique, polydispersity index of 0.6, also confirms high variability in particle size. Both results are in agreement with the SEM histogram (Figure 4.2B). However, the light scattering intensity average diameter (z average) of the particles was 632 nm, a higher average particle size than that estimated from the SEM images (219 nm). The discrepancy between the results could be due to the difference between the measuring techniques, being that DLS method measures hydrodynamic diameter instead of the real particle diameter [145].

Further, DLS method is very sensitive to particle agglomeration and it is possible that the agglomeration of fine dispersed particles resulted in larger measured particle diameters and consequently, a shift of the average particle size to higher values.

4.2 Substrate characterization

4.2.1 Compacting curve

To obtain the green compacts, different compacting pressures were applied. The relative densities of the green compacts were measured for each compacting pressure in order to construct a compaction curve (Figure 4.4).

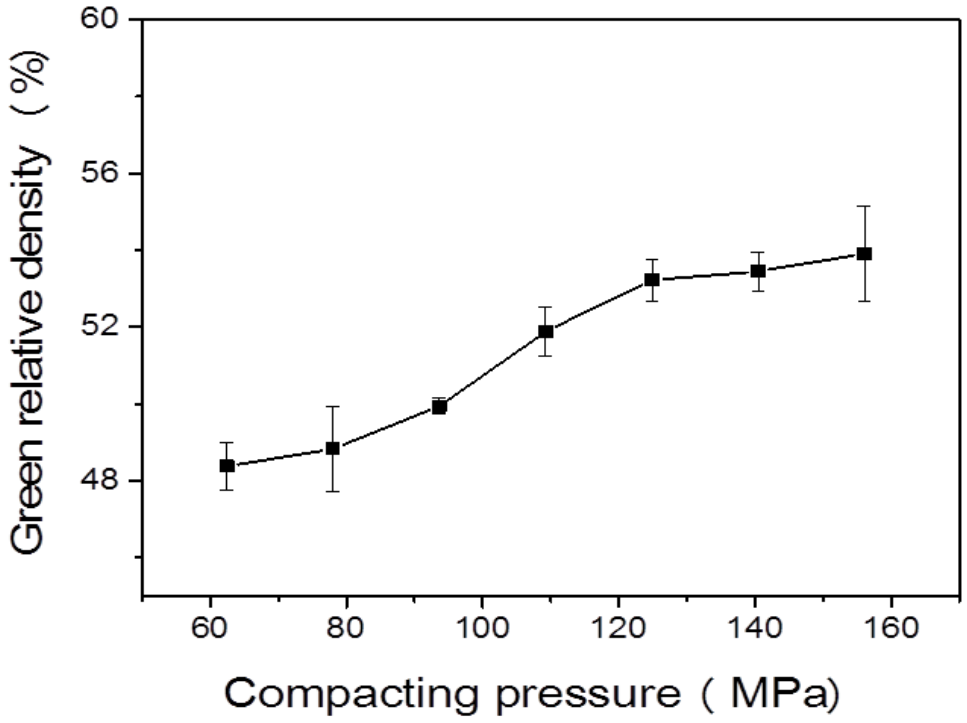

Figure 4.4 - The influence of compacting pressure on the variation of green relative density of the substrates.

The curve shows an increase in green density as pressure increases. With the increase of pressure from 62 MPa to 109 MPa, an increase of 4% in green density was observed. This could be a result of the breaking and rearrangement of the granules such that there is increase in particle-particle contact and consequently, reduction in pore volume [82]. On the contrary, for compacting pressures above 130 MPa, the density leveled off reaching a relative density of approximately 54% for the highest compacting pressure.

This behavior suggests that there exists an optimum pressure for which there is a balance between the breaking and rearrangement of granules as well as reduction of pore volume. After this pressure is exceeded, the established

particle-particle contact creates resistance to compaction in the form of frictional force. Usually, at this stage of powder compaction, the total frictional force tends to play a major role in the compaction of the particles than the applied pressure [146]. For this reason, compacting curves provide information on the maximum green density attainable using a particular pressing equipment or method, a useful tool for saving energy and improving density of sintered ceramics.

4.2.2 Physical properties of the substrates

The green compacts were sintered at 1450 °C/2h and their physical properties such as relative density, porosity, water absorption and shrinkage were measured. Figure 4.5 presents relative density prior to sintering (green) and after sintering of the substrates compacted at different pressures.

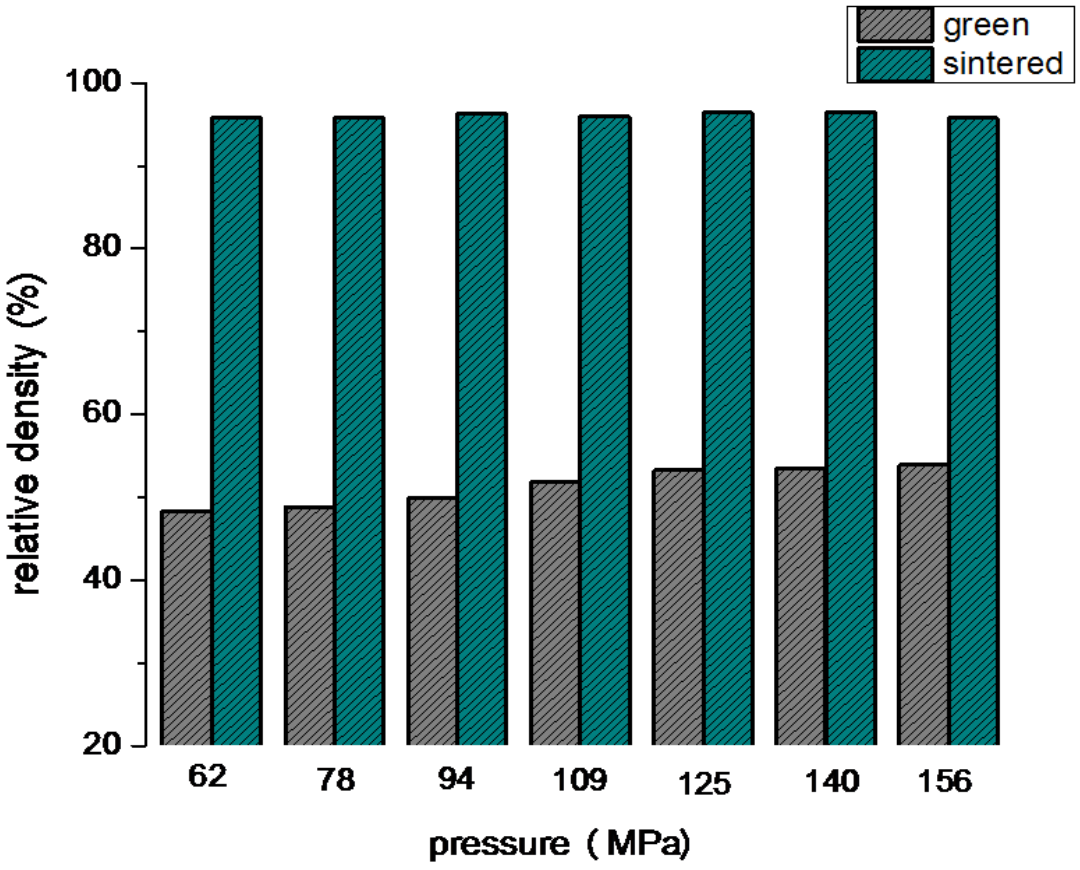

Figure 4.5 - The variation of green relative density and density after sintering of the substrates for different compacting pressures.

The effect of green compact density on relative density after sintering for the five compacting pressures appears to be negligible. Although, there were variations in green density, a relative density of approximately 96% was achieved for all samples after sintering. This outcome indicates that the reactivity of the starting powder, green density and sintering temperature contributed to the sintering process.

The results for porosity and water absorption also followed the same trend as relative density. Within the limitations of the characterization method used, 0% apparent porosity and water absorption were measured for all samples. Figure 4.6 shows the effect of green density on shrinkage of the substrates compacted at different pressures.

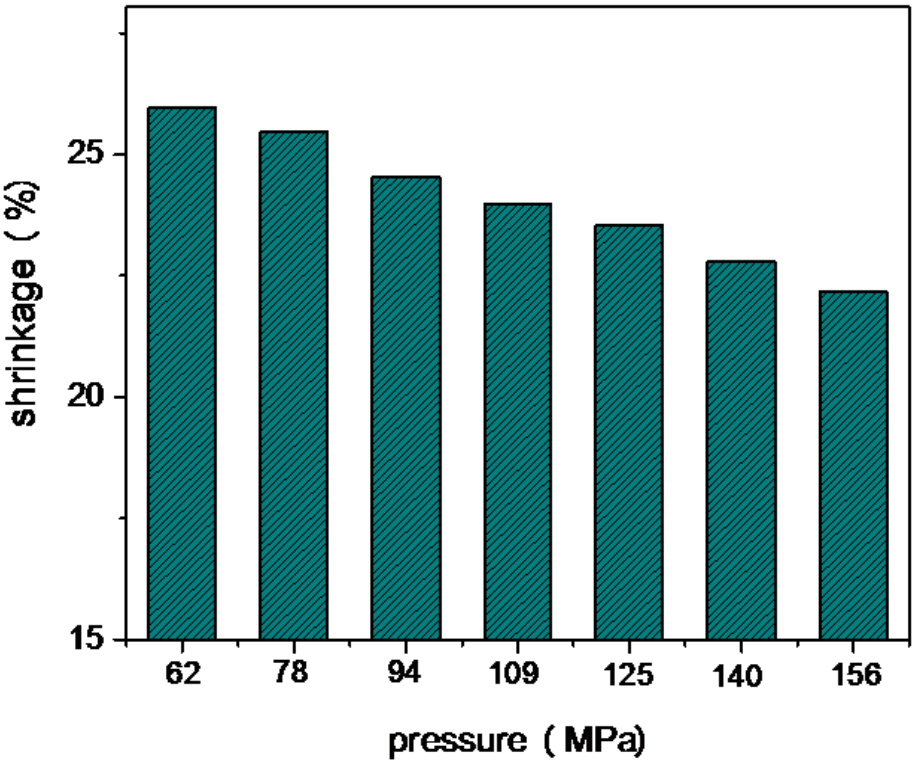

Figure 4.6 - Shrinkage after sintering of substrates compacted at different pressures.

Unlike the other properties (apparent porosity, water absorption and relative density), the percentage of shrinkage seems to be dependent on the compacting pressure and consequently on green density (Figure 4.5). In fact, an increase of compaction pressure from 62 MPa to 158 MPa produced a 4%

drop in shrinkage from 26 to 22%, which is significant depending on the dimensional tolerance of a project.

In general, green compacts undergo shrinkage during sintering especially due to densification, when the pores within the compact are eliminated, making room for intimate particle-particle contact [81]. Hence, the more pores to be eliminated in the case of less dense compacts (lower compaction pressure), the higher the linear shrinkage suffered. The loss of additives also accounts for shrinkage.

The physical properties (final density, water absorption, shrinkage, apparent porosity) and the compaction curve of the first batch of substrates were used as selection criteria for the final compaction pressure of the second batch of substrates.

The analysis of the results suggests that the final density is independent of green density and since minimal shrinkage differences are acceptable within the scope of the research, the compaction pressure was set at 109 MPa. Although, this pressure is not the highest, there is a balance between the final density and physical properties. The second batch of substrates (40 in number) was pressed at 109 MPa and their physical properties were measured before and after sintering.

A summary of the physical properties of the second batch of substrates that will be used for posterior analysis is presented in Table 4.1. The properties presented are identical to the first batch of substrates showing good reproducibility,

Table 4.1 - Physical properties of the second batch of substrates.

Sample	**Substrate**
Green Relative Density (%)	50.25 ± 0.12
Relative Density (%)	95.82 ± 0.10
Shrinkage (%)	24.39 ± 0.04
Water Absorption (%)	0.01 ± 0.05
Apparent Porosity (%)	0.01 ± 0.00

4.2.1 Microstructure of the substrates

A sample of the sintered substrates from the second batch of substrates was analyzed by X-ray diffraction for phase composition verification. The diffraction pattern of the TiO_2 substrate is showed in Figure 4.7.

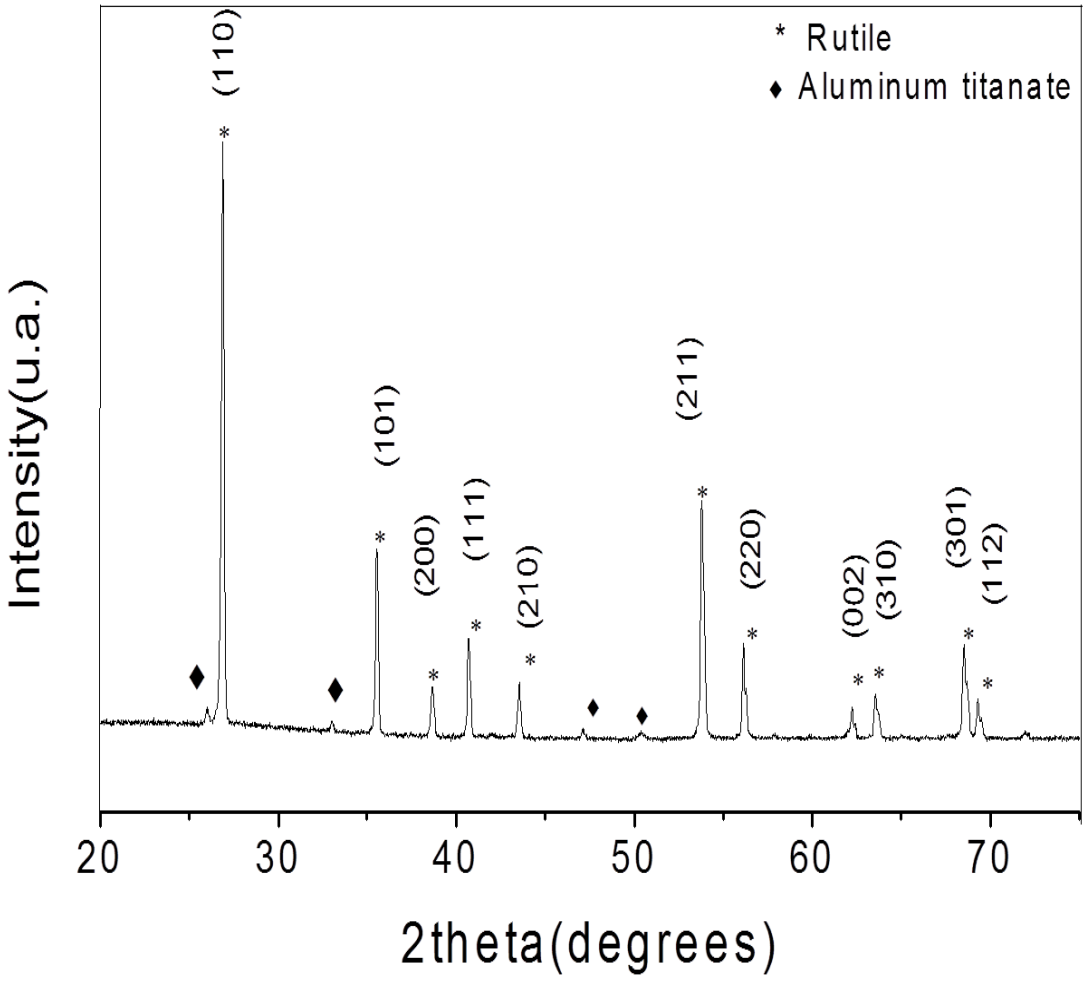

Figure 4.7 - X-ray diffraction pattern of the rutile TiO_2 sintered substrate.

The diffraction pattern (Figure 4.7) reveals rutile phase as predominant in the substrate, with reflections from identified planes corresponding to rutile phase. Furthermore, the intensity and width of the diffracted peaks suggest that the substrate is polycrystalline.

Basal reflections not pertaining to rutile phase identified with the symbol (◆) can be observed in the diffractogram. These reflections were not evident in the XRD analysis of the raw material (Figure 4.1), hence suggests that they

were formed during the sintering of the compacted powder at 1450 ºC. At this temperature, TiO_2 could react with other constituents of the powder, for example, Alumina, resulting in Al_2TiO_5 (Aluminum titanate). Sobhani et al. (2014) also reported the formation of Al_2TiO_5 through reaction sintering of alumina and titanium oxide powder at 1450 ºC [147]. Aluminum titanate has not been reported as photoactive therefore its influence on photocatalytic activity of the substrates can be considered negligible.

4.2.2 Microstructure of the substrates

The microstructure of the sintered substrate polished and a thermally etched at 1350 °C is shown in Figure 4.8. It contains a SEM micrograph of the substrate and grain size distribution.

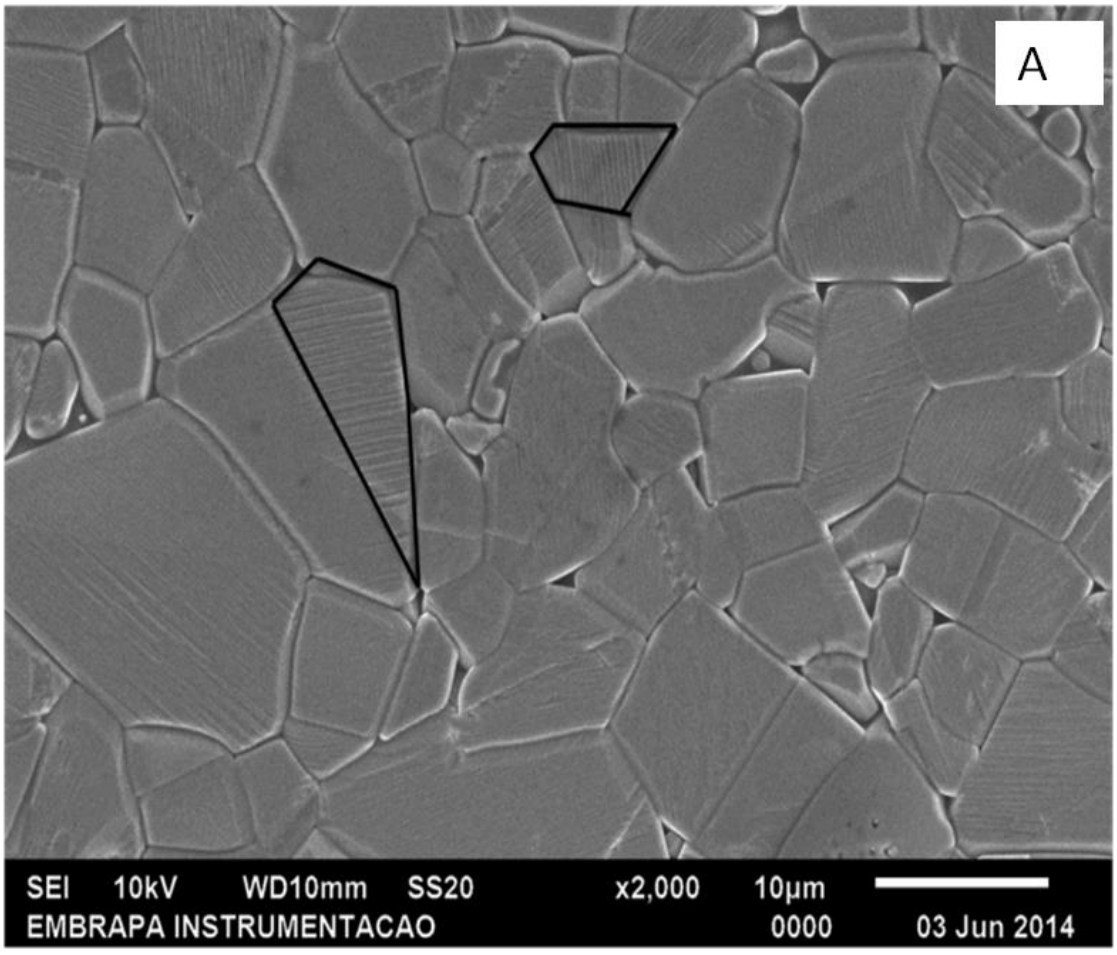

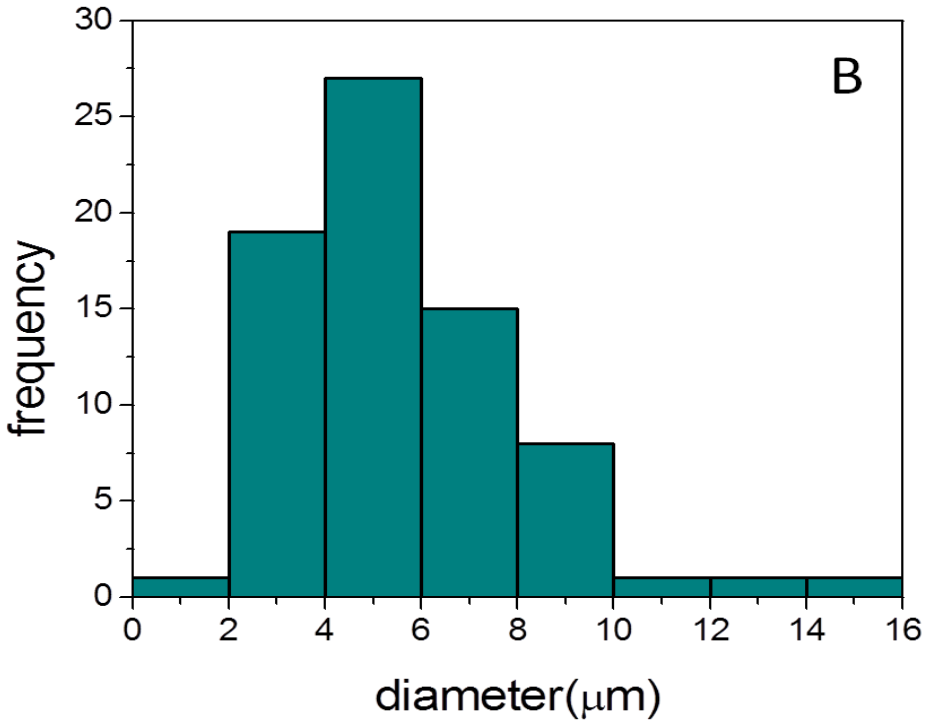

Figure 4.8 - *A)* SEM micrograph of the sintered substrate and *B)* distribution of grain size.

The microstructure of the substrate is composed of various grains of different sizes and shapes with well defined grain boundaries typical of sintered materials. The variation in grain size observed in the micrograph and the histogram could be linked to the particle size distribution of the starting powder (Figure 4.2 and 4.3), a possible factor for heterogeneous growth during sintering since larger particles grow at the expense of smaller particles. In fact, the mean grain size estimated was 5.71 ± 0.35 μm, which represents significant particle growth during sintering when compared to the mean starting particle size measured from the SEM micrograph (0.219 μm).

Despite the significant growth and high density (96%), visible pores between grains are present in the microstructure of the substrate. At first glance, these pores seem to contradict the validity of null porosity in the samples. However, null water absorption of the samples suggests that the pores are more likely to be closed than open. Another interesting feature observed in the micrograph (highlighted in Figure 4.8B) is localized lines on some grains that resemble slipping terraces or macro ledges. The source of the

lines could be related to deformation caused by the alumina polish used for sample preparation.More insight into the surface topology of the substrate is made possible by AFM analysis. Using the tapping mode, the surface of the unpolished substrate was analyzed and the 2D and 3D images are shown in Figure 4.9.

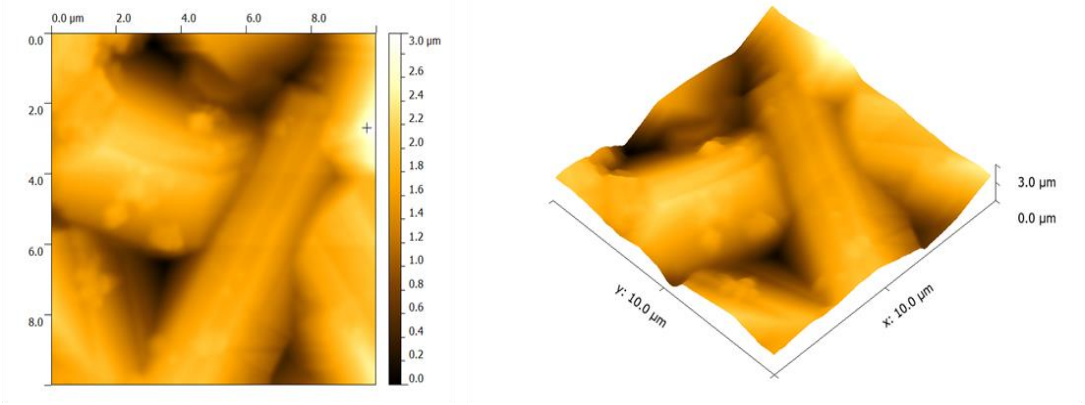

Figure 4.9 - AFM 2D micrograph of the sintered substrate and corresponding 3D image.

The AFM images show that the substrate is formed of grains of different sizes and the intersection of the grains are characterized by void or valleys. The surface features are in agreement with that of the SEM image (Figure 4.8). Apparently, the substrate is not planar and will affect the properties of the film such as adhesion and growth. The mean surface roughness was 0.478 µm.

4.3 Characterization of Ti^{4+} polymeric precursors resin

4.3.1 Resin viscosity and TiO_2 concentration

The Brookfield viscosity of the resin was 8.4 cP and it showed a newtonian behavior. This behavior is important since the resin will be spin coated onto the substrate and it is desirable that the resin's viscosity remains constant during the process. The concentration of Ti^{4+} ions in the resin was estimated using loss on ignition at 850 °C. From the TiO_2 residue produced, the concentration of Ti^{4+} ions in the resin was 0.050 $g.mL^{-1}$. The concentration can be used to estimate the quantity of TiO_2 that a volume of resin produces.

4.3.2 Phase analysis of the resin

Part of the Ti^{4+} precursor resin was separated and calcined in air with the following thermal conditions: 350 °C/12h, 400 °C/2h, 450 °C/2h and 500 °C/2h. These thermal conditions are the exact conditions for the preparation of the subsequent anatase films (SAM 1, SAM 2, SAM 3 and SAM 4 respectively). The phase composition of the prepared powders was verified by XRD to ensure phase purity of the posterior deposited films. Figure 4.10 presents the diffraction patterns of the as-prepared powders.

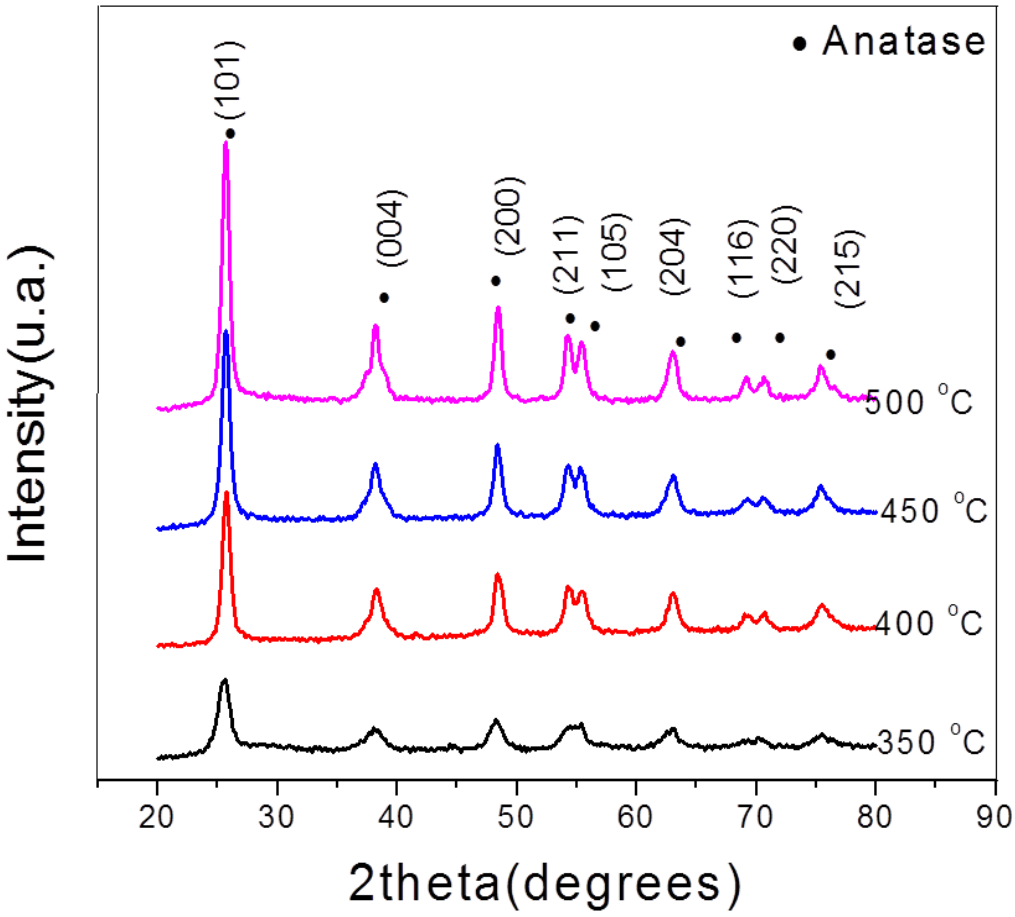

Figure 4.10 - X-ray diffraction pattern of the powders produced from the resin calcined at different temperatures.

The XRD patterns of the powders shown in Figure 4.10 depict the formation of anatase phase. The diffracted peaks are reflections from lattice planes peculiar to anatase phase with corresponding angles at 25.67°, 38.16°, 48.44°, 54.38°, 55.38°, 63.03°, 69.19°, 70.75° and 75.38° respectively [148].

The patterns are identical to other TiO_2 powders prepared by the polymeric precursors method [66,149]. Traces of rutile phase were not identified in the powder, dismissing any possibility of rutile contamination during resin synthesis.

For the samples calcined at lower temperatures (350 °C and 400 °C), the broad diffuse pattern of the peaks and the poor reflections from the (211), (105), (204), (116) and (220) planes, especially for 350 °C could be associated with the amorphous nature of the powder as well as crystallite size. It is expected that the thermal conditions at which the powders were calcined will be sufficient for the elimination of organic substances from the precursor resin and also for subsequent formation of anatase phase. However, the crystallinity of anatase phase and the amount of carbon eliminated are more pronounced at temperatures above 400 °C. As can be seen from the XRD patterns of 450 °C and 500° C, the peaks from all reflection planes of anatase are well defined with higher intensities compared to 350 °C and 400 °C. Table 4.2 presents the average crystallite size of the synthesized powders.

Table 4.2 - Crystallite size of the powders produced from the resin.

Sample	**Crystallite Size (nm)**
350 °C	8
400 °C	10
450 °C	10
500 °C	13

It can be inferred from the average crystallite size of the powders estimated by the Scherrer method that the crystallite size of the powders increased as calcination temperature increased. In general, the powders with smaller crystallites presented broader peaks possibly related to lesser planes for destructive interference [150]. The crystallite size of the powders indicates that the polymeric precursor method is a practical for obtaining nanometric powders.

4.4 Characterization of films on glass substrate

A replicate of the films on rutile substrate was made using a glass substrate. For this, five layers of rutile film were deposited on a glass substrate and were calcined. After, five layers of the precursor resin were deposited on the as-prepared rutile film and the assembly was then calcined.

4.4.1 Phase analysis

The phase of the films on glass was analyzed by XRD to observe the effect of the glass substrate on phase evolution. Figure 4.11 shows the XRD of the films and the rutile coated glass substrate.

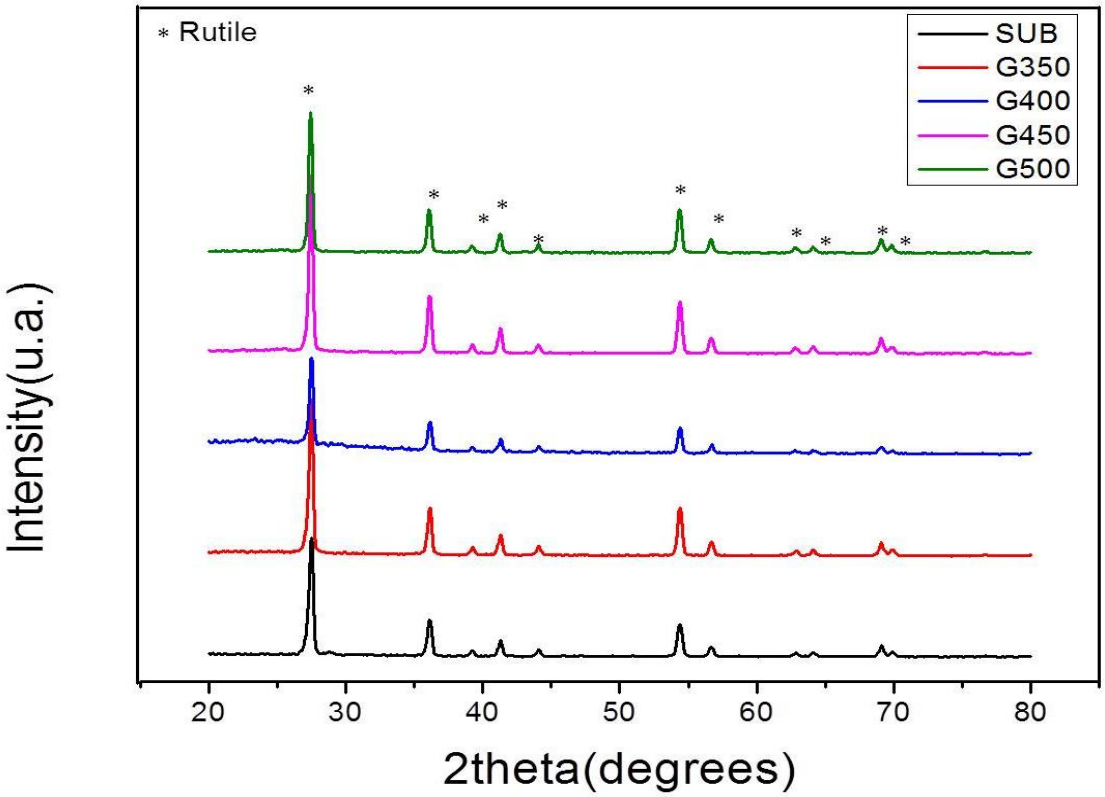

Figure 4.11 - X-ray diffraction pattern of rutile film on glass (SUB) and TiO_2 five layer films deposited on rutile coated glass by spin coating and calcined at a ramp rate of 1°C.min^{-1} to final calcination temperature and time: 350 °C/12h (SAM 1), 400 °C/2h (SAM 2), 450 °C/2h (SAM 3) and 500 °C/2h (SAM 4).

All the films presented diffraction peaks pertaining to rutile phase and no anatase diffraction peak was present. This could mean that either anatase

phase in the films was transformed prematurely into rutile phase or the films contain anatase phase but the layer is too thin to have significant signal for analysis in conventional X-ray diffraction equipment.

In order to further analyze the phase composition of the films, grazing incidence X-ray diffraction was performed on the samples. The runs were performed from 15° to 30° (2theta) where anatase principal (101) peak is known to be diffracted. Figure 4.12 shows the diffraction pattern of the films for the various temperature conditions.

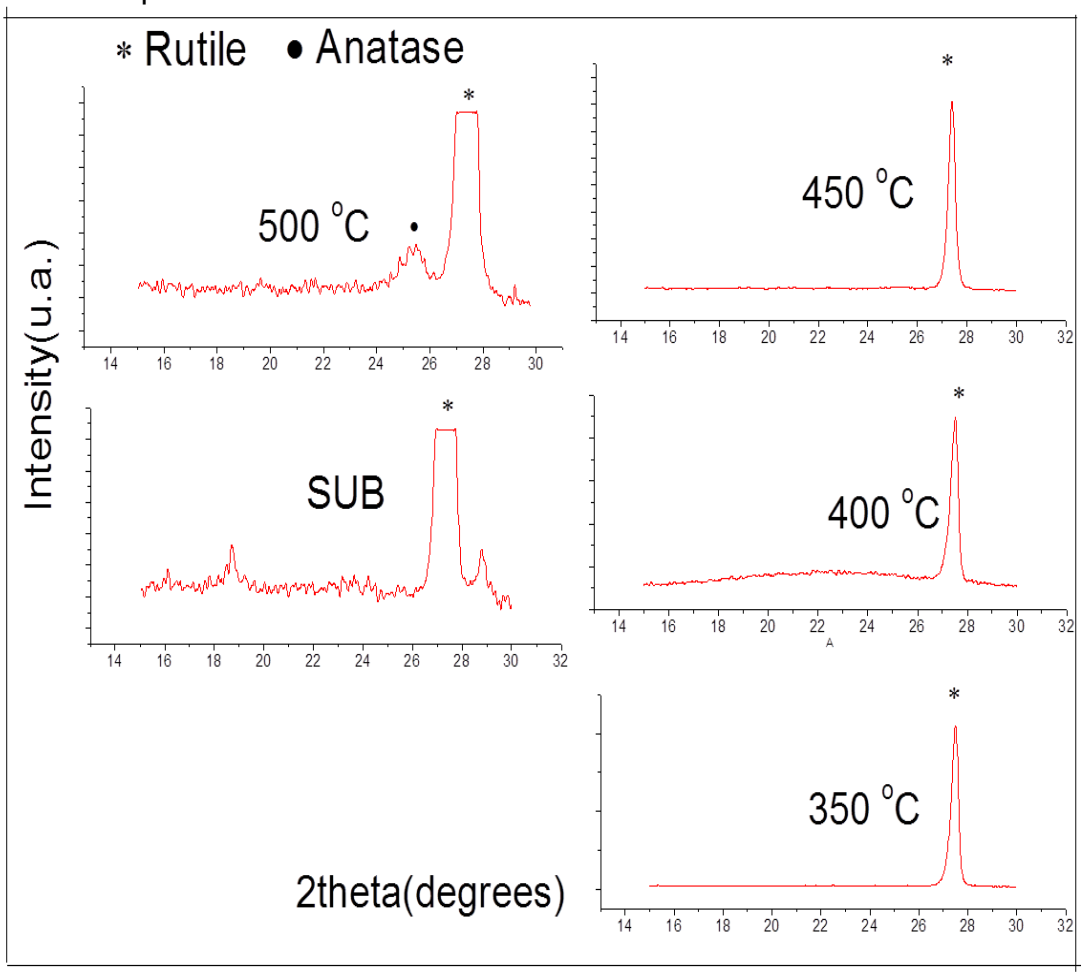

Figure 4.12 - Grazing incidence X-ray diffraction patterns of rutile film on glass (SUB) and TiO_2 five layer film deposited on glass by spin coating and calcined at a ramp rate of 1°C.min^{-1} to final temperature and time: 350 °C/12h (G350), 400 °C/2h (G400), 450 °C/2h (G450) and 500 °C/2h (G500).

The principal rutile peak at 27.3° (identified as ✶) is present in all the samples and is in agreement with the patterns obtained from conventional X-ray diffraction. Anatase phase diffracted at 25.5° was noted in the film calcined at

500°C (identified with (•)) and the estimated crystallite size from this peak is shown in Table 4.3.

Table 4.3 - Crystallite size estimated from grazing incidence X-ray diffraction pattern of TiO_2 five layer film deposited on glass and calcined at 1 °C.min^{-1} to 500 °C/2h (G500).

Sample	Crystallite Size (nm)
G500	9

The crystallite size indicates that anatase phase is still maintained in the film at this temperature but the percentage of the phase and possible transformation of part of it into rutile cannot be confirmed with much certainty because the rutile peak of the substrate can overlap the rutile peak from the transformation of anatase to rutile. The absence of anatase in the films (G350, G400 and G450) may be due to rutile since the crystallization of anatase demands higher temperatures contrary to anatase formed from the precursor resins or on pristine glass substrates.

4.4.2 Surface morphology and topology

Table 4.4 presents the mean square roughness of the films estimated from AFM images of the films deposited on the glass coated substrates.

Table 4.4 - Mean surface roughness of five layer TiO_2 films deposited on glass by spin coating and calcined at a ramp rate of 1 °C.min^{-1} to the final calcination temperature and dwell time: *A)* 350 °C/12h (G350); *B)* 400 °C/2h (G400); *C)* 450 °C/2h (G450) and *D)* 500 °C/2h (G500).

Sample	Mean Square Roughness (nm)
G350	117
G400	92
G450	121
G500	194

According to the data, calcination temperature did not have a clear effect on surface roughness. It is plausible to consider that there was no significant difference in surface roughness from one film to the other since surface roughness could be very sensitive to height variation when analyzing features of less than hundred nanometers to few hundreds of nanometers.

Figure 4.13 presents the AFM images of the as-prepared films.

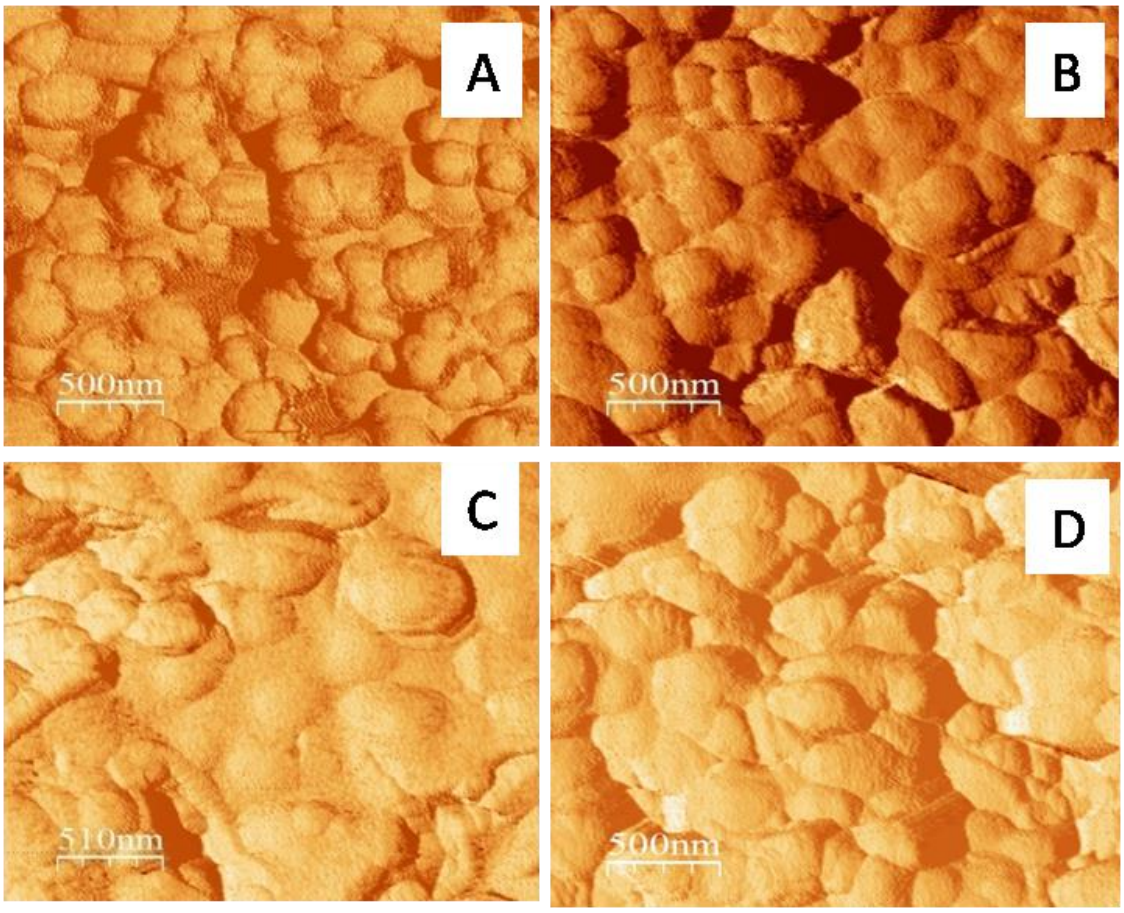

Figure 4.13 - AFM images of the five layer TiO_2 films deposited on glass by spin coating and calcined at a ramp rate of 1°C.min^{-1} to final temperature and time: *A)* 350 °C/12h (G350); *B)* 400 °C/2h (G400); *C)* 450 °C/2h (G450) and *D)* 500 °C/ 2h (G500).

The films appear to be formed on spherical particles (rutile film) whose morphology and size affect the structural properties of the film. The effect of temperature on microstructural evolution is also evident in the samples, for example, as calcination temperature increases, the film particles tend to increase in size.

4.4.3 Microstructural analysis

The morphology and homogeneity of the films deposited on glass were observed by SEM. Figure 4.14 shows the SEM micrograph of the films calcined at various temperatures (350, 400, 450 and 500 °C).

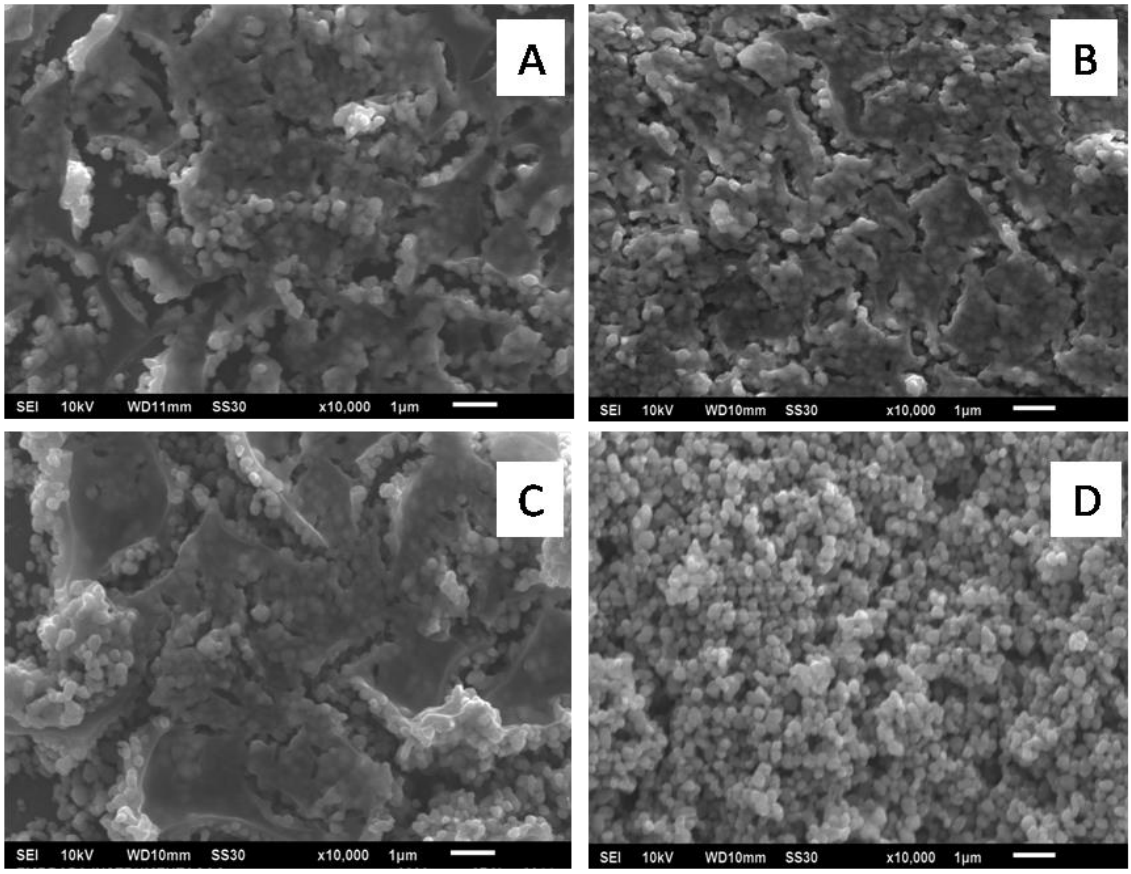

Figure 4.14 - SEM micrographs of five layer TiO_2 films deposited on rutile coated glass by spin coating and calcined at a ramp rate of 1°C.min^{-1} to the final calcination temperature and time: *A)* 350 °C/12h (G350); *B)* 400 °C/2h (G400); *C)* 450 °C/2h (G450) and *D)* 500 °C/2h (G500).

The micrographs show the evolution of the films with respect to temperature. During thermal treatment, the precursor resin losses solvent and organic content and gradually forms the TiO_2 film. Volume changes related to the process induces stress within the film which causes cracks. Films (G350, G 400 and G450) present cracks with discontinuous layers which appear to be residue from the Ti^{4+} polymeric resin. The nature of the layers suggests that the temperatures at which the films were calcined were not sufficient for the total

elimination of organic content except for G500 calcined at 500 °C. Hence for films produced by the polymeric precursors method, calcination temperature has to be adequate for elimination of organics and formation of a continuous film.

Figure 4.14C draws attention to the properties of the resin especially its viscosity. It is apparent that the loss of solvent and organic matter during heat treatment increases the viscosity of the precursor film so it is important that the initial viscosity is low coupled with an optimum calcination temperature for good film properties [151]. For the higher temperature calcined films, for example G500, the surface of the films does not have a viscous appearance perhaps due to the complete loss of organics.

4.5 Characterization of Ti^{4+} polymeric precursors resin

4.5.1 Phase composition

Figure 4.15 shows the XRD of the films deposited on rutile substrate.

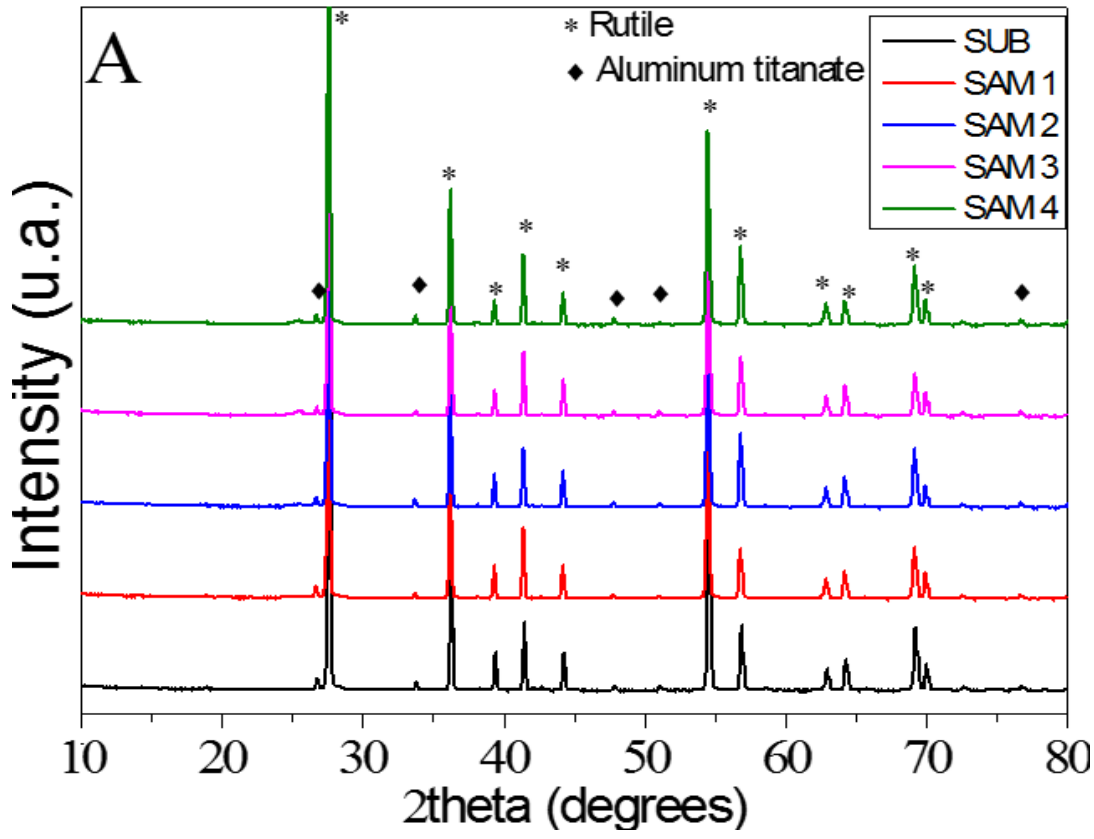

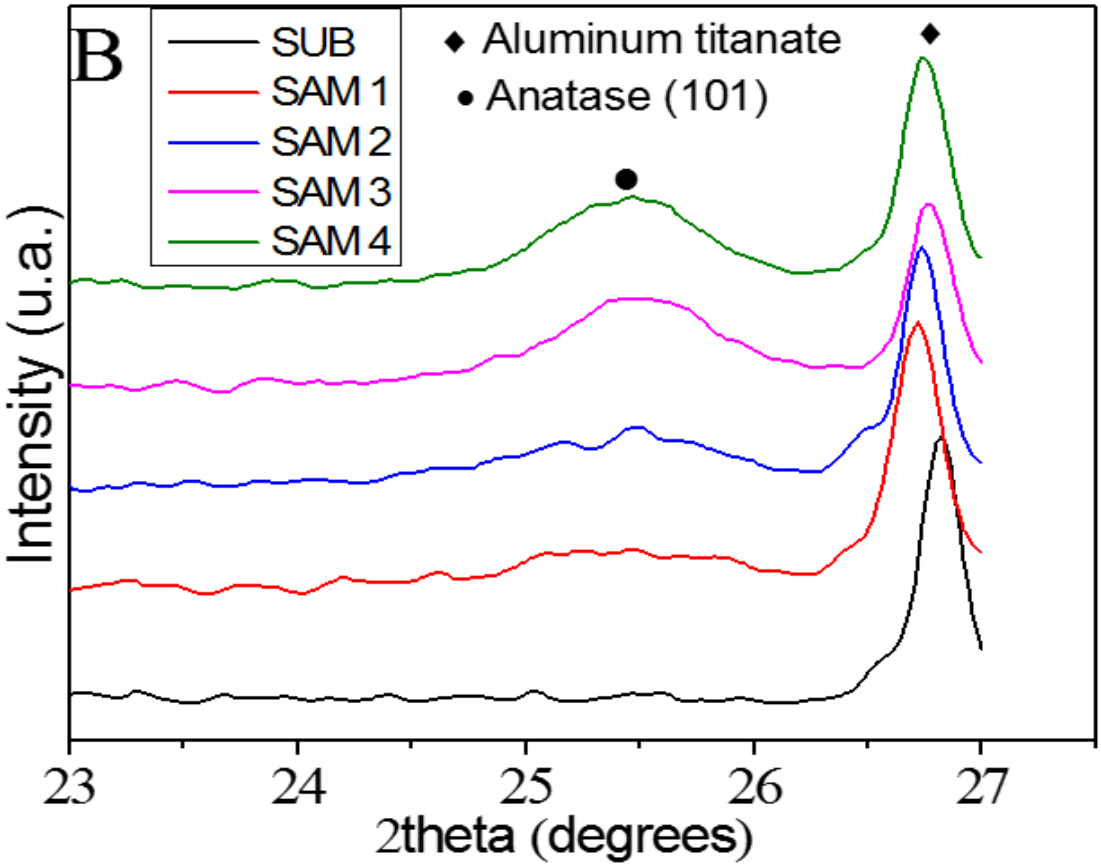

Figure 4.15 - X-ray diffraction patterns of ten layer TiO_2 films deposited on rutile sintered substrate calcined at a ramp rate of 1 °C.min^{-1} to the final calcination temperature and dwell time: *A)* rutile sintered substrate (SUB); 350 °C/12h (SAM 1); 400 °C/2h (SAM 2); 450 °C/2h (SAM 3) and 500 °C/2h (SAM 4) *B)* expanded view of selected region of the diffractogram.

The diffraction pattern of the substrate is identical to the samples with TiO_2 films (SAM 1, SAM 2, SAM 3 and SAM 4). The similarity in pattern could indicate that anatase has been transformed into rutile. However, this hypothesis is open to discussion since conventional XRD has its limitations [152]. Thus, signals from anatase in the film might be suppressed due to the volume of the substrate. So, a thorough analysis of the patterns was done by zooming into known regions of anatase reflections. Figure 4.15B shows anatase (101) plane in SAM 3 and SAM 4. A comparison among the samples indicates that anatase phase is gradually formed as calcination temperature increases. For SAM 1 and SAM 2, it can be deduced that at lower calcination temperatures, anatase

phase was not fully formed perhaps due to higher organic content. On the other hand, higher temperature calcined films, SAM 3 and SAM 4 show well defined anatase (101) peak. Table 4.5 presents the crystallite size of the samples with defined (101) anatase peaks.

Table 4.5 - Crystallite size estimated from the anatase (101) peak.

Sample	Crystallite Size (nm)
SAM 3	11
SAM 4	11

The crystallite size of SAM 3 and SAM 4, suggests that there is gradual crystallite growth due to constriction of the film by the substrate, a speculation derived from the crystallite sizes of the equivalent powders (Table 4.2).

Figure 4.16 presents the XRD patterns obtained from grazing incidence x-ray diffraction technique at angle of 2 °.

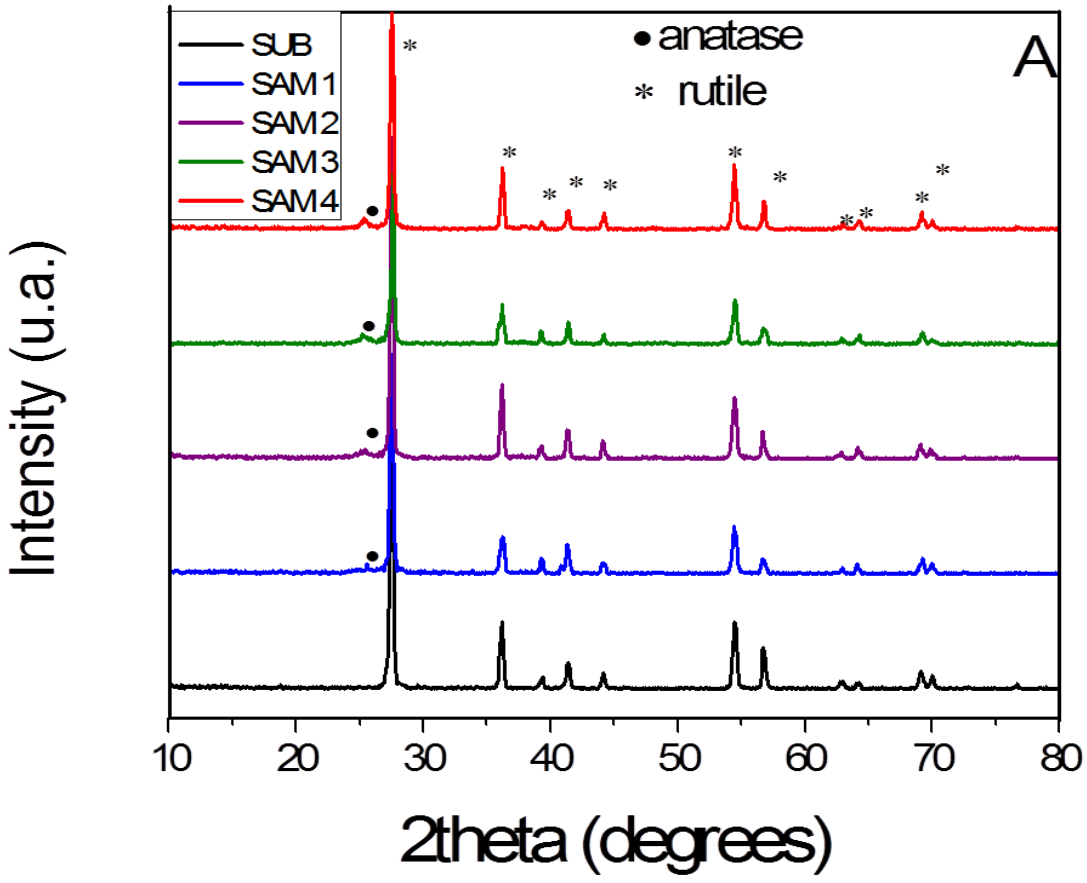

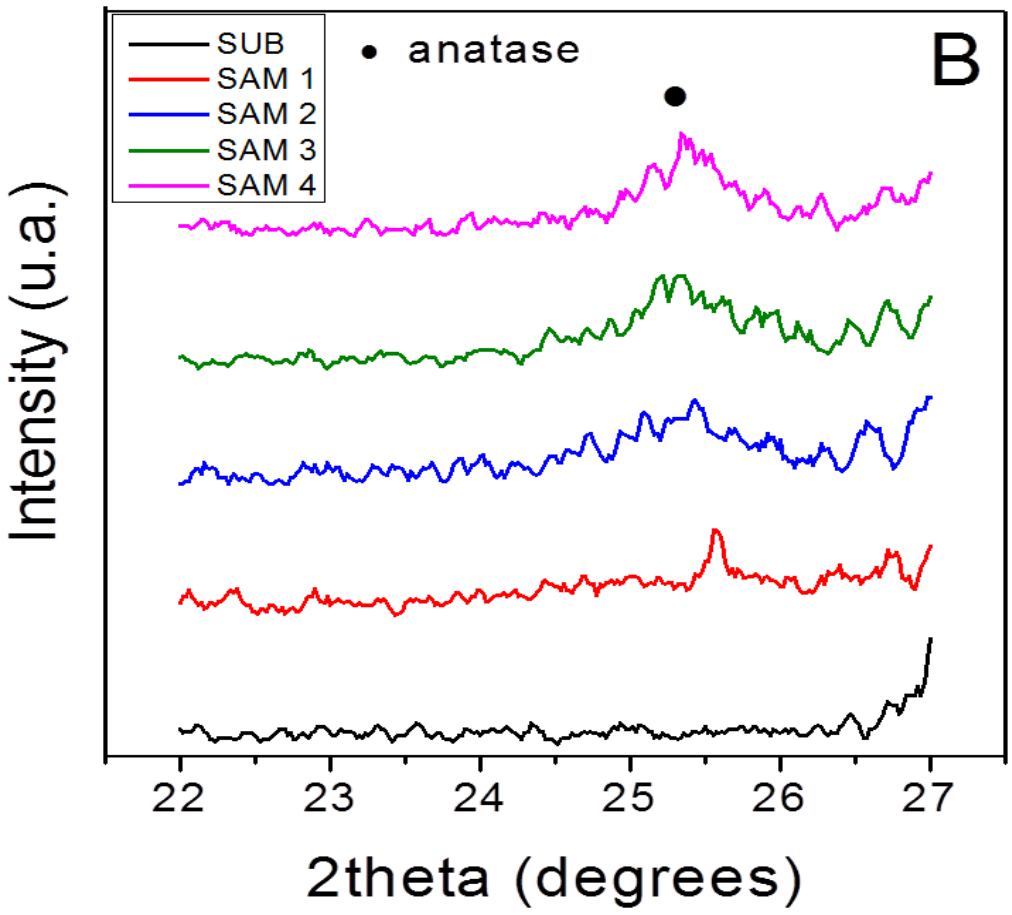

Figure 4.16 - Grazing incidence X-ray patterns of ten layer TiO_2 films deposited on rutile sintered substrate and calcined at a ramp rate of 1 °C.min^{-1} to final temperature and time: *A)* rutile sintered substrate (SUB); 350 °C/12h (SAM 1); 400 °C/2h (SAM 2); 450 °C/2h (SAM 3) and 500 °C/2h (SAM 4) *B)* expanded view of selected region of the diffractogram.

For all samples, reflections from rutile planes are present and their intensities and widths are almost identical. Unlike the patterns from conventional XRD, they show a complete absence of basal reflections associated with aluminum titanate as well as the unidentified basal reflection.

Since the basal reflections are absent, it can be assumed that the region analyzed pertains to the multilayered film. Even with this assumption, the region analyzed could be just above the substrate or distant from the substrate. If this is possible, then regions closer to the substrate would have stronger substrate signal than regions very distant from the substrate. The anatase (101) reflection

is identified in some of the films (•). Its intensity compared to that of the principal rutile peak suggests non-preferential growth of the anatase film or poor anatase phase formation. An amplified view of the region between angle 23° and 26° shows the effect of temperature on anatase formation and crystallinity. For example, higher temperature samples presented well defined anatase phase whereas for lower temperatures, anatase is weakly formed or not formed at all.

It is worth mentioning that anatase phase in the films on glass was identified in only one sample (G500) compared to three samples (SAM 2, SAM 3 and SAM 4) for films deposited on rutile substrate.

Rutile phase on the glass substrate and sintered rutile substrate may present different surface properties which could alter the formation of anatase in the films. For instance, the films formed on rutile phase observed by AFM (Figure 4.13) shows that they are formed on rutile particles while for rutile substrate; the films are formed on grains. Another reason could be the number of layers of TiO_2 films deposited on the substrates, five layers on the glass compared to ten layers on rutile substrate could affect the dynamics of anatase formation.

Table 4.6 presents the crystallite size of the samples estimated from the (101) anatase peak.

Table 4.6 - Crystallite size of the films.

Sample	**Crystallite Size (nm)**
SAM 2	11
SAM 3	15
SAM 4	17

It shows that the higher the temperature, the higher the tendency for crystallite growth and consequently, improved crystallinity of the film. Also, unlike the crystallite values presented by XRD, it seems the constriction of crystallite growth in the films is lower.

The difference in the values presented by both techniques may be due to the region analyzed, constriction is likely to be higher for film layers closer to the

substrate than those further away from the substrate surface or within the multilayered films.

The phase composition and structural properties of the substrate and films deposited on sintered rutile substrate were probed by micro-Raman spectroscopy (Figure 4.17).

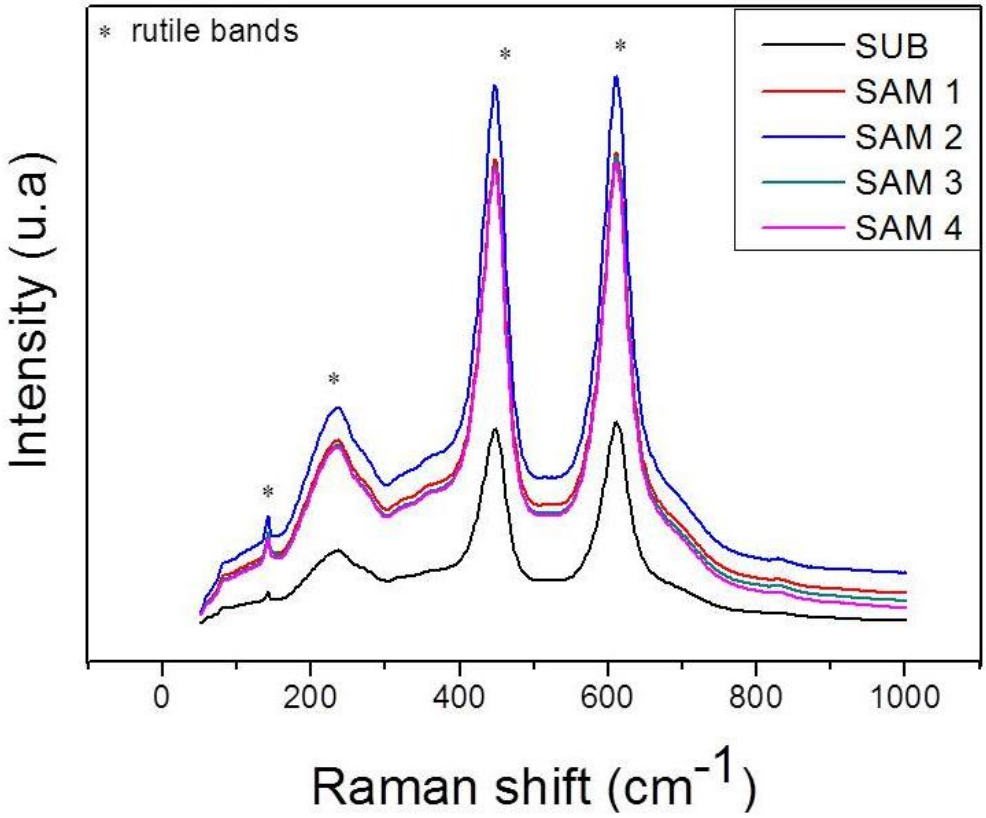

Figure 4.17 - Raman spectra of ten layer TiO_2 films deposited on rutile sintered substrate by spin coating and calcined at a ramp rate of 1 °C.min^{-1} to final calcination temperature and time: rutile substrate (SUB); 350 °C/12h (SAM 1); 400 °C/2h (SAM 2); 450 °C/2h (SAM 3) and 500 °C/2h (SAM 4).

Rutile phase presents four Raman active vibration modes: A_{1g}, B_{1g}, B_{2g} and E_g where A_{1g} is the Raman active mode for out of plane bending vibration, E_g is raman active in-plane stretching vibration and B_{1g} is out of plane stretching vibration and B_{2g} is symmetric stretching in plane [153]. The sintered substrate (SUB) presents Raman active modes at 142, 447, 612 cm^{-1} for B_{1g}, E_g and A_{1g} modes respectively. The bands confirm rutile phase as the major phase after sintering and is in agreement with other analysis found in the literature. Lattice

vibration of the substrate in the B_{1g} mode is very weak and almost absent while vibration in the B_{2g} mode is totally absent. A peak at 235 cm^{-1} can be observed. Although, this peak does not form part of Raman allowed bands for rutile, it has been reported in several Raman spectroscopy analysis. It is speculated that this peak is associated with second order scattering bands or peculiar rutile structure disorder scattering [153]. Apparently, the bands of all the films are identical with the substrate and no anatase active bands were exhibited. However, the films show broader peaks and higher intensities than the pristine substrate. In general, the intensities indicate the increase in active groups (Tii groups) due to the presence of the films.

The complete absence of anatase active modes despite confirmed by XRD suggests that there could be transformation of the films into rutile phase although the quantification of the phase present cannot be calculated from the spectra. It is important to note that micro-Raman results may depend on the region analyzed.

4.5.2 Surface topography

Figure 4.18 shows the AFM 2D and 3D images of SAM 1. As can be seen, the surface of the film is not planar due to the properties of the substrate as discussed previously.

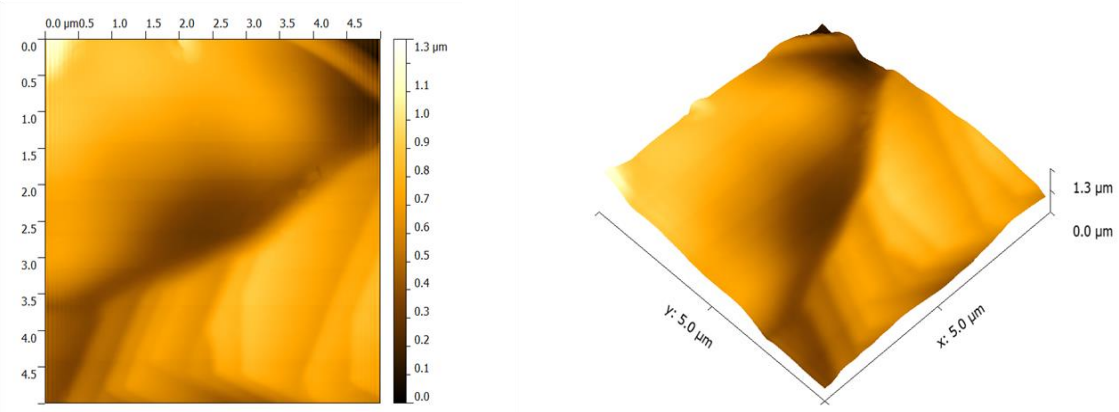

Figure 4.18 - AFM 2D and 3D images of SAM 1 - ten layer TiO_2 film deposited on rutile by spin coating and calcined at a ramp rate of 1°C.min^{-1} to 350 °C/12h.

As can be seen, the surface of the film is not planar due to the properties of the substrate as discussed previously. A feature that calls attention is the step-terrace structure at certain regions of the film.

The widths of the steps are as wide as 0.476 µm and as small as 0.694 µm. The structure bears some similarity to the localized lines observed in the SEM micrograph (Figure 4.8) even though the sample was not polished. Due to this, the localized lines and step terraces are intrinsic of the substrate and might be formed at high temperature. Czerwinski and Szpunar studied the topology of rutile oxide formed on Ti using AFM analysis and they reported the presence of macro and micro growth ledges at some regions of the oxide associated with diffusion of Ti cations suggesting that the lines observed on the substrate could be macro and micro growth ledges [154].

Figure 4.19 shows the AFM 2D and 3D images of SAM 2. They also show the influence of the substrate on the topography of the film. The variation in substrate height is shown clearly through the difference in color associated with height. The heterogeneous nature of the substrate might affect the growth of the film.

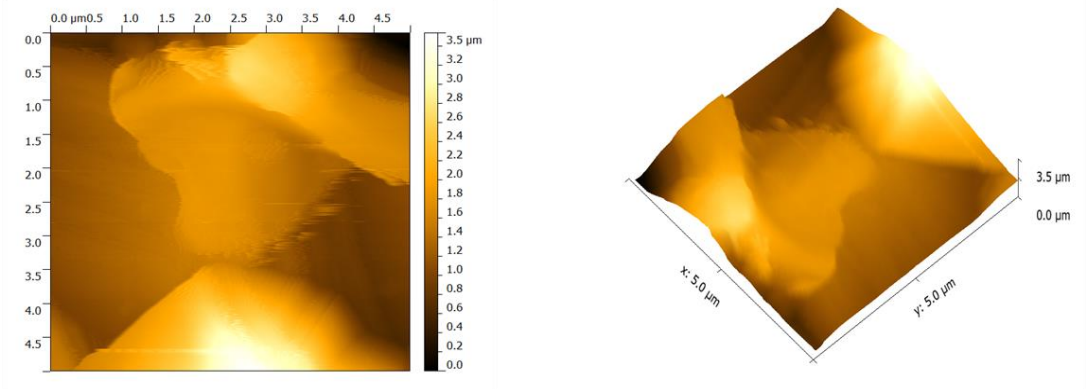

Figure 4.19 - AFM 2D and 3D images of SAM 2 - ten layer TiO_2 film deposited on rutile sintered substrate by spin coating and calcined at a ramp rate of 1°C.min^{-1} to 400 °C/2h.

Figure 4.20 shows the AFM 2D and 3D images of SAM 3. The surface of SAM 3 appears to be different from that of the films calcined at 350 and 400 °C (SAM 1 and SAM 2). It shows regions with what appear to be agglomerates of particles that may be associated to the growth of TiO_2 particles in the resin.

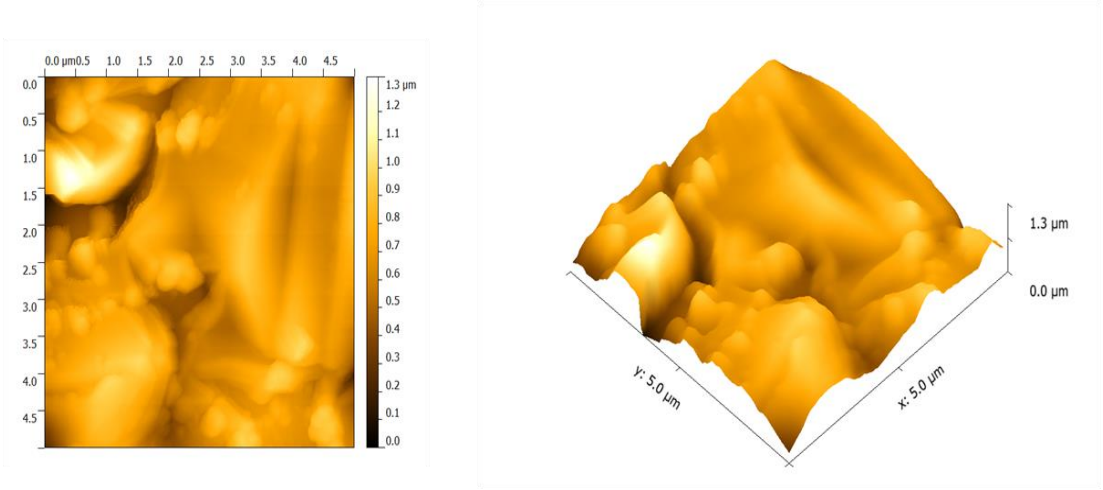

Figure 4.20 - AFM 2D and 3D images of SAM 3 -ten layer TiO_2 film deposited on rutile sintered substrate by spin coating and calcined at a ramp rate of 1°C.min^{-1} to 450 °C/2h.

Figure 4.21 presents the AFM image of SAM 4. The film shows topography associated with the substrate.

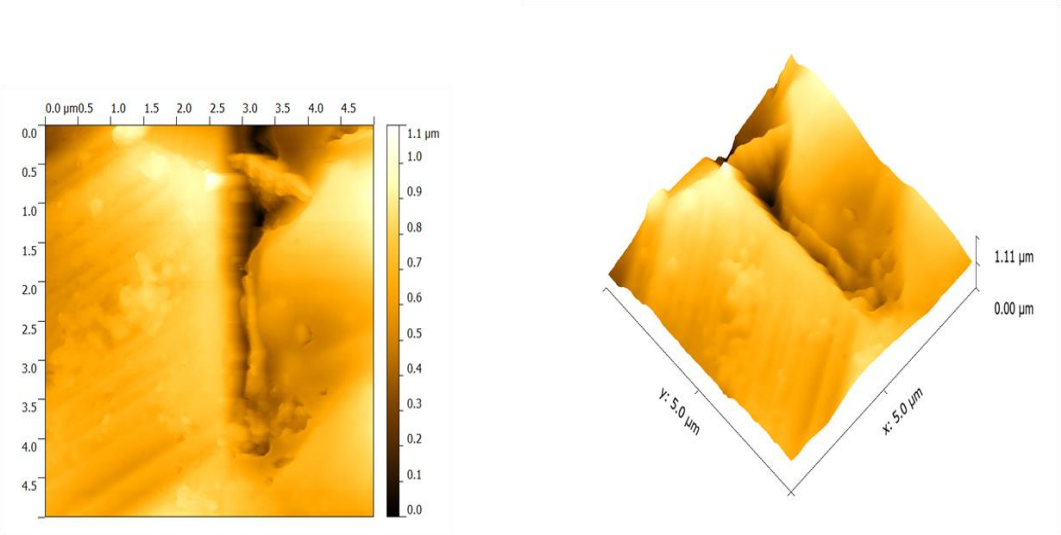

Figure 4.21 - AFM 2D and 3D images of SAM 4- ten layer TiO_2 film deposited on rutile sintered substrate by spin coating and calcined at a ramp rate of 1°C.min^{-1} to 500 °C/ 2h.

They suggest the growth of the resin particles with increase in temperature and crystallinity. Table 4.7 presents the mean square roughness of pristine rutile substrate and the 10 layer films deposited on rutile substrate.

Table 4.7- Mean square roughness of the films deposited on rutile substrate.

Sample	Mean Square Roughness (nm)
SUB	478
SAM 1	171
SAM 2	182
SAM 3	592
SAM 4	392

SAM 1 and SAM 2 have low surface roughness while the contrary is observed for SAM 3 and SAM 4. Since mean square roughness is related to variation in surface features, vast height variations at certain parts of the film shift the mean to higher values and so surface roughness might be different depending on the region analyzed. Temperature effect on surface roughness did not follow a clear trend.

4.5.3 Bandgap

The optical bandgap of the films was evaluated by diffuse reflectance measurements. The data were transformed into Kubelka Munk spectra which allowed bandgap extrapolation [155]. Figure 4.22 shows the normalized Kubelka Munk spectra for the samples and the linear extrapolation of the bandgap.

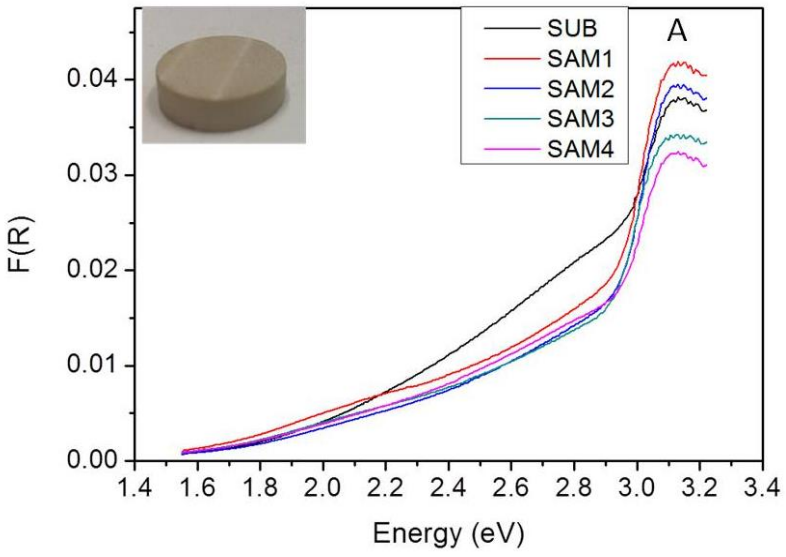

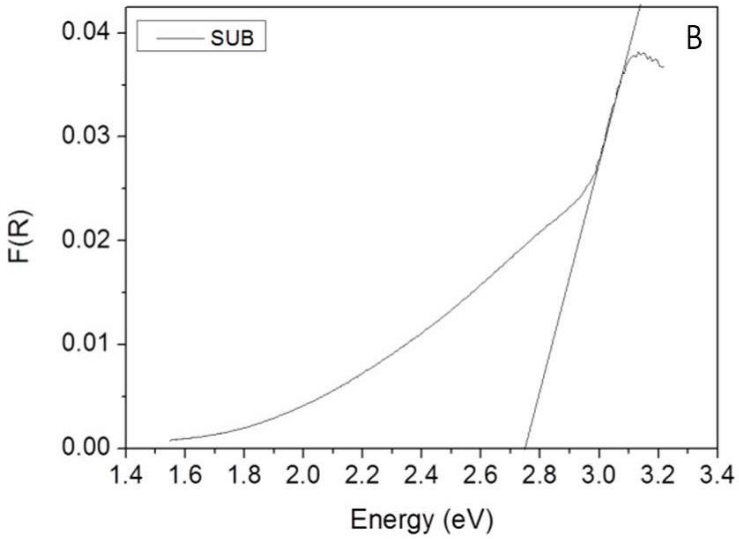

Figure 4.22 - *A*) Kubelka Munk spectra of the ten layer films deposited on rutile substrate and calcined at different temperatures at a rate of 1°C.min^{-1}: 350 °C/12h (SAM 1); 400 °C/2h (SAM 2); 450 °C/2h (SAM 3); 500 °C/2h (SAM 4) and *B*) the extrapolation of rutile bandgap using the substrate as an example.

The spectra of the substrate and the samples are almost identical. The spectra show an absorption shoulder indicated in Figure 4.22B a characteristic of anatase or rutile TiO_2 phase.

Table 4.8 presents the estimated bandgaps of the films and substrate.

Table 4.8 - Bandgap of rutile substrate and ten layer films deposited on rutile substrate.

Sample	Bandgap (eV)
SUB	2.74
SAM 1	2.83
SAM 2	2.85
SAM 3	2.84
SAM 4	2.79

The bandgap of the substrate is 2.74 eV compared to 3.0 eV in the literature [156]. The color and bulk nature of the substrate can contribute to its

lower bandgap. In general, there was bandgap lowering of the films compared to theoretical bandgap of anatase (3.2 eV).However, the bandgaps of the films are higher than the substrate which indicates bandgap modification with film deposition. A possible reason is the deposition of anatase phase a higher bandgap on a lower bandgap rutile substrate which may shift the bandgap of anatase to lower values in order to form a heterojunction. Also, structural modification due to phase transformation or disorder due to to crystallinity may cause bandgap opening as evident in SAM 1, SAM 2 and SAM 3 [157]. SAM 4 has the lowest bandgap and is closer to that of the substrate suggesting that as crystallinity increases, its bandgap tends to align with the substrate as a result of better interface formation.

4.5.4 Microstructure

Figure 4.23 shows the SEM micrographs of the films formed on rutile.

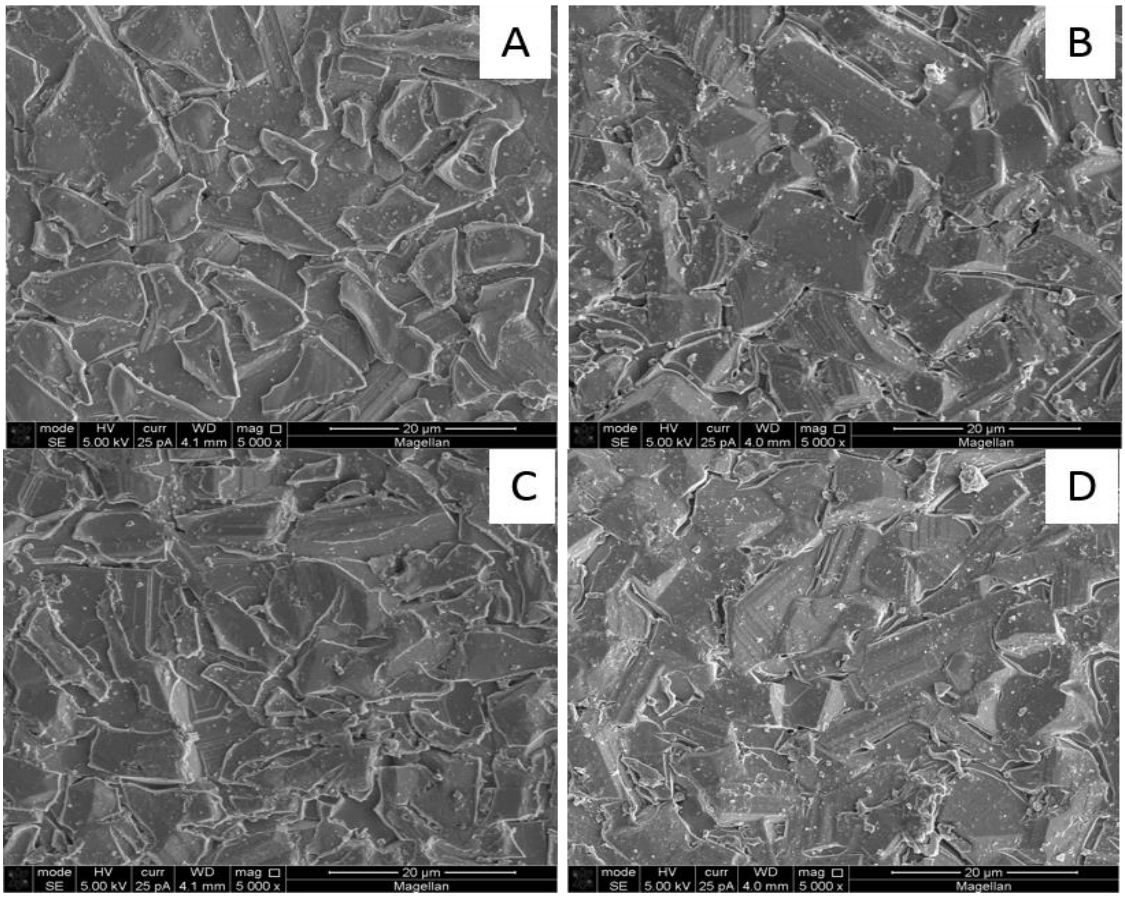

Figure 4.23 - SEM micrographs of ten layer TiO_2 films deposited on rutile by

spin coating and calcined at a ramp rate of 1°C.min^{-1} to final temperature and dwell time: *A)* 350 °C/12h (SAM 1); *B)* 400 °C/2h (SAM 2); *C)* 450 °C/2h (SAM 3) and *D)* 500 °C/2h (SAM 4).

The presence of the films on the substrates is evident for all the samples. As can be seen, SAM 2 and SAM 4 presented a more homogeneous and continuous film despite the presence of cracks. On the contrary, micrographs of SAM 1 and SAM 3 show dispersed islands of TiO_2 film as well as exposed regions of the substrate.

The total absence of TiO_2 film on the exposed substrate cannot be confirmed because there can be nanometric films in these areas that were not revealed due to the resolution limitation of scanning electron microscope The microstructure evident in the samples can be associated with the process by which films are formed in the polymeric precursor method. One of the crucial stages is the elimination of organic materials and solvent evaporation which cause minimal to severe contraction depending on the viscosity of the resin, calcination temperature and time [151]. Contraction induces stress in films causing cracks.

The trend for crack formation was not consistent for the samples, for example SAM 2, a lower temperature calcined film compared to SAM 3, presented a more homogeneous film with less cracks. It therefore draws attention to the substrate properties as a possible contributing factor to the quality of the films.

It is likely that the films, SAM 2 and SAM 4, were formed on a more planar region of the substrate, reducing stress associated with the difference in film height. Another possible cause of the cracks may be due to stress associated with lattice mismatch between the substrate and the film.

Figure 4.24 shows a closer view of the SEM micrographs. In these micrographs, the exposed surface of the substrate and the films in SAM 1 and SAM 3 depicts that the films are at different heights which could be an evidence for their detachment during calcination. Dispersed particles on the films, which appear to be anatase particles, can be seen on all samples. Figure 4.24D

shows a highlighted region with detached film. The depth of the region suggests that the films are thick in nature.

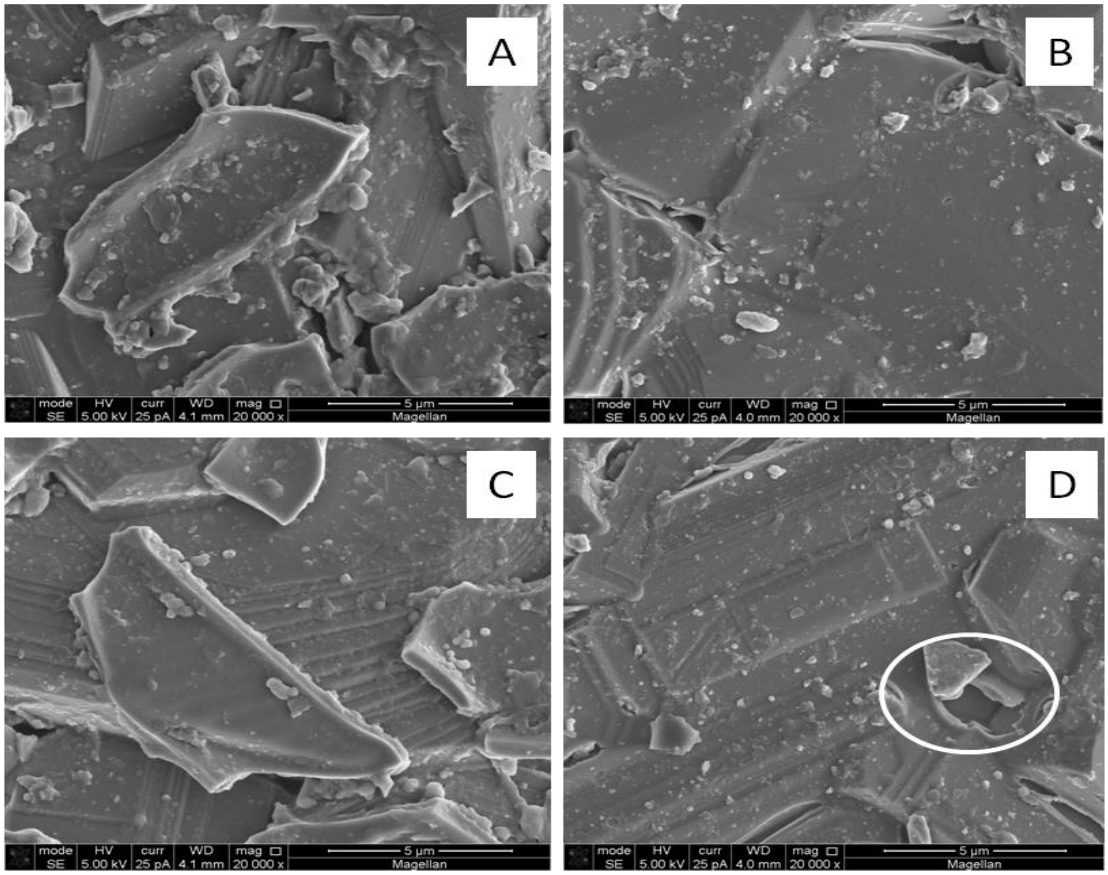

Figure 4.24 - SEM micrographs of ten layer TiO_2 films deposited on rutile substrate and calcined at a rate of 1°C.min^{-1} to final temperature and dwell time: *A)* 350 °C/12h (SAM 1); *B)* 400 °C/2h (SAM 2); *C)* 450 °C/2h (SAM 3) and *D)* 500 °C/2h (SAM 4).

4.5.5 Film thickness

The thickness of selected films (SAM 1 and SAM 2) were analyzed by SEM. Figure 4.25 shows the cross sectional SEM of SAM 2 and a line energy EDX scan of the analyzed region. The film width estimated from the micrograph is approximately 1.4 µm from the surface of the substrate (Figure 4.25 A). However, the analysis of the patterns of the individual elements, especially Ti, suggests that the film could be 1.2 µm from the substrate (Figure 4.25 B). If

zero is considered as the apex of the film, the intensity of Ti increased until it became stable at 1.2 µm, indicating the onset of the surface of the substrate.

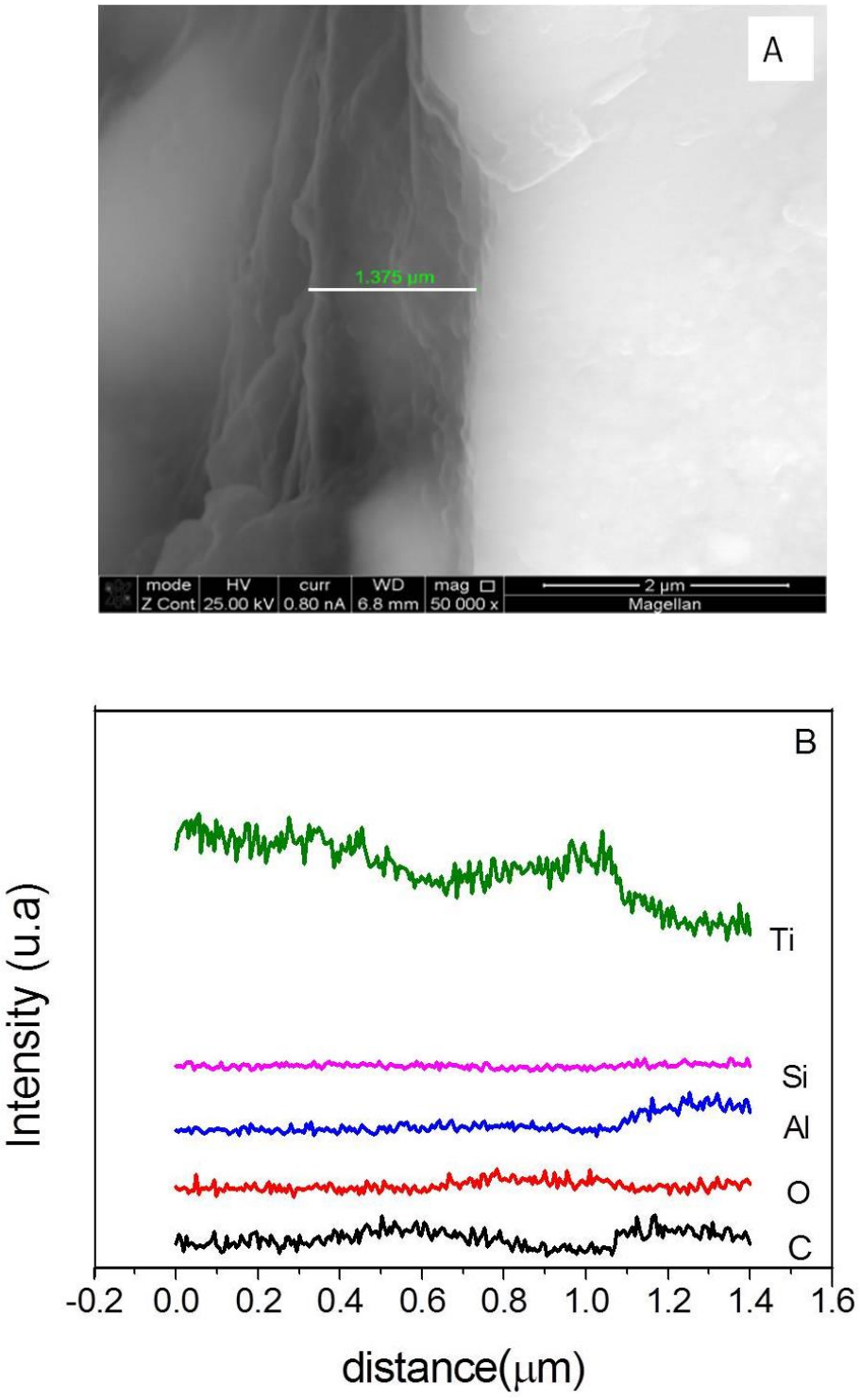

Figure 4.25 - *A)* Micrograph of cross sectional SEM of SAM 2 - ten layer TiO_2 films deposited on rutile substrate by spin coating and calcined at 400 °C/2h with a rate of 1 °C.min^{-1} and *B)* EDX line scan of the measured region.

The cross sectional FEG of SAM 1 micrograph is presented in Figure 4.26.

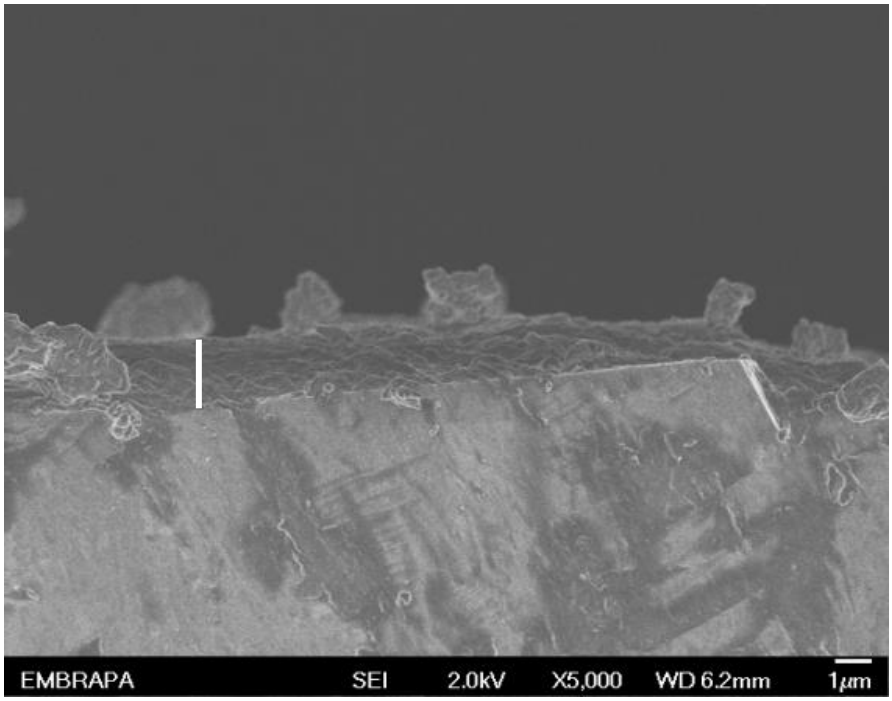

Figure 4.26 - Cross sectional FEG micrograph of SAM 1-ten layer TiO_2 film deposited on rutile substrate and calcined at 350 °C/12h with a rate of 1°C.min^{-1}

The micrograph clearly shows anatase film on the substrate with a width of 1.4 µm identified by white line, however this value is debatable because areas to the right of the identified region have widths up to 1 µm.

The surface of the film is not uniform and depending on the region of the fracture, variation in measured film width can be observed. As such, comparing the width values of the two different, it can be assumed that the samples have a width range between 1 µm to 1.4 µm.

4.6 Characterization of mixed phase powders

4.6.1 Phase composition

Micro-Raman spectroscopy was utilized to study the phase composition of the powders. Figure 4.27 presents the patterns of the mixed phase powders and rutile powder.

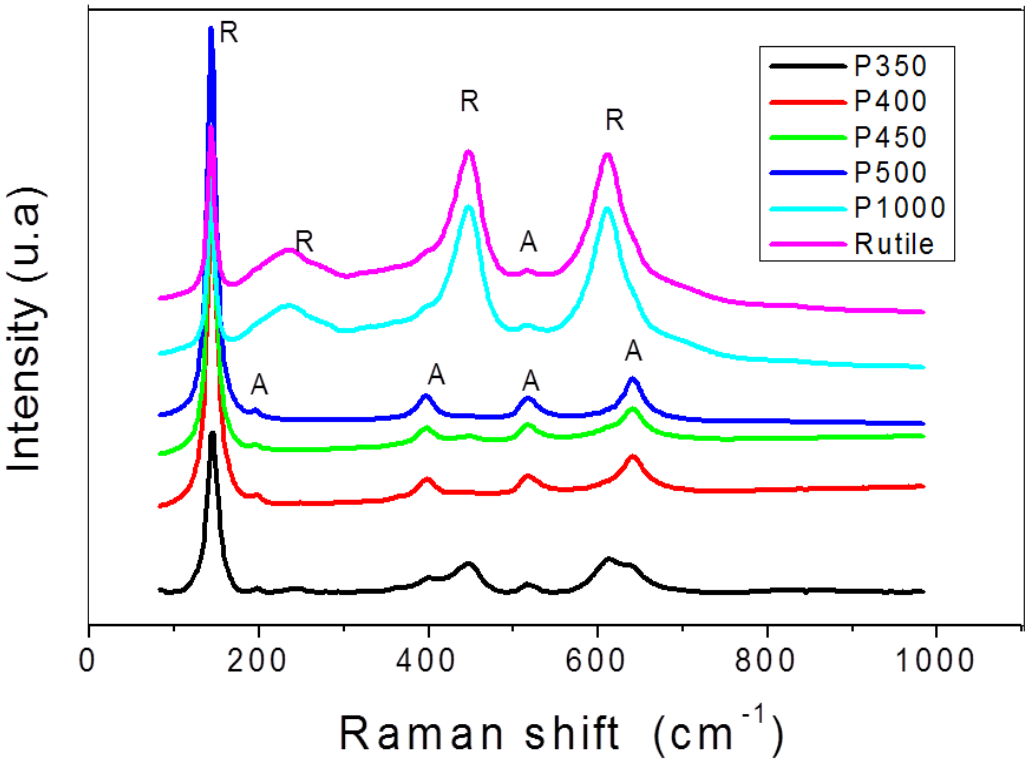

Figure 4.27 - Raman spectra of powders produced from a mixture of rutile powder and Ti^{4+} resin and calcined at various temperatures: P350 (350°C /12h), P400 (400°C /2h), P450 (450 °C/2h), P500 (500 °C/2h) and P1000(1000°C /2h).

The phase composition and structural properties of the powders were probed by micro-Raman spectroscopy. The rutile raw material and the powder calcined at 1000 °C present rutile active modes at 143, 446 and 612 cm^{-1} for, B_{1g}, E_g and A_{1g} and respectively. The bands indicate rutile phase as the major phase of P1000 and the rutile raw material. Usually, rutile presents a low intensity band at 143 cm^{-1} compared to the other characteristic bands of rutile, and also anatase phase presents a much intense band at 144 cm^{-1}. Due to the proximities of the band values there could be overlapping of the bands, however the band at 143 cm^{-1} is assumed to be rutile. Another peak is also observed at 235 cm^{-1} which does not form part of Raman allowed bands, it has been reported in several Raman spectroscopy analysis of rutile phase components. It is speculated that this vibration mode is caused by second order scattering bands or peculiar rutile structure disorder scattering. Apart from the peak at 235 cm^{-1}, a peak at 515 cm^{-1} is also observed. Usually peaks in the vicinity of

515 cm^{-1} are related to anatase phase and is rather surprising that the spectra of rutile and P1000 contain such a band. It is interesting to note that the band was absent in the sintered substrate. Then, it is highly improbable that anatase phase is retained at 1000 °C being that the temperature is sufficiently high. However, the raw material rutile contains this band which could indicate that the powder may contain anatase impurities that were not detected by XRD. It calls attention to the fact that alumina and silica could retain anatase phase if there are anatase impurities.

As expected, the mixed phase powders present anatase and rutile active modes. Four of the six active bands of anatase were present in P350, P400 P450 and P500: 196 cm^{-1} (E_{2g}), 396 cm^{-1} (A_{2g}), 517 cm^{-1} (A_{1g}), 642 cm^{-1} (E_{3g}). Also, a rutile band at 143 cm^{-1} was identified. The number of bands present for each phase shows that there was an intimate mixture of the phases in the powder. For P350, the bands suggest that anatase is formed at 350 °C and could be superimposed on rutile.

4.6.2 Microstructure

Figure 4.28 shows the SEM micrographs of P450 calcined at 450 °C.

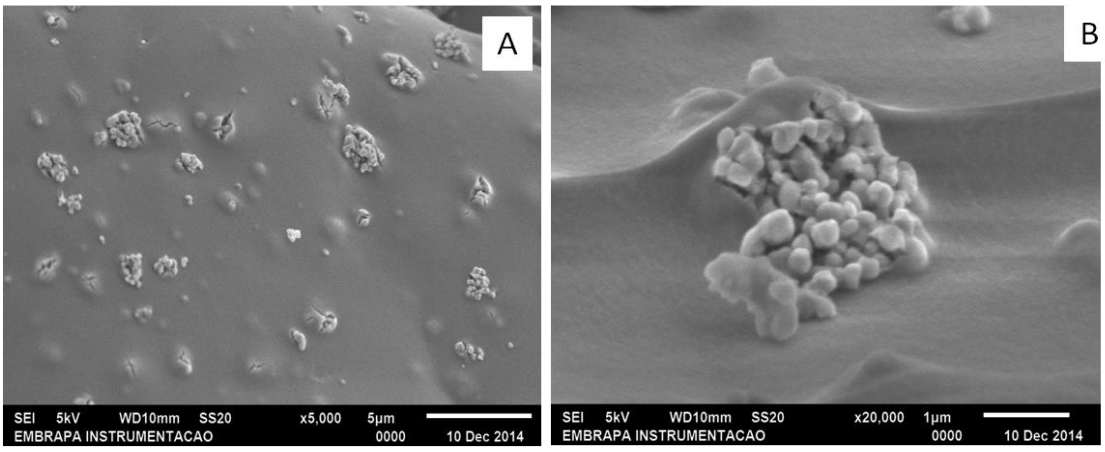

Figure 4.28 - SEM micrographs of mixed phase powder calcined at 450 °C (P450).

The micrographs show a continuous film was formed over the rutile powder particles. In some areas, rutile particles are exposed at regions with

cracks. The microstructure of the powder permits the extrapolation of the film properties from the powder.

Figure 4.29 presents the TEM micrographs of the mixed phase powders.

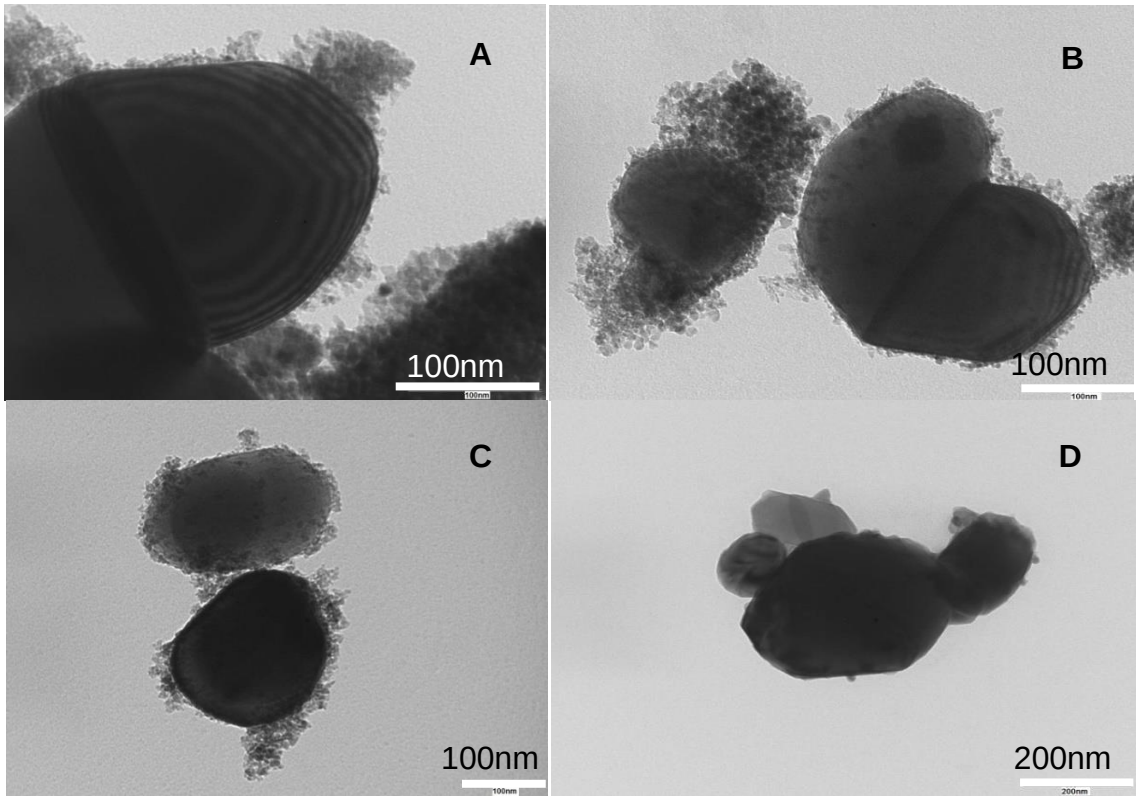

Figure 4.29 - TEM micrographs of mixed phase powders produced from a mixture rutile powder and Ti^{4+} resin that was calcined at various temperatures: *A)* P350 (350 °C/12h), *B)* P450 (450 °C/2h), *C)* P500 (500 °C/2h) and *D)* P1000 (1000 °C/2h).

They contain large particles assigned to rutile phase and smaller particles believed to be anatase. The terrace feature observed in the SEM micrograph of the substrate (Figure 4.8) is also evident in Figure 4.29A and is in agreement with the fact that it is intrinsic of the powder. It further confirms that the large particles are related to rutile phase.

Anatase fine particles tend to grow and segregate at the edges and surfaces of rutile particles suggesting that these places have lower nucleation energy. The powder calcined at 1000 ^{o}C shows the absence of agglomerates of fine anatase particles at the outlines of the particles or over the surface.

Apparently, at this temperature, anatase particles have transformed into rutile through particle growth and coalescence.

Figure 4.30 shows the bright field image of P500, corresponding dark field image and a selected diffraction pattern.

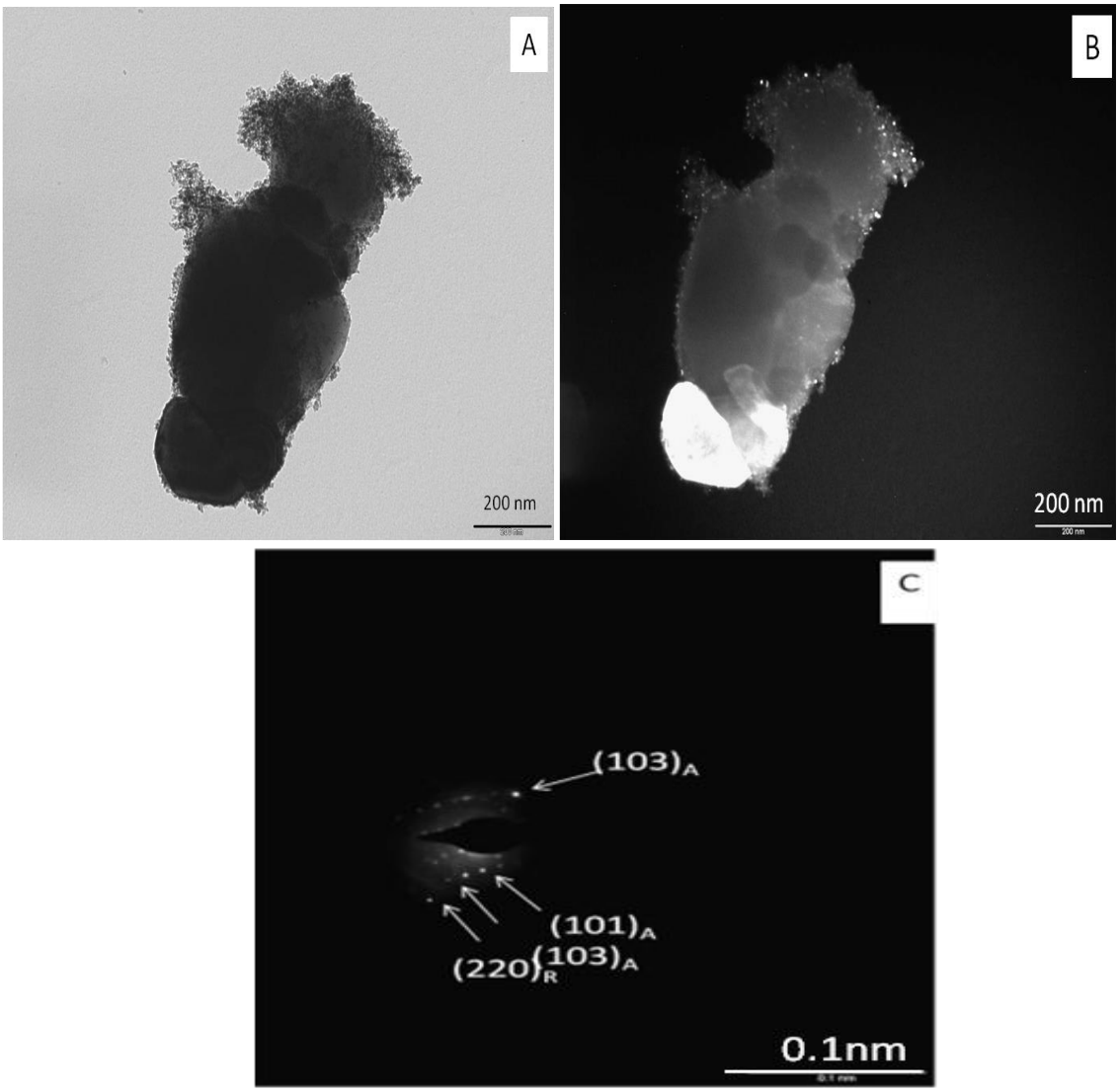

Figure 4.30 - TEM micrographs of mixed phase powder produced from a mixture of rutile powder and Ti^{4+} resin that was calcined at 500 °C/2h(P 500): *A)* bright field; *B)* dark field*; C*) selected area diffraction.

The difference in contrast of the dark field image (Figure 4.30B) indicates bright areas with a particular orientation. The selected area diffraction of the bright area (Figure 4.30C) reveals aligned spots indicative of reflection from individual crystallites or single crystals. Thus, a low degree of orientation is

shown in this region. Anatase reflections from (101) and (103) planes were detected as well as reflections from (220) rutile, showing that there was no topotactic effect, i.e., anatase was surface nucleated but did not convert to rutile.

Figure 4.31 shows a dark field image of P1000 and a selected area diffraction pattern.

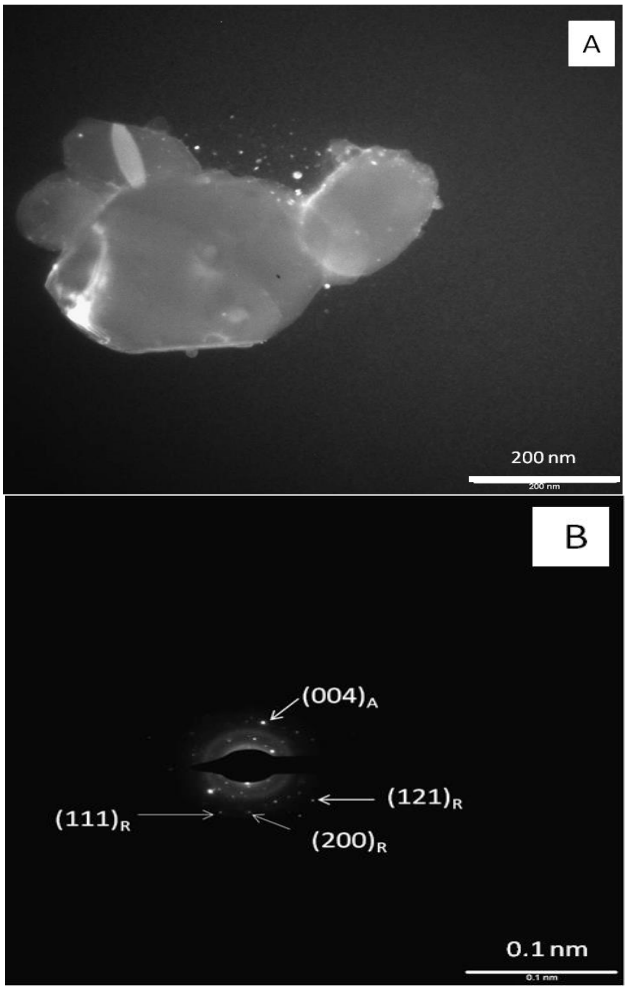

Figure 4.31 - TEM micrographs of mixed phase powder produced from a mixture of rutile powder and Ti^{4+} resin that was calcined at 1000 °C/2h (P 1000): *A)* dark field*; B*) selected area diffraction.

The presence of diffuse rings and bright spots indicate that the diffracted region is polycrystalline. The crystallites in the outer rings are associated with rutile in the (111), (200) and (121) planes while a spot is indicative of anatase in the (004) plane. Since at this temperature all anatase phase is transformed into

rutile, the presence of anatase could indicate that the powder contains anatase impurities which are retained at high temperatures. The presence of silica and alumina might contribute to this behavior. It is interesting to note that anatase vibrational mode in the powder was also detected through Raman spectroscopy (Figure 4.27).

4.7 Photocatalytic performance

4.7.1 Rhodamine B degradation

The discoloration of Rhod-B was monitored at different time intervals utilizing the absorbance spectra of the molecule. Figure 4.32 and Figure 4.33 present the absorbance spectra of Rhod-B in the presence of the samples after UV irradiation for the first cycle. The rest of the cycles were not presented here to reduce redundancy.

Rhod-B is noted to have a maximum absorption peak around 544 nm wavelength and the reduction of the intensity of this peak with time is utilized as the measure of the rate of discoloration

.

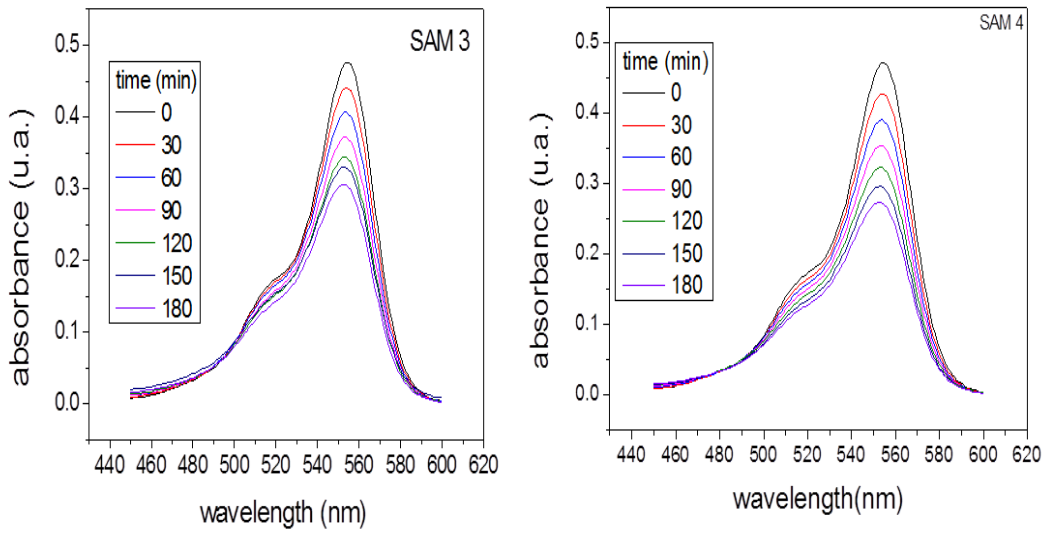

Figure 4.32 - Absorption spectra of Rhod-B after UV irradiation in the presence of SAM 3 and SAM 4 for a period of 180 minutes.

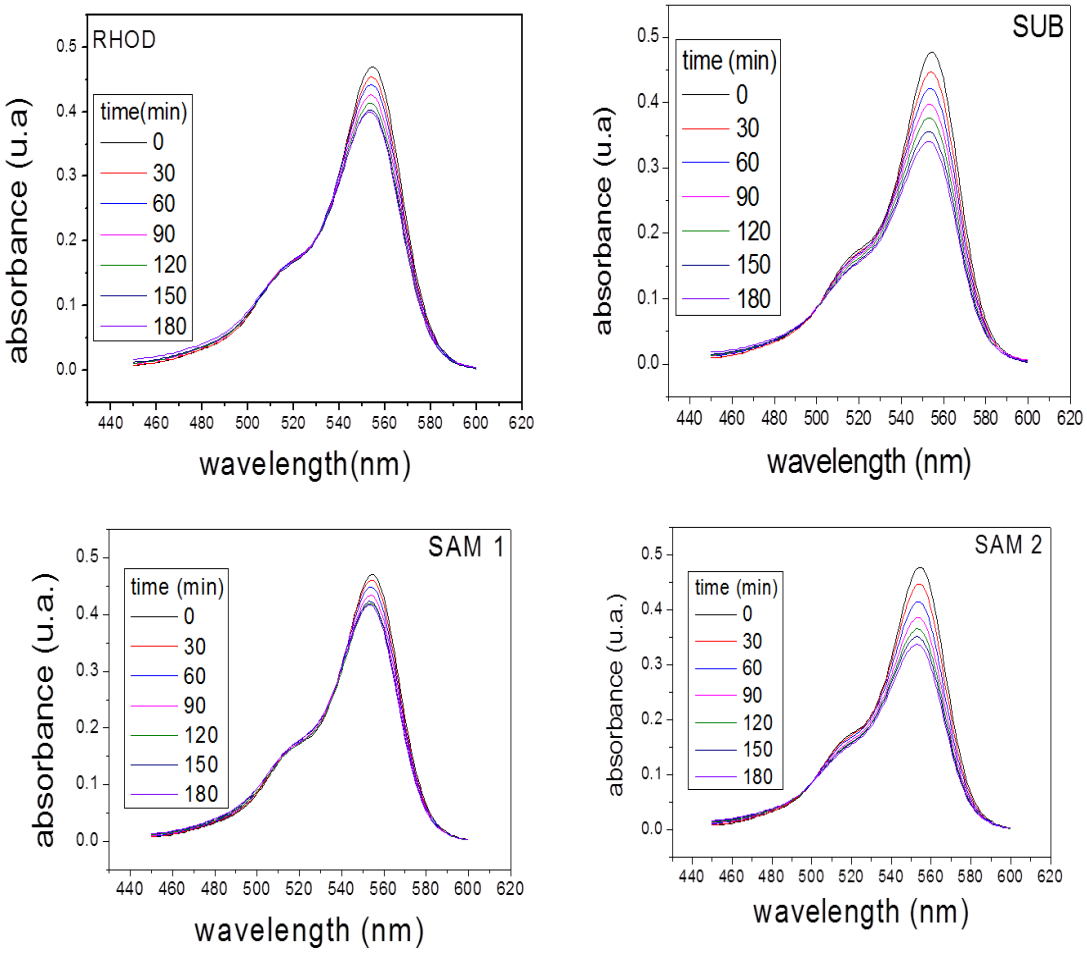

Figure 4.33 - Absorption spectra of Rhod-B after UV irradiation in the presence of Rhodamine B (RHOD), rutile substrate (SUB), SAM 1 and SAM 2 for a period of 180 mins.

The spectra of all the samples show a reduction in the intensity of the peak with an increase in irradiation time. The position of the absorption peak monitored at 544 nm did not show any significant dislocation during the irradiation period for the first cycle, an indication of the absence of hypsochromic or bathochromic shifts.

Hypsochromic shift is a phenomenon that occurs in dyes in general, when the energy between the ground state and excited state is increased (blue shift) such that the maximum absorption wavelength is shifted to shorter wavelengths [158]. The opposite occurs in bathochromic shifts. Usually, hypsochromic or bathochromic shift indicates changes in the conjugate structure of the dye and provide information on the degradation pathway of the molecule during photocatalysis.

Rhod-B presents two main degradation paths: cleavage of the chromophore ring and N-deethylation. With cleavage, the chromophore bonds are broken. Degradation of Rhod-B through this path does not cause the dislocation of the maximum absorption wavelength. For the second degradation pathway, N-deethylation, where the methyl group from the nitrogen (*N*)-containing functional group is detached, the wavelength is shifted to lower or higher wavelength depending on the byproduct formed [159]. Therefore, the degradation path of Rhod-B in the presence of the films is believed to be bond cleavage. However, the complete absence of N-deethylation reactions can not be confirmed since both mechanisms can take place at different stages of Rhod-B degradation using TiO_2 nanoparticles [159]. Figure 4.34 presents the reduction of the concentration of the Rhod-B in solution with the presence of the films for all four cycles.

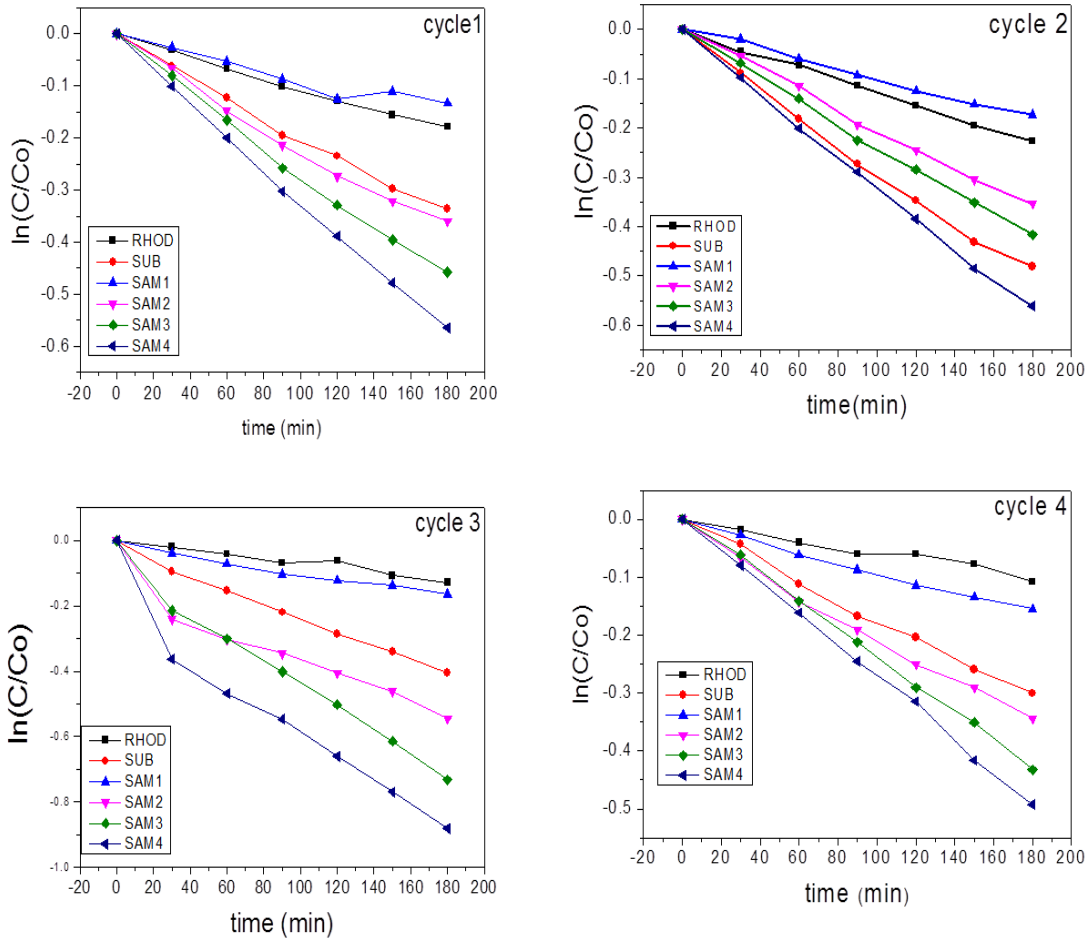

Figure 4.34 - Reduction of Rhod-B concentration with time for cycle 1, cycle 2, cycle 3 and cycle 4.

In general, the percentage of Rhod-B chromophore removed after 3 hours of UV irradiation was up to 43%, 43%, 54% and 39% for cycle 1, 2, 3 and 4 respectively. The values suggests that the photocatalytic properties of the samples are stable and could be maintained after several applications

The kinetic behavior of the samples with respect to Rhod-B degradation is very important to understanding the possible factors that affect the process. Also, it is a very simple way to evaluate the photocatalytic efficiency of the films

From the first rate order kinetic law and according to the experimental set ,Equation 4.1 clearly defines the rate order of the photodegradation of Rhodamine B.

$$\frac{-d[Rhodamine\ B]}{dt} = k[Rhodamine\ B\ ][surface\ area\ ] \tag{4.1}$$

where surface area represents the concentration of active sites in the photocatalyst (proportional to the surface area of the films) which is constant. Therefore, Equation 4.1 is reduced to Equation 4.2:

$$\frac{-d[Rhodamine\ B]}{dt} = k[Rhodamine\ B\ ] \tag{4.2}$$

where k' = k[AS];

The integration of Equation 4.2 results in Equation 4.3:

$$-\ln\left(\frac{[Rhodamine\ B\ ]}{[Rhodamine\ B\ ]_0}\right) = k't \tag{4.3}$$

In accordance with Equation 4.3, if ln([*Rhodamine B]/ [Rhodamine B]*) is plotted as a function of t, a straight line should be obtained whose slope is k' and the quality of the linear fit is verified through linear regression (R^2). Thus, a linear fit of the plots in Figure 4.38 provides the kinetic constants of the degradation process.

Table 4.9, 4.10, 4.11 and 4.12 contain the kinetic constant k', standard error and linear regression (R^2) of the samples for the degradation of Rhod-B for cycle 1 through to cycle 4, respectively.

Table 4.9 - Kinetic constant (*k*'), standard error and linear regression of all the samples for cycle 1.

Sample	$K'.10^{-3}$ (min^{-1})	Standard error.10^{-3}	R^2
RHOD	1.01	0.03	0.993
SUB	1.9	0.07	0.993
SAM 1	0.76	0.10	0.999
SAM 2	2.04	0.01	0.994
SAM 3	2.58	0.07	0.985
SAM 4	3.14	0.05	0.912

Table 4.10 - Kinetic Constant (*k*'), standard error and linear regression of all the samples for cycle 2.

Sample	$K'.10^{-3}$ (min^{-1})	Standard error.10^{-3}	R^2
RHOD	1.26	0.03	0.997
SUB	2.73	0.09	0.992
SAM 1	1.01	0.03	0.992
SAM 2	2.02	0.05	0.997
SAM 3	2.33	0.04	0.998
SAM 4	3.15	0.05	0.999

Table 4.11 - Kinetic constant (*k*'), standard error and linear regression of all the samples for cycle 3.

Sample	$K'.10^{-3}$ (min^{-1})	Standard error.10^{-3}	R^2
RHOD	0.69	0.06	0.952
SUB	2.19	0.07	0.994
SAM 1	0.88	0.05	0.917
SAM 2	2.59	0.02	0.982
SAM 3	3.81	0.04	0.887
SAM 4	4.34	0.06	0.974

Table 4.12 - Kinetic constant (*k*'), standard error and linear regression of all the samples for cycle 4.

Sample	$K'.10^{-3}$ (min^{-1})	Standard error.10^{-3}	R^2
RHOD	0.60	0.05	0.959
SUB	1.70	0.06	0.994
SAM 1	0.87	0.04	0.991
SAM 2	1.90	0.03	0.990
SAM 3	2.41	0.07	0.998
SAM 4	2.74	0.03	0.999

For all the cycles, a low standard error is associated with the estimate of the rate constants, thereby confirming the accuracy of the films in degrading Rhod-B by pseudo first order reaction. In fact, the linear model used to fit the data is appropriate as the R-squared values for all cycles are ranging between 0.999 and 0.877. Figure 4.35 contains a bar representation of the *k'* values for all the samples at different cycles.

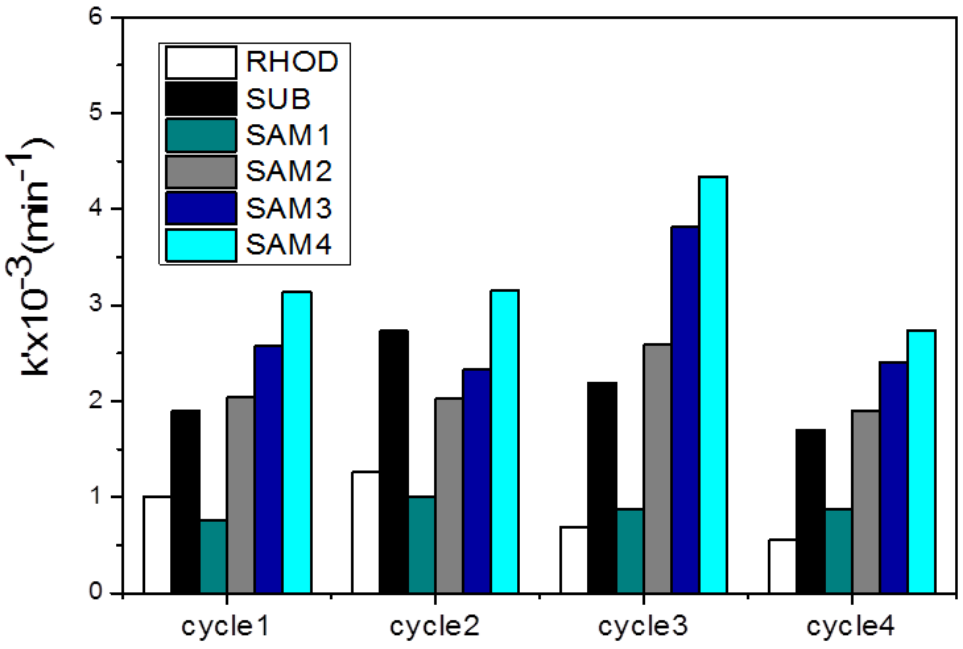

Figure 4.35 - Kinetic Constant of the samples for the four cycles.

From the cycles, Rhod-B containing no sample showed a considerable rate constant under UV irradiation. A possible explanation to this behavior is photolysis, where the dye can absorb UV light radiation whose energy is sufficient to break bonds in the chromophore group [131]. However, photolysis represents a small fraction of the degradation process and does not effectively lead to mineralization. For all the cycles, Rhod-B solutions containing the films and pristine substrate showed better photocatalytic activity compared to raw Rhod-B except for SAM 1 in the second and third cycle. This shows that the presence of the films is crucial for improved degradation of Rhod-B.

When the solutions are irradiated in the presence of the films, photons from the UV light are absorbed by TiO_2 and excitation of electrons take place with consequent formation of holes and electrons in the valence and conduction

band respectively. The hydroxyl and superoxide radicals are responsible for the oxidation of the dye molecules by the films.

The recombination rate of the holes and electrons in the photocatalytic process can be reduced if the heterojunction formed between anatase and rutile phase is such that the electrons are transferred to local traps in the rutile phase. The optical bandgap plays a key role in the recombination rates because the lower the bandgap formed between anatase and rutile, the lower the energy barrier between the phases thereby faster electron transfer. In general, the properties of the TiO_2 films such as quality, thickness, interface with rutile substrate, phase composition, crystallite size of anatase phase can affect photocatalytic activity.

It can be seen that the films calcined at higher temperatures (SAM 3 and SAM 4) showed better photocatalytic activity than the films calcined at lower temperatures for all the cycles. For the higher temperature calcined films, anatase phase is present and is very crystalline. Further, the quantity of residual carbon which may affect catalytic process is apparently lower. Results from the grazing incidence X-ray analysis confirm the near absence of anatase in the lower temperature calcined films. In this way, the radicals formed on the surface of the films containing anatase may be higher compared to the lower crystalline films.

Fan et al. (2012) degraded Rhod-B with TiO_2 and observed that crystallinity affects the degradation process [159]. They reported that quicker N-deethylation and slower cleavage of conjugated chromophore structure was susceptible in Rhod-B degradation with less crystalline anatase while crystalline anatase lead to slower N-deethylation and quicker cleavage of the conjugated chromophore. Since there was no apparent blue shift in the samples, then Rhod-B molecules in the presence of the lower calcined films might be undergoing cleavage at a slower rate.

The bandgap measured for SAM 4 was close to the rutile substrate which indicates that electron transfer from anatase to rutile can be facilitated. Easy electron transfer and trapping could reduce recombination and increase charge separation of charge carriers. The lower optical bandgap of SAM 4 could

contribute to its superior photoctivity. In fact, SAM 1, SAM 2 and SAM 3 presented close bandgap values but the discrepancy in their photocatalytic activities indicates that photocatalytic activity did not depend solely on the reduction of recombination but on several factors.

The quality of the films in terms of homogeneity can be a determining factor during photocatalysis because it reduces the surface area of the film for active sites and adsorption of the Rhod-B molecules. In the samples, there was no clear correlation between film homogeneity and photocatalytic activity for all cycles. However, SAM 4 with better film quality presented improved photoactivity than the other samples. It is believed that SAM 3 and SAM 4 with a more crystalline anatase phase than the other samples are likely to have a better interface which may contribute to lower recombination rate. Strikingly, the substrate showed better photoactivity than some of the films especially for SAM 1. This sample was calcined at 350 °C, where anatase might be in the amorphous form and less active with the irradiation of light.

The results from grazing incidence diffraction X-ray and conventional X-ray showed that it has very negligible anatase phase, thus the near absence of anatase coupled with high residual carbon might hinder light absorption and increase adsorption of the Rhod-B molecules [160]. Since dye removal rate of SAM 1 might be lower than the rate of adsorption, the active sites might be poisoned leading to lower photoactivity. With this hypothesis, the pristine substrate has less barriers in absorbing light and can have more surface area for the catalytic process. Also it has been reported that superoxide radicals produced by rutile are very stable compared to anatase [161].

From the *k'* values, the trends in the cycles show that the samples can be used repeatedly and still maintain their photocatalytic properties. In general, the kinetic constant of the individual samples were practically identical for cycle 1, 2 and 4 despite drops in kinetic constant values. On the contrary, a significant increase in the kinetic constant was observed in the third cycle for samples (SAM 3 and SAM 4). Further SAM 3 and SAM 4 followed a consistent trend for the photodegradation of Rhod-B suggesting that calcination at higher temperature enhanced the activity of anatase films.

4.7.2 Atrazine degradation

The photocatalytic activity of the samples was tested for the degradation of Atrazine, a herbicide. For this purpose, ATZ solutions were irradiated with UV light in the presence of the films and the resultant spectra were analyzed. Figure 4.36, 4.37 and 4.38 present the spectra of ATZ in the presence of the samples for cycle 1 after UV irradiation.

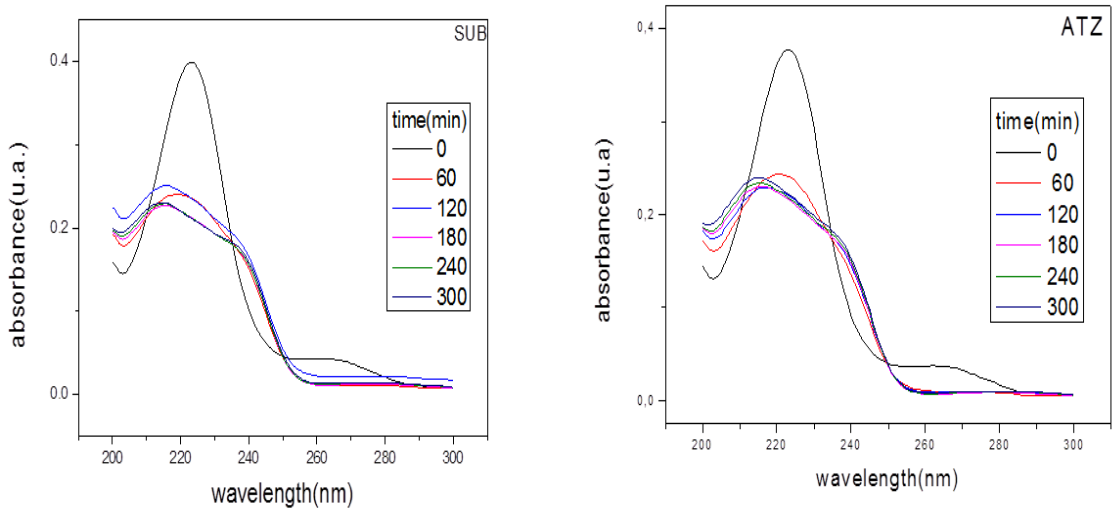

Figure 4.36 - UV-vis spectra of Atrazine (ATZ) after UV irradiation in the presence of rutile substrate (SUB) and raw Atrazine for a period of 300 minutes.

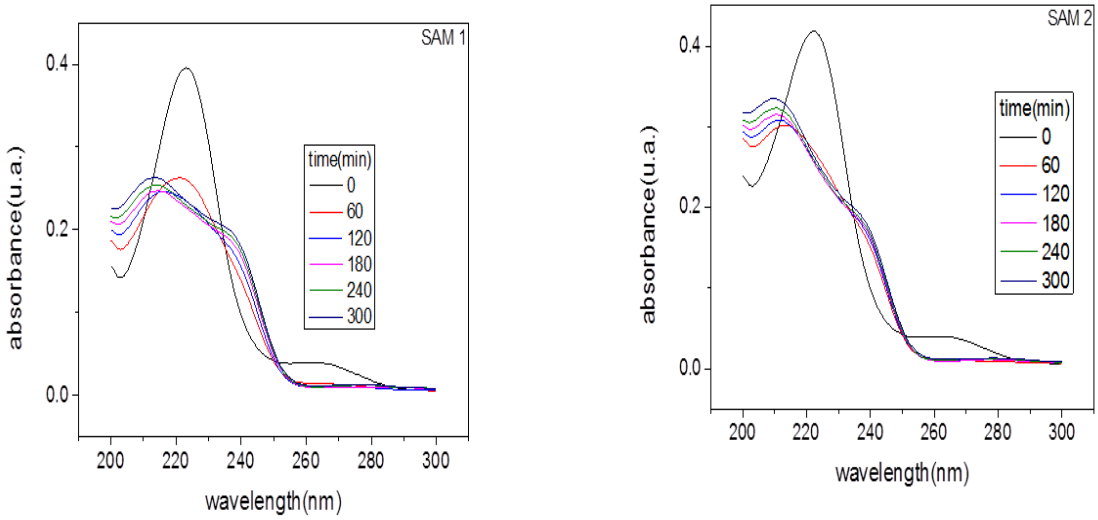

Figure 4.37 - UV-vis spectra of Atrazine after UV irradiation in the presence of film calcined at 350 °C/12h (SAM 1) and film calcined at 400 °C/2h (SAM 2) for a period of 300 minutes.

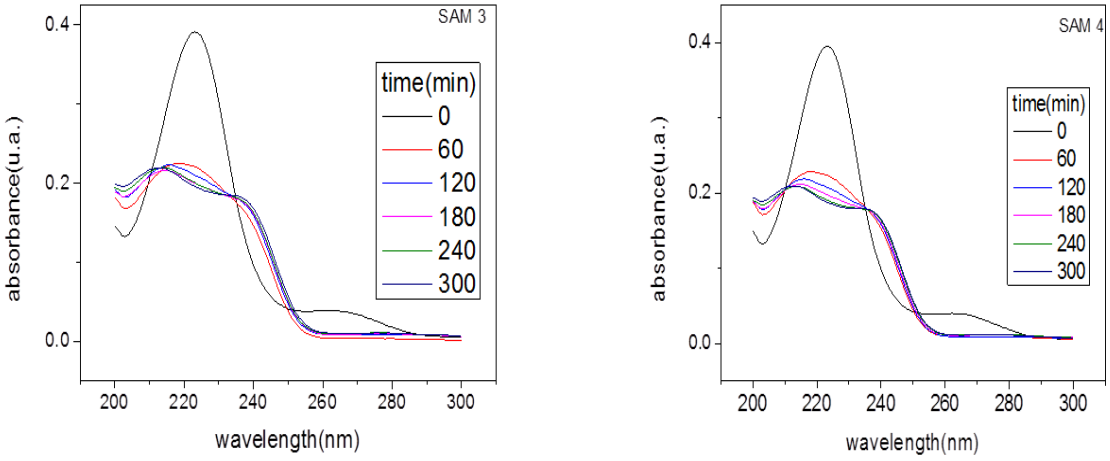

Figure 4.38 - UV-vis spectra of Atrazine after UV irradiation in the presence of film calcined at 450 °C/2h (SAM 3) and film calcined at 500 °C/2h (SAM 4) for a period of 300 minutes.

The spectra are characterized by ATZ molecule which has a maximum absorption wavelength of 223 nm and a second maximum absorption wavelength at 263 nm. Absorbance at these wavelengths was monitored before and after UV irradiation to calculate the reduction of the concentration of the molecule in solution. After 60 minutes, a significant reduction of almost 50 % of the concentration of ATZ at 223 nm is observed for all samples including raw ATZ solution and the absorbance peak at 263 nm was completely reduced to zero which is equivalent to 100% degradation of ATZ.

S-triazine dyes such as Atrazine and Ametryn have been reported to have a rapid degradation behavior after UV irradiation [66,149]. This behavior has been associated to adsorption and degradation of the molecule. The peak at 263 nm can be considered as pure ATZ since the formation of byproducts at this wavelength is low, so its complete absence suggests a transformation of the molecules into byproducts [162]. Further, it shows that ATZ is more susceptible to degradation but the byproducts formed in the process tend to hinder the complete mineralization of ATZ in solution since they are more resistant to degradation.

One of the problems associated with byproducts is that they can poison the active sites of the films, reducing the degradation process. Thus, for

subsequent irradiation, the efficiency of the films in the mineralization of ATZ depends on the oxidation of the byproducts formed.

The peak at 223 nm was monitored after 60 minutes up to the end of the experiment. The subsequent spectra after 60 minutes show the formation of unidentified byproducts with peaks near 212 nm and 236 nm maximum peaks.The peaks can be precisely identified by chromatograpy. However, it was not within the scope of the study. The performance of the films in degrading ATZ and its byproducts can be more comprehensive through plots of ATZ concentration versus time.

Figure 4.39 shows the effect of UV irradiation in the presence of the samples on the degradation of ATZ monitored at 223 nm.

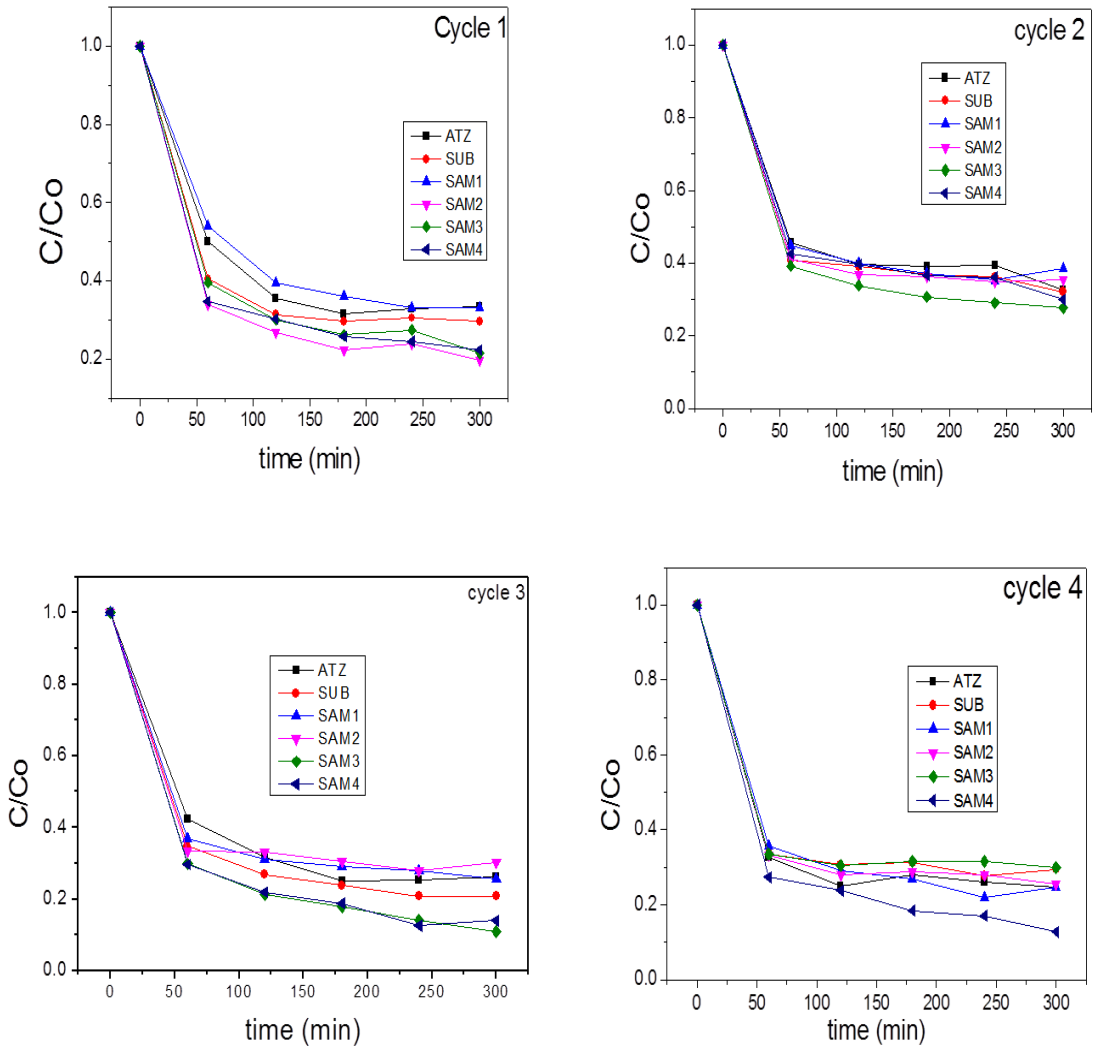

Figure 4.39 - The reduction of ATZ concentration with time for cycle 1, cycle 2, cycle 3 and cycle 4.

From the graphs, it is possible to see the degradation of ATZ after 60 minutes of irradiation for all the cycles.

In general, a greater reduction in absorbance was observed at 60 minutes in all the samples for all cycles followed by a slower degradation after 60 minutes due to factors such as formation of byproducts and poisoning of active sites. The percentage of ATZ molecules in solution deduced from the absorbance spectra at the end of the photocatalytic tests was not so deviant among the cycles despite the continuous formation of byproducts. It is therefore believed that the films to some extent were resistant to ATZ poisoning.

The role of specific properties on photocatalytic activity was not consistent for the samples. For example, cycle 1, SAM 2 presented better activity than the higher temperature calcined films whereas in cycles 2, 3 and 4, the higher temperature calcined films (SAM 3 and SAM 4) presented higher photocatalytic activity. It is important to note that the reduction in ATZ concentration is not very deviant from one film to the other, therefore, minimal changes in film properties during the process can enhance or reduce photocatalytic activity. Considering that ATZ degradation is characterized by the formation of resistant byproducts, several factors are involved contrary to Rhod-B degradation. The type and quantity of byproduct can affect the degradation mechanisms of the film in each cycle. From the photocatalytic trend of the samples, SAM 3 and SAM 4 depict the contribution of anatase phase to the degradation process. Its crystallinity seems to enhance the production of radicals for the degradation process. The recombination rate might be lower for SAM 4, prolonging the lifetime of photogenerated carriers.

For SAM 1 and SAM 2, as previously mentioned, carbon can assist in adsorption and it is possible that the desorption process was slower for these films, resulting in pronounced poising of the active sites. This hypothesis may be the reason for low photoactivity in addition to lower crystalline phase especially for the lower temperature calcined films. The kinetics of the degradation process was also studied.

The plots in Figure 4.36 were fitted to a first order exponential decay profile. The exponential model is represented by Equation 4.4:

$$y = yo + Ae^{-kt} \tag{4.4}$$

where yo = offset, A = amplitude, t = time, k = kinetic constant.

Typically, a first order exponential decay model is characterized by a rapid decrease after which the rate becomes slow and levels off approaching an equilibrium lower limit. The degradation pattern of ATZ suggests that this model is appropriate for understanding the kinetics behind the degradation process.

The exponential decay parameters are interpreted in real world context utilizing the parameters of the photocatalytic process. First, Equation 4.4 is analyzed at an infinite time (Equations 4.5 and 4.6):

$$\lim_{t\to\infty}(yo + Ae^{-kt}) = yo \tag{4.5}$$

$$y = yo \tag{4.6}$$

It can be observed that at a sufficiently long time, the system approaches Equation 4.6. In the context of the degradation graphs, it represents the degradation of ATZ and the reduction in ATZ concentration becoming asymptotic to a lower limit. Thus, yo represents the byproducts in the system after the rapid degradation of ATZ. The formation and resistance of these byproducts control the kinetics of the process at this stage. Then, yo is accepted as the concentration of byproducts in the system which can be represented by C_R (Equation 4.7) and y as the reduction in concentration of ATZ with time (C/Co).

$$\frac{C}{C_O} = C_R \tag{4.7}$$

where C/Co is the reduction in initial concentration C_o at a certain time t.

Now, how does the model describe what happens at the initial stages of the degradation process? The limit of Equation 4.4 at time 0 is shown in Equations 4.8, 4.9 and 4.10:

$$\lim_{t\to 0}(yo + Ae^{-kt}) = A + yo \tag{4.8}$$

$$y = A + yo \tag{4.9}$$

$$\frac{C}{C_O} = A + C_R \tag{4.10}$$

If it is considered that at time *0*, there is no degradation, then *C/Co* = 1 and Equation 4.10 becomes:

$$A = 1 - C_R \tag{4.11}$$

If all the assumptions are true, the constant *A* is a measure of the efficiency of the films in degrading the byproducts.

It is apparent that the higher the C_R content, the lower the efficiency of the films in oxidizing ATZ. With this analysis, the exponential model is modified to satisfy the conditions of ATZ degradation and Equation 4.12 is represented by the parameters of the degradation process and becomes Equation 4.13:

$$y = yo + Ae^{-kt} \tag{4.12}$$

$$\frac{C}{C_o} = C_R + Ae^{-kt} \tag{4.13}$$

Where *C/Co* is the reduction in initial concentration C_o at a certain time *t*, C_R is the concentration of byproducts and *A* is the efficiency of the process or fit constant. The kinetic constant is $k = \frac{1}{t}$, and the parameters for the fit are provided by the Origin software 9th version.

Table 4.13, 4.14, 4.15 and 4.16 show the values derived from fitting the graphs (Figure 4.39) utilizing an exponential decay of first order. The standard errors associated with the parameters indicate that the precision of the values is high.

A first order exponential decay model is confirmed as a good fit for the degradation process due to the high non-linear regressions presented. It is therefore acceptable to classify the degradation of ATZ by the films as being of first order exponential decay.

As was previously discussed, *yo* values indicate the amount of residual byproduct after the degradation process. It was observed that the residue formed from cycle 1 through to cycle 4 ranged from 15% to 37%. The lower

range values suggest that the films have the potential to degrade the byproducts from ATZ degradation.

Accordingly, the A constants which is a measure of the efficiency of degrading ATZ byproducts for all cycles showed a lower value of 63% and a peak value of 85%.

Table 4.13 - Fit parameters of the degradation process and R^2 values for cycle 1.

Sample	C_R	A	K (min^{-1})	R^2
ATZ	0.32 ± 0.01	0.68 ± 0.02	0.023	0.997
SUB	0.30 ± 0.00	0.70 ± 0.01	0.032	1
SAM 1	0.33 ± 0.00	0.67 ± 0.01	0.019	0.999
SAM 2	0.22 ± 0.01	0.77 ± 0.03	0.031	0.994
SAM 3	0.25 ± 0.02	0.75 ± 0.03	0.026	0.991
SAM 4	0.25 ± 0.02	0.75 ± 0.03	0.032	0.992

Table 4.14 - Fit parameters of the degradation process and R^2 values for cycle 2.

Sample	C_R	A	K (min^{-1})	R^2
ATZ	0.37 ± 0.02	0.63 ± 0.04	0.033	0.984
SUB	0.36 ± 0.01	0.64 ± 0.03	0.041	0.989
SAM 1	0.37 ± 0.01	0.63 ± 0.02	0.035	0.996
SAM 2	0.36 ± 0.00	0.64 ± 0.01	0.041	0.999
SAM 3	0.30 ± 0.01	0.70 ± 0.02	0.032	0.994
SAM 4	0.35 ± 0.02	0.65 ± 0.04	0.034	0.979

Table 4.15 - Fit parameters of the degradation process and R^2 values for cycle 3.

Sample	C_R	A	K (min^{-1})	R^2
ATZ	0.26 ± 0.01	0.74 ± 0.02	0.024	0.997
SUB	0.22 ± 0.01	0.78 ± 0.02	0.029	0.996
SAM 1	0.28 ± 0.01	0.72 ± 0.02	0.034	0.996
SAM 2	0.30 ± 0.01	0.70 ± 0.02	0.051	0.995
SAM 3	0.15 ± 0.02	0.85 ± 0.04	0.027	0.990
SAM 4	0.16 ± 0.02	0.84 ± 0.04	0.028	0.990

Table 4.16 - Fit parameters of the degradation process and R^2 values for cycle 4.

Sample	C_R	A	K (min^{-1})	R^2
ATZ	0.26 ± 0.01	0.74 ± 0.02	0.040	0.997
SUB	0.30 ± 0.01	0.70 ± 0.02	0.048	0.997
SAM 1	0.25 ± 0.01	0.75 ± 0.02	0.031	0.993
SAM 2	0.27 ± 0.01	0.73 ± 0.02	0.042	0.998
SAM 3	0.31 ± 0.00	0.69 ± 0.01	0.054	0.999
SAM 4	0.17 ± 0.02	0.83 ± 0.05	0.032	0.986

In general, the variation in residue concentration was not very significant between the cycles and there was no particular trend observed. It is very difficult to associate a particular trend to the degradation of ATZ since the molecule is very complex compared to Rhod-B. And, due to the structure of the ATZ, it is easier to form various byproducts However, it is observed that high efficiency of the films results in lower byproduct concentration. For samples calcined at higher temperatures, this is associated to adequate crystallinity. Also, the production of byproducts may alter mechanisms during the degradation process.

In order to clearly state the types of byproducts formed in each ATZ sample, it is necessary to carry out chromatography studies which is not within the scope of the project. However, it is of great importance because the byproduct formed for each sample may not necessarily be the same which could incur bias analysis of their degradation performance.

5 CONCLUSION

For the experimental conditions adopted in this work, it is possible to conclude that anatase films were successfully grown on rutile substrate by the polymeric precursors method without the complete transformation of the anatase films into rutile. Anatase in the (101) plane was identified for the films calcined at 450 and 500 °C.

Rutile tends to suppress the growth of anatase for lower temperature calcined films and anatase phase is stabilized for higher temperature calcined films. The optical bandgaps of the films were altered due to the presence of the substrate.

The quality of the films grown on rutile substrate depends on surface topography compared to the films grown on glass.

Rutile has shown to be a candidate for immobilizing TiO_2 films as it supports anatase growth and presents considerable photocatalytic activity.

Anatase film on rutile substrate assembly has potential as a catalyst for the degradation of dyes and herbicides.

The kinetics of Rhod-B and ATZ degradation followed a pseudo first order and first order exponential decay respectively. The films calcined at 450 °C and 500 °C showed superior photocatalytic activity for Rhod-B degradation than the films calcined at 350 °C and 400 °C. This behavior was attributed to the adequate crystallinity of anatase. Therefore, crystallinity of anatase is crucial for photocatalytic activity.

6 SUGGESTIONS FOR FUTURE STUDIES

- The phase evolution and photocatalytic properties of TiO_2 films deposited on rutile substrates for temperatures above 500 °C.

- The effect of the number of deposited layers on the photocatalytic activity of the films.

- The photocatalytic properties of anatase phase films deposited on rutile phase films.

- Detailed analysis of the mixed phase powder employing Transmission electron microscopy in search of oriented nucleation and growth of anatase on rutile particles.

- Characterization of the interface between anatase film and rutile substrate by transmission electron microscopy.

- Characterization of the interface between anatase film and rutile utilizing focused ion beam.

- Surface characterization by atomic force microscopy taking into consideration larger focus areas in order to study the general aspect of the surface of the films and substrate.

7 REFERENCES

[1] Statistics (2008), Ministry of Agriculture Brazil. Available at: <http://www.agricultura.gov.br> Accessed:10.11.2014.

[2] ARRAES, A. A; BARRETO, F. M. S; ARAÚJO, J. C. Use of Atrazine and groundwater availability in Brazil: case study Tianguá. In: **World Water Congress** of IAHR, 13, 2008, Montpellier. Anais..2008. Montpellier: IAHR: CD Rom.

[3] JACOMINI, A. E. et al. Assessment of Ametryn contamination in river water, river sediment, and mollusk bivalves in Sao Paulo State, Brazil. **Archives of Environmental Contamination and Toxicology**, v. 60, n. 3, p. 452-461, 2011.

[4] NOGUEIRA, E. N. et al. Currently used pesticides in water matrices in Central-Western Brazil. **Journal of the Brazilian Chemical Society**, v. 23, n. 8, p. 1476-1487, 2012.

[5] CAPPELINI, L. T. D. **Análise dos pesticidas Ametrina, Atrazina, Diuron e Fipronil em amostras de água do Ribeirão do Feijão.** 2008. 69 p. Dissertation (Masters Analytical Chemistry)–Institute of Chemistry São Carlos, University of São Paulo, São Carlos, 2008.

[6] Monitoring of some pesticides by SAAE. Available at: <http://www.vitorandrade.com.br/templates/saae/laboratorio_olaboratorio.php> Accessed: 10.11.2014.

[7] Monitoring of some pesticides by SAAE. Available at: <http://www.saaeara.com.br/informacao/agua/> Accessed: 10.11.2014.

[8] RIBEIRO, A. R. et al. An overview on the advanced oxidation processes applied for the treatment of water pollutants defined in the recently launched Directive 2013/39/EU. **Environment International**, v. 75, p. 33-51, 2015.

[9] LAZAR, M. A.; VARGHESE, S.; NAIR, S. Photocatalytic water treatment by titanium dioxide: recent updates. **Catalysts**, v. 2, n. 4, p. 572-601, 2012.

[10] SHAN, A. Y.; GHAZI, T. I. M.; RASHID, S. A. Immobilization of titanium dioxide onto supporting materials in heterogeneous photocatalysis: A review. **Applied Catalysis A: General**, v. 389, n. 1-2, p. 1-8, 2010.

[11] PAZ, Y. Application of TiO_2 photocatalysis for air treatment: Patents' overview. **Applied Catalysis B: Environmental**, v. 99, n. 3-4, p. 448-460, 2010.

[12] YANG, G.; YAN, Z.; XIAO, T. Preparation and characterization of SnO_2/ZnO/TiO_2 composite semiconductor with enhanced photocatalytic activity. **Applied Surface Science**, v. 258, n. 22, p. 8704-8712, 2012.

[13] KENANAKIS, G.; KATSARAKIS, N. ZnO nanowires on glass via chemical routes: A prospective photocatalyst for indoors applications. **Journal of Environmental Chemical Engineering**, v. 2, n. 3, p. 1416-1422, 2014

[14] YUAN, J. et al. TiO_2/SnO_2 double-shelled hollow spheres-highly efficient photocatalyst for the degradation of rhodamine B. **Catalysis Communications**, v. 60, p. 129-133, 2015.

[15] FENOLL, J. et al. Semiconductor-sensitized photodegradation of s-triazine and chloroacetanilide herbicides in leaching water using TiO_2 and ZnO as catalyst under natural sunlight. **Journal of Photochemistry and Photobiology A: Chemistry**, v. 238, p. 81-87, 2012.

[16] FUJISHIMA, A.; ZHANG, X. Titanium dioxide photocatalysis: present situation and future approaches. **Comptes Rendus Chimie**, v. 9, n. 5-6, p. 750-760, 2006.

[17] MANE, R. S. et al. Unprecedented coloration of rutile titanium dioxide nanocrystalline. **Micron**, v.38, n.1, p. 85-90, 2007.

[18] FISHER J.; EGERTON, T. A. Titanium compounds, inorganics in: **Kirk-Othmer Encyclopedia of chemical technology**. New York: Wiley & Sons, 2001.

[19] NAVROTSKY A.; KLEPPA, O. J. Enthalpy of the Anatase-Rutile transformation. **Journal of the American Ceramic Society**, v. 50, n.

11, p. 626, 1967.

[20] JIANG, L.; ZHOU, G. Facile synthesis of monodispersed nanocrystalline anatase TiO_2 particles with large surface area and enhanced photocatalytic activity for degradation of organic contaminant in wastewaters. **Materials Science in Semiconductor Processing**, v. 15, n. 1, p.108-111, 2012.

[21] KAO, LH.; HSU, TC.; CHENG, KK. Novel synthesis of high surface area ordered mesoporous TiO_2 with anatase framework for photocatalytic applications. **Journal of colloid and Interface science**, v.341, n.2, p.359-365, 2010.

[22] MAZINANI, B. et al. Photocatalytic activity, surface area and phase modification of mesoporous SiO_2–TiO_2 prepared by a one-step hydrothermal procedure. **Ceramics International**, v. 40, n. 8, p. 11525-11532, 2014.

[23] PUGAZHENTHIRAN, N.; MURUGESAN, S.; ANANDAN, S. High surface area Ag-TiO_2 nanotubes for solar/visible-light photocatalytic degradation of ceftiofur sodium. **Journal of Hazardous Materials**, v. 263, n.2, p. 541-549, 2013.

[24] JUNG, HG.; KANG, Y. S.; SUN, YK. Anatase TiO_2 spheres with high surface area and mesoporous structure via a hydrothermal process for dye-sensitized solar cells. **Electrochimica Acta**, v. 55, n. 15, p. 4637-4641, 2010.

[25] LEE, SY.; PARK, SJ. TiO_2 photocatalyst for water treatment applications. **Journal of Industrial and Engineering Chemistry**, v. 19, n. 6, p. 1761-1769, 2013.

[26] WANG, H et al. Antibacterial Properties and Corrosion Resistance of Nitrogen-doped TiO_2 Coatings on Stainless Steel. **Journal of Materials Science & Technology**, v. 27, n. 4, p. 309-316, 2011.

[27] TIAN, Y. et al. Antibacterial activity and cytocompatibility of titanium oxide coating modified by iron ion implantation. **Acta biomaterialia**, v. 10, n. 10, p. 4505-4517, 2014.

[28] FAN, J. et al. Dye-sensitized solar cells based on TiO_2 nanoparticles/nanobelts double-layered film with improved photovoltaic performance. **Applied Surface Science**, v. 319, p. 75-82, 2014.

[29] LOGOTHETIDIS, S. (Ed.). **Nanostructured Materials and Their Applications.** Heidelberg: Springer, 2012. 213 p.

[30] VIANA, M. M. et al. Nanocrystalline titanium oxide thin films prepared by sol-gel process. **Brazilian Journal of Physics**, v. 36, n. 3b, p. 1081-1083, 2006.

[31] CHEN, HS.; HUANG, SH.; PERNG, TP. Preparation and Characterization of Molecularly Homogeneous Silica–Titania Film by Sol–Gel Process with Different Synthetic Strategies. **Applied Materials and Interfaces***,* v. 4, n.10, p. 5188-5195, 2012.

[32] SABYROV, K.; BURROWS, N. D.; PENN, R. L. Size-Dependent Anatase to Rutile Phase Transformation and Particle Growth. **Chemical Material**, v. 25*,* n. 8, p.1408-1415, 2013.

[33] BU, X.; ZHANG, G.; ZHANG, C. Effect of nitrogen doping on anatase–rutile phase transformation of TiO_2. **Applied Surface Science**, v. 258, n. 20, p. 7997-8001, 2012.

[34] BERNARDI, M. I. B et al. TiO_2 Thin Film Growth Using the MOCVD method. **Materials Research**, v. 4, n. 3, p.223-226, 2001.

[35] SILVA, V. F. et al. Substrate-controlled allotropic phases and growth orientation of TiO_2 epitaxial thin films. **Journal of Applied Crystallography**, v. 43, p.1502-1512, 2010.

[36] LOTNYK, A.; SENZ, S.; HESSE, D. Growth and characterization of (012) and (001) oriented epitaxial anatase thin films. **Advances in Science and Technology**, v. 46, p. 146-151, 2006.

[37] KENNEDY, R. J.; STAMPE, P. A. The influence of lattice mismatch and film thickness on the growth of TiO_2 on $LaAlO_3$ and $SrTiO_3$ substrates. **Journal of Crystal Growth**, v. 252, n.1, p. 333-342, 2003.

[38] JUNG, H. S. et al. Mobility enhanced photoactivity in sol-gel grown

epitaxial anatase TiO_2 films. **Langmuir**, v. 24, n. 6, p. 2695-2698, 2008.

[39] ANDRONIC, L.; PERNIU, D.; DUTA, A. Synergistic effect between TiO_2 sol–gel and Degussa P25 in dye photodegradation. **Journal of Sol-Gel Science and Technology**, v. 66, n. 3, p. 472-480, 2013.

[40] LI, G. et al. Synergistic effect between anatase and rutile TiO_2 nanoparticles in dye-sensitized solar cells. **Dalton Transactions,** v. 45, p.10078-10085, 2009.

[41] ANDREOZZI, R. et al. Advanced oxidation processes (AOP) for water purification and recovery, **Catalysis Today** v. 53, n. 1, p. 51-59, 1999.

[42] DOMENECH, X. et al. **Advanced oxidation processes for contaminant removal.** In: Contaminants removal by heterogeneous photocatalysis, Blesa M.A., Sánchez B. (Ed), Madrid, Spain: CIEMAT .c 2004, cap 01.

[43] HUANG, C. P.; DONG, C.; TANG, Z. Advanced chemical oxidation: Its present role and potential future in hazardous waste treatment. **Waste Management**, v. 13, p. 361-377, 1993.

[44] BOURGINE, F. P. et al. Ozone and the Formation of Bromate in Water Treatment. **Water and Environment Journal,** v. 7, n. 6, p. 571-576, 1993.

[45] KATSOUNAROS, I. et al. Electrochemical reduction of bromate ions in aqueous solutions on a tin cathode: **In proceeding of European Biological Inorganic Chemistry Conference (EUROBIC)** 10, 2010, Thessaloniki – Greece: 2010, p. 290.

[46] MOTA, A. L. N. et al. Advanced oxidation processes and their application in the petroleum industry: a review. **Brazilian Journal of Petroleum and Gas**. v. 2, n. 3, p. 122-142, 2008.

[47] GULTEKIN, I.; INCE, N. H. Degradation of Reactive Azo Dyes by UV/H_2O_2: Impact of Radical Scavengers. **Journal of Environmental Science and Health, Part A: Toxic/Hazardous Substances and Environmental Engineering**. v. 39, n. 4, p. 1069-1081, 2004.

[48] HOFFMANN, M. R.; MARTIN, F. T.; CHOI, W.; BAHNEMANN, D. W. Environmental Applications of semiconductor photocatalysis**. Chemical Reviews,** v. 95, p. 69-96, 1995.

[49] XU, TH et al. Band structure of TiO_2 doped with N, C and B. **Journal Zhejiang University Science B**, v. 7, n. 4, p. 299-303, 2006.

[50] GRATZEL, M. **Heterogeneous Photochemical Electron Transfer**. Boca Ranto: CRC Press,1989, 98 p.

[51] LINSEBIGLER, A. L.; LU, G.; YATES, J. T. J. Photocatalysis on TiO_2 Surfaces: Principles, Mechanisms, and Selected Results. **Chemical Reviews**, v. 95, p. 735-758, 1995.

[52] ZALESKA, A. Doped-TiO_2: A Review**. Recent Patents on Engineering,** v. 2, p.157-164, 2008.

[53] BARKA, N. et al. Kinetic Modeling of the Photocatalytic Degradation of Methyl Orange by supported TiO_2. **Journal of Environmental Science and Engineering.** v. 4, n. 5, p. 1-5, 2010.

[54] NOSAKA, Y.; NAKAMURA, M.; HIRAKAWA, T. Behavior of superoxide radicals formed on TiO_2 powder photocatalyst by chemiluminescent probe method. **Physical Chemistry Chemical Physics**, v. 4, n.6, p. 1088-1092, 2002.

[55] CHONG, M. N. et al. Recent developments in photocatalytic water treatment technology: a review. **Water research**, v 44, n. 10, p. 2997-3027, 2010.

[56] LUTTRELL, T. et al. Why is anatase a better photocatalyst than rutile? - Model studies on epitaxial TiO_2 films. **Scientific Reports,** v. 4, p. 1-7, 2014.

[57] LEE, SY.; PARK, SJ. TiO_2 photocatalyst for water treatment applications. **Journal of Industrial and Engineering Chemistry**, v. 19, n. 6, p. 1761-1769, 2013.

[58] CHIN, S. S.; CHIANG, K.; FANE, A. G. The stability of polymeric membranes in TiO_2 photocatalysis process. **Journal of Membrane**

Science, v. 275, p. 202-211, 2006.

[59] BYRNE. J. A. et al. Immobilisation of TiO_2 for the treatment of polluted water. **Applied Catalysis B: Environmental**, v. 17, p. 25-36, 1998.

[60] POZZO, R. L.; BALTANAS, M. A.; CASSANO, A. E. Supported titanium oxide as photocatalyst in water decontamination: state of the art. **Catalysis Today**, v. 39, p. 219-231, 1997.

[61] TORRES, A. R. et al. A comparison between bulk and supported TiO_2 photocatalysts in the degradation of formic acid, **Brazilian Journal Chemical Engineering**, v. 24, n. 2, p.185-192, 2007.

[62] MASUDA, Y.; KATO K. Anatase TiO_2 films crystallized on SnO_2:F substrates in an aqueous solution, **Thin Solid Films**, v. 516, p. 2547-2552, 2008.

[63] SAMPATH, S.; UCHIDA, H.; YONEYAMA, H. Photocatalytic degradation of gaseous pyridine over zeolite-supported titanium dioxide. **Journal of Catalysis**, v.149, p.189-194, 1994.

[64] TAKEDA, N et al. Effect of inert supports for titanium dioxide loading on enhancement of photodecomposition rate of gaseous propionaldehyde. **Journal of Physical Chemistry**, v. 99, n. 26, p. 9986-9991,1995.

[65] VOHRA, M. S.; TANAKA, K. Enhanced photocatalytic activity of Nafion-coated TiO_2, **Environmental Science Technology**, v. 35, p. 411-415, 2001.

[66] DAWSON, M.; SOARES, G. B.; RIBEIRO, C. Preparation and photocatalytical performance of TiO_2:SiO_2 nanocomposites produced by the polymeric precursors**. Journal of Nanoscience and Nanotechnology**, v. 13, n. 7, p. 5126-5133, 2013.

[67] JUNG, K. Y.; PARK, S. B. Effect of calcination temperature and addition of silica, zirconia, alumina on the photocatalytic activity of titania. **Korean Journal of Chemical Engineering**, v.18, p. 879-888, 2001.

[68] WANG, H. N. et al. Synthesis and characterization of TiO_2-incorporated silica foams*.* **Journal of Materials Science**, v. 44, p. 6484-6489, 2009.

[69] YODA, S.; SUH, D. J.; SATO, T. Adsorption and photocatalytic decomposition of benzene using silica–titania and titania aerogels: effect of supercritical drying, **Journal of Sol-Gel Science and Technology**, v. 22, p. 75-81, 2001.

[70] ANDERSON, C.; BARD, A. J. An Improved Photocatalyst of TiO_2/SiO_2 Prepared by a Sol-Gel Synthesis. **Journal Physics and Chemistry**, v. 99, n. 24, p. 9882-9885, 1995.

[71] KIM, Y.; YOON, M. TiO_2/Y-Zeolite encapsulating intramolecular charge transfer molecules: a new photocatalyst for photoreduction of methyl orange in aqueous medium. **Journal of Molecular Catalysis A: Chemistry**. v. 168, p. 257-263, 2001.

[72] SASIKALA, R. et al. Role of support on the photocatalytic activity of titanium oxide. **Applied Catalysis A: General**, v. 390, n. 1-2, p. 245-252, 2010.

[73] ANASTASESCU, M. et al. Substrate impact on optical and microstructural properties of TiO_2–PEG sol–gel films. **Ceramics International**, v. 40, p. 11803-11811, 2014.

[74] KAO, CH. Growth of Epitaxial Anatase TiO_2 (001) Thin Film on NaCl (001) Substrate by Ion Beam Sputtering and Thermal Annealing. **Japan Journal of Applied Physics**, v. 51, p. 45502-45506, 2012.

[75] LOTNYK, A.; SENZ, S.; HESSE, D. Epitaxial growth of TiO_2 thin films on $SrTiO_3$, $LaAlO_3$ and yttria-stabilized zirconia substrates by electron beam evaporation. **Thin Solid Films**, v. 515, p. 3439-3447, 2007.

[76] YANG, C. et al. C-axis-oriented growth of anatase TiO_2 thin films on glass substrate with $SrTiO_3$/TiN template. **Journal of Crystal Growth**, v. 376, p. 66-69, 2013.

[77] XIE, Y. et al. Hierarchical TiO_2 photocatalysts with one-dimensional heterojunction for improved photocatalytic activities. **Nano research**, v. 8, p. 2092-2101, 2015.

[78] LIU, Z. et al. Anatase TiO_2 Nanoparticles on Rutile TiO_2 Nanorods: A Heterogeneous Nanostructure via Layer-by-Layer Assembly.

Langmuir, v. 23, p. 10916-10919, 2007.

[79] KAWAHARA, T. et al. A patterned TiO_2 (anatase)/TiO_2 (rutile) bilayer-type photocatalyst: effect of the anatase/rutile junction on the photocatalytic activity. **Angewandte Chemie (International Edition)**, v. 41, n. 15, p. 2811-2813, 2002.

[80] MENDONÇA, V. R. et al. TiO_2-SnO_2 heterostructures applied to dye photodegradatIon: The relationship between variables of synthesis and photocatalytic performance. **Applied Surface Science**, v. 298, p. 182-191, 2014.

[81] REED, J. S. **Principles of Ceramics Processing.** 2 ed, United States: John Wiley& Sons, 1995. 688 p.

[82] RAHAMAN, M. N. **Ceramic Processing and Sintering**. 2 ed, United States: CRC Press, 2003. 875 p.

[83] KANG, S. L. **Sintering: Densification, Grain growth and Microstructure.** 1 ed, Oxford: Elsevier Butterworth-Heinemann, 2005. 280 p.

[84] REAL, C. et al. Influence of grinding on the sintering properties of Rutile. **Solid State Ionics**, v. 141, p. 671-675, 2001.

[85] LI, D. et al. The Master Sintering Curve for Pressureless Sintering of TiO_2. **Science of Sintering**, v. 39, p.103-110, 2007.

[86] YOO, S.; AKBAR, S. A.; SANDHAGE, K. H. Nanocraving of bulk titania crystals into oriented arrays of single-crystal nanofibers via reaction with hydrogen–bearing gas. **Advanced Materials**, v. 16, n. 3, p. 260-264, 2004.

[87] RUBIO, J. et al. Characterization and sintering behavior of submicrometre titanium dioxide spherical particles obtained by gas-phase hydrolysis of titanium tetrabutoxide, **Journal of Materials Science**, v. 32, n. 3, p. 643-652, 1997.

[88] SAKTIVEL, S.; KISCH, H. Daylight photocatalysis by carbon-modified titanium dioxide, **Angewandte Chemie International Edition**, v. 42, p.

4808-4911, 2003.

[89] DAWSON, M.; SOARES, G. B.; RIBEIRO, C. Influence of calcination parameters on the synthesis of N-doped TiO_2 by the polymeric precursors method. **Journal of Solid State Chemistry** v. 215, p. 211-218, 2014.

[90] UMEBAYASHI, T. et al. Bandgap narrowing of titanium dioxide by sulfur doping. **Applied Physics Letters**, v. 81, n. 3, p. 454-456, 2002.

[91] WANG, HW. et al. Synthesis and photocatalysis of mesoporous anatase TiO_2 powders incorporated Ag nanoparticles. **Journal Physics and Chemistry of Solids**, v. 69, p. 633-636, 2008.

[92] CONNELLY, K.; WAHAB, A. K.; IDRISS, H. Photoreaction of Au/TiO_2 for hydrogen production from renewables: a review on the synergistic effect between anatase and rutile phases of TiO_2. **Materials for Renewable and Sustainable Energy**, v. 1, n. 1, p. 1-12, 2012.

[93] HURUM, D. C. et al. Explaining the enhanced photocatalytic activity of Degussa P25 mixed-phase TiO_2 using EPR. **Journal of Physical Chemistry B**, v.107, n.19, p. 4545-4549, 2003.

[94] LI, G.; GRAY, K. A. The solid-solid interface: Explaining the high and unique photocatalytic reactivity of TiO_2-based nanocomposite materials. **Chemical Physics**, v. 339, p.173–187, 2007.

[95] LAURETO, E. et al. The technique of photoluminescence applied to investigation of structural imperfections in quantum wells of semiconductor materials. **Semina: Ciências Exatas e Tecnológicas**, v. 26, n. 1, p. 23-35, 2005.

[96] KAWAHARA, T. et al. Photocatalytic activity of rutile–anatase coupled TiO_2 particles prepared by a dissolution–reprecipitation method. **Journal of Colloid and Interface Science**. v. 267, n. 2, p. 377-381, 2003.

[97] OHNO, T. et al. Synergism between rutile and anatase TiO_2 particles in photocatalytic oxidation of naphthalene. **Applied Catalysis A: General,** v. 244, n. 2, p. 383-391, 2003.

[98] KOSUKA, H. (Ed.) **Sol-gel processing**. Volume I in SAKKA, S. (Ed.). **Handbook of sol-gel science and technology. Processing, Characterization and Applications.** United States: Klewer Academic Publishers, 2005.

[99] HANAOR, D. A. H.; SORRELL, C. C. Review of the anatase to rutile phase transformation. **Journal of Materials Science**, v. 46, n. 4, p. 855-874, 2011.

[100] KNORR, F. J.; ZHANG, D.; MCHALE, J. L. Influence of $TiCl_4$ Treatment on Surface Defect Photoluminescence in Pure and Mixed-Phase Nanocrystalline TiO_2 , **Langmuir**, v. 23, n. 17, p. 8686-8690, 2007.

[101] PARK, NG.; VAN DE LAGEMAAT, J.; FRANK, A. J. Comparison of dye sensitized rutile and anatase TiO_2 based solar cells. **Journal of Physical Chemistry**, v. 104, p. 8989-8994, 2000.

[102] DATYE, A. K. et al. Microstructural characterization of a Fumed Titanium Dioxide Photocatalyst. **Journal Solid State Chemistry**, v. 115, p. 236-239, 1995.

[103] OHNO, T. et al. Morphology of a TiO_2 photocatalyst (Degussa, P-25) consisting of anatase and rutile crystalline phases. **Journal of Catalysis**, v. 203, p. 82-86, 2001.

[104] CARTER, C. B.; NORTON, M. G. **Ceramic Materials: Science and Engineering**. 2 ed, New York: Springer, 2013. 745 p.

[105] EVARESTOV, R. A. Quantum Chemistry of Solids: **The LCAO First Principles Treatment of Crystals**, Berlin: Springer, 2007. 147 p.

[106] MEAGHER, E. P., LAGER, G. A. Polyhedral thermal expansion in the TiO_2 polymorphs: refinement of the crystal structures of rutile and brookite at high temperature. **Canadian Mineralogist**, v. 17, p. 77-85, 1979.

[107] KNAUTH, P. Point Defects in 3D and 1D Nanomaterials: The Model Case of Titanium Dioxide, 11th Europhysical Conference on Defects in Insulating Materials (EURODIM 2010). IOP Conf. Series: **Materials Science and Engineering** 15 (2010).

[108] WETCHAKUN, N. et al. Influence of calcination temperature on anatase to rutile phase transformation inTiO_2 nanoparticles synthesized by the modified sol–gel method. **Materials Letters**, v. 82, p. 195-198, 2012.

[109] GHOSH, T. B.; DHABAL, S.; DATTA, A. K. On crystallite size dependence of phase stability of nanocrystalline TiO_2. **Journal of Applied Physics**, v. 94, p. 4577-4582, 2003.

[110] LI, G. et al. High Purity Anatase TiO_2 Nanocrystals: Near Room-Temperature Synthesis, Grain Growth Kinetics, and Surface Hydration Chemistry. **Journal of American Chemical Society**, v. 127, p. 8659-8666, 2005.

[111] WEI, Y. et al. Study on preparation and formation mechanism of nanophase TiO_2 with different morphologies and crystalline-structures from $TiOCl_2$ solution. **Acta Chimica Sinica**, v. 59, n. 9, p. 1424-1429, 2001.

[112] LEVCHENKO, A. A. et al. TiO_2 Stability Landscape: Polymorphism, Surface Energy, and Bound Water Energetics, **Chemistry of Materials**. v. 18, n. 26, p. 6324-6332, 2006.

[113] ZHANG, H.; BANFIELD, J. F. Understanding polymorphic phase transformation behavior during growth of nanocrystalline aggregates: insights from TiO_2. **Journal of Physical Chemistry B**., v. 104, p. 3481-3487, 2000.

[114] HWU, Y. et al. X-ray absorption of nanocrystal TiO_2. **Nanostructure Materials**, v. 9, p. 355-358, 1997.

[115] ZHOU, Y.; FICHTHORN, K. A. Microscopic View of Nucleation in the Anatase-to-Rutile Transformation, **Journal of Physical Chemical C**, v. 116 ,n. 14, p. 8314-8321, 2012.

[116] SHANNON, D. R.; PASK, J. A. Topotaxy in Rutile Anatase Transformation. **The American Mineralogist**, v. 49, p. 1707-1711, 1964.

[117] SHAO, Y. et al. Lattice deformation and phase transformation from nano-scale anatase to nano-scale rutile TiO_2 prepared by a sol-gel

technique. **China Particuology**, v. 2, n. 3, p.119-123, 2004.

[118] MACKENZIE, K. J. D. Calcination of titania V. Kinetics and mechanism of the anatase-rutile transformation in the presence of additives. **Transactions and Journal of the British Ceramic Society**. v. 74, n. 3, p. 77-78,1975.

[119] MACKENZIE, K. J. D. Calcination of titania V. Effect of additives on the anatase-rutile transformation. **Transactions and Journal of the British Ceramic Society**, v. 74, n. 2, p. 29-34, 1975.

[120] VARGAS, S. et al. Effect of cationic dopants on the phase transition temperature of titania prepared by the Sol-gel method. **Journal of Materials Research** v. 14, n. 10, p. 3932-3937,1999.

[121] LOTGERING, F. K. Topotactical reactions with ferrimagnetic oxides having hexagonal crystal structures. **Journal Inorganic and Nuclear Chemistry**, v. 9, p.113-123, 1959.

[122] Epitaxy <http://global.britannica.com/EBchecked/topic/190362/epitaxy> Accessed 25/11/2014.

[123] WANG, S. J.; HUAN, A. C. H. **Epitaxial oxides on semiconductors for application in nanoelectronics** In: Leading-Edge semiconductor research, Elliot B.T. (Ed), New York: Nova Science Publishers, 2005. p.151-200.

[124] POHL, U. W. **Epitaxy of Semiconductors: Introduction to Physical Principles**. Verlag: Springer, 2013. 325 p.

[125] SUGIHARTO, S. Y. et al. Preparation of TiO_2-anatase film on Si (001) substrate with TiN and $SrTiO_3$ as buffer layers. **Journal of Physics: Condensed matter**, v. 13, p. 2875-2881, 2001.

[126] OGALE, S. B. **Thin Films and Heterostructures for Oxide Electronics**, New York: Springer science, 2005. 430 p.

[127] Epitaxy rutile and hematite <http://www.mineral-forum.com/> *apud* <http://en.wikipedia.org/wiki/Epitaxy> Accessed: 24.10.2014.

[128] CHAN, K. Y. S.; GOH, G. K. L. Solution Epitaxy of TiO_2 Thin Films. **Journal of The Electrochemical Society**, v. 156, n. 7, p. 231-235, 2009.

[129] CHO, A. Y.; ARTHUR, J. R. Molecular beam epitaxy. **Progress in Solid State Chemistry**, v. 10, p. 157-191, 1975.

[130] BEIJA, M.; AFONSO, C. A. M.; MARTINHO, J M. G. Synthesis and applications of Rhodamine derivatives as fluorescent probes. **Chemical Society Revelation**, v. 38, p. 2410-2433, 2009.

[131] ROCHKIND, M.; PASTERNAK, S.; PAZ, Y. Using Dyes for Evaluating Photocatalytic Properties: A Critical Review, **Molecules**, v. 20, p. 88-110, 2014.

[132] CHAN, K. H.; CHU, W. Atrazine removal by catalytic oxidation processes with or without UV irradiation Part II: an analysis of the reaction mechanisms using LC/ESI-tandem mass spectrometry. **Applied Catalysis B: Environment**, v. 58, p. 165-174, 2005.

[133] LI, X.; ZENG, F.; LI, K. Computer Assisted Pathway Generation for Atrazine Degradation in Advanced Oxidation Processes. **Journal of Environmental Protection**, v. 4, n. 1b, p. 62-69, 2013.

[134] JONES, F. W. The measurement of particle size by the X-ray method. **Proceedings Royal Society of London Society A. Mathematical and Physical Sciences**, v. 166, p. 16-43, 1938.

[135] BRUNAUER, S.; EMMETT, P. H.; TELLER, E. Adsorption of Gases in Multimolecular Layers. **Journal of American Chemical Society**, v. 60, p. 309-319, 1938.

[136] KATO, H.; SUZUKI, M.; FUJITA, K. Reliable size determination of nanoparticles using dynamic light scattering method for in vitro toxicology assessment. **Toxicology in vitro**, v. 23, n. 5, p. 927-934, 2009.

[137] LEE, H. et al. A novel approach to preparing nano-size CO_3O_4-coated Ni powder by the Pechini method for MCFC cathodes. **Journal of**

Materials Chemistry, v. 13, p. 2626-2632, 2003.

[138] Image spin coating <http://www.sneresearch.com/eng/info/show.php?c_id=4970&pg=5&s_sort=&sub_cat=&s_type=&s_word= > Accessed: 19.12.2014.

[139] Spin coating process <http://www.utdallas.edu/~rar011300/CEEspinner/SpinTheory.pdf> Accessed: 19.12.2014.

[140] NGUYENA, T.; HIND, A. R. **The measurement of absorption edge and band gap properties of novel nanocomposite materials**. Varian Cary 500 Spectrophotometer manual No. 081.

[141] MOORE, J. W. **Kinetics and Mechanism**, 3 ed, New York: John Wiley & Sons, 1961. 455 p.

[142] ZHAO, J.; GU, Y.; HUANG, J. Flame synthesis of hierarchical nanotubular rutile titania derived from natural cellulose substance. **Chemical Communications**, v. 47, n. 38, p. 10551-10553, 2011.

[143] WARHEIT, D. B. et al. Pulmonary toxicity study in rats with three forms of ultrafine-TiO_2 particles: differential responses related to surface properties. **Toxicology**, v. 230, n. 1, p. 90-104, 2007.

[144] TOPUZ, E.; SIGG, L.; TALINLI, I. A systematic evaluation of agglomeration of Ag and TiO_2 nanoparticles under freshwater relevant conditions. **Environmental Pollution,** v. 193, p. 37-44, 2014.

[145] JIANG, J.; OBERDORSTER, G.; BISWAS, P. Characterization of size, surface charge, and agglomeration state of nanoparticle dispersions for toxicological studies. **Journal of Nanoparticle Research,** v. 11, p. 77-89, 2009.

[146] SOBHANI, M.; EBADZADEH, T.; RAHIMIPOUR, M. R. Formation and densification behavior of reaction sintered alumina-20 wt.% aluminium titanate nano-composites. **International Journal of Refractory Metals & Hard Materials**, v. 47, p. 49-53, 2014.

[147] RAK, Z. S. From nanosize powder to a diesel soot converter. In: nato advanced study institute on functional gradient materials and surface layers prepared by fine particles technology. 16., 2000, Kiev, Ukraine. **Proceedings** Functional gradient materials and surface layers prepared by fine particles technology, Klawer Academic Publishers, Dordrecht: The Netherlands, 2001. p. 87-103.

[148] WEI, X. et al. Synthesis, Characterization, and Photocatalysis of Well-Dispersible Phase-Pure Anatase TiO_2 nanoparticles. **International Journal of Photoenergy**, v. 2013, p.1-6, 2013.

[149] SOARES, G. B. et al. Facile synthesis of N-doped TiO_2 nanoparticles by a modified polymeric precursor method and its photocatalytic properties. **Applied Catalysis B- Environmental**, v. 106, n. 3-4, p. 287-294, 2011.

[150] GERMAN, R. M.; PARK, J. S. **Handbook Mathematical Relations in Particulate Materials Processing Ceramics, Powder Metals, Cermets, Carbides, Hard Materials, and Minerals**. New York: John Wiley & Sons Inc., 2008. 419 p.

[151] COSTA, G. C. et al. Effect of viscosity and temperature on the microstructure of BBT thin films. **Materials Research,** v. 6, n. 3, p. 347-351, 2003.

[152] FEWSTER, P. F. X-ray analysis of thin films and multilayers. **Reports on Progress in Physics,** v. 59, n. 11, p. 1339-1407, 1996.

[153] YAN, J. et al. Understanding the effect of surface/bulk defects on the photocatalytic activity of TiO_2: anatase versus rutile. **Physical Chemistry Chemical Physics**, v. 15, p. 10978–10988, 2013.

[154] CZERWINSKI, F.; SZPUNAR, J. A. Atomic force microscopy imaging of the growth features on the surface of rutile. **Micron**, v. 29, p. 201-206, 1998.

[155] KUBELKA, P.; MUNK F. Ein Beitrag zur Optik der Farbanstriche. **Zeitschrift für Technische Physik,** v. 12, p. 593-620, 1931 *apud* BUNKHOLT, I.; KLEIV, R. A. The applicability of the Kubelka–Munk

model in GCC brightness prediction. **Minerals Engineering**, v. 56, p. 129-135, 2014.

[156] CARNIE, M.; WATSON, T.; WORSLEY, D. UV Filtering of Dye-Sensitized Solar Cells: The Effects of Varying the UV Cut-Off upon Cell Performance and Incident Photon-to-Electron Conversion Efficiency.**International Journal of Photoenergy**, v. 2012, p. 1-9, 2012.

[157] ACOSTA, M.; RIECH, I.; MARTÍN-TOVAR, E. Effects of the Argon Pressure on the Optical Band Gap of Zinc Oxide Thin Films Grown by Nonreactive RF Sputtering. **Advances in Condensed Matter Physics**, v. 2013, p. 1-6, 2013.

[158] ROBINSON, J. W.; FRAME, E. M. S.; G. M. II FRAME. **Undergraduate Instrumental Analysis.** Marcel Dekker: New York, 2005. 1079 p.

[159] FAN, Y. Highly Selective Deethylation of Rhodamine B on Prepared in Supercritical Fluids, **International Journal of Photoenergy**, v. 2012, p.1-7, 2012.

[160] SHAO, X. et al. Enhanced photocatalytic activity of TiO_2-C hybrid aerogels for methylene blue degradation. **Science Report**, v. 3, n. 3018, p. 1-9, 2013.

[161] PHILIP, L.; VIJAYANANDAN, A.; SENTHILNATHAN J. Modified TiO_2-based photocatalytic systems for the removal of emerging contaminants from water. In: Reisner, D. E.; Pradeep, T. (Ed). **Aquananotechnology Global Aspects**, Boca Raton: CRC Press, 2014. p. 479-510.

[162] CAMPANELLA, L.; VITALIANO, R. Atrazine toxicity reduction following H_2O_2/TiO_2 photocatalyzed reaction and comparison with H_2O_2-photolytic reaction. **Annali di Chimica**, v. 92, p. 123-134, 2007.